Particles and Bubbles Collisions Frequency in Homogeneous Isotropic Turbulence and Applications to Minerals Flotation Machines

Hassan Elhady H. Fayed

Dissertation submitted to the faculty
of the Virginia Polytechnic Institute and State University
in partial fulfillment of the requirements for the degree of

Doctor of Philosophy
in
Engineering Mechanics

Saad Ragab - Chairman
Gerald Luttrell
Slimane Adjerid
Muhammad Hajj
Surot Thangjitham

December 6th, 2013
Blacksburg, Virginia

Keywords: Collisions Frequency, Multiphase flow, Homogeneous turbulence, Direct numerical simulation, Large-eddy simulation, Multifractal modeling, Bubble size distribution, Minerals flotation machines

Particles and Bubbles Collisions Frequency in Homogeneous Isotropic Turbulence and Applications to Minerals Flotation Machines

Hassan Elhady H. Fayed

(ABSTRACT)

The collisions frequency of dispersed phases (particles, droplets, bubbles) in a turbulent carrier phase is a fundamental quantity that is needed for modeling multiphase flows with applications to chemical processes, minerals flotation, food science, and many other industries. In this dissertation, numerical simulations are performed to determine collisions frequency of bi-dispersed particles (solid particles and bubbles) in homogeneous isotropic turbulence. Both direct numerical simulations (DNS) and large-eddy simulations (LES) are conducted to determine velocity fluctuations of the carrier phase. The DNS results are used to validate existing theoretical models as well as the LES results. The dissertation also presents a CFD-based flotation model for predicting the pulp recovery rate in froth flotation machines.

In the direct numerical simulations work, particles and bubbles suspended in homogeneous isotropic turbulence are tracked and their collisions frequency is determined as a function of particle Stokes number. The effects of the dispersed phases on the carrier phase are neglected. Particles and bubbles of sizes on the order of Kolmogorov length scale are treated as point masses. Equations of motion of dispersed phases are integrated simultaneously with the equations of the carrier phase using the same time stepping scheme. In addition to Stokes drag, the pressure gradient in the carrier phase and added-mass forces are also included. The collision model used here allows overlap of particles and bubbles. Collisions kernel, radial relative velocity, and radial distribution function found by DNS are compared to theoretical models over a range of particle Stokes number. In general, good agreement between DNS and recent theoretical models is obtained for radial relative velocity for both particle-particle and particle-bubble collisions. The DNS results show that around Stokes number of unity particles of the same group undergo expected preferential concentration while particles and bubbles are segregated. The segregation behavior of particles and bubbles leads to a radial distribution function that is less than one. Existing theoretical models do not account for effects of this segregation behavior of particles and bubbles on the radial distribution function.

In the large-eddy simulations efforts, the dissertation addresses the importance of the subgrid fluctuations on the collisions frequency and investigates techniques for predicting those fluctuations. The cases studied are of particles-particles and particles-bubbles collisions at Reynolds number $Re_\lambda = 96$. A study is conducted first by neglecting the effects of subgrid velocity fluctuations on particles and bubbles motions. It is found that around Stokes number of unity solid particles of the same group undergo the well known preferential concentration as observed in the DNS. Effects of pressure gradient on the particles are negligible due to

their small sizes. Bubbles as a low inertia particles are very sensitive to subgrid velocity and acceleration fields where the effects of pressure gradient in the carrier phase are dominant. However, particle-bubble radial distribution functions from LES are not as low as that from DNS. To account for the effects of subgrid field on the dispersion of particles and bubbles, a new multifractal methodology has been developed to construct a subgrid vorticity filed from the resolved vorticity field in frame work of LES. A Poisson′s solver is used to obtain the subgrid velocity field from the subgrid vorticity field. Accounting for the subgrid velocity fluctuations (but neglecting pressure gradient) produced minor changes in the radial distribution function for particle-particle and particle-bubble collisions. We conclude from this study that for accurate particle tracking in LES the subgrid velocity fluctuations must be dynamically realizable field (temporally and spatially correlated with the large scale motion). Adding random SGS velocity fluctuations is not enough to capture the correct radial distribution functions of dispersed phases especially for bubbles-particles collisions where the pressure gradient term (or acceleration $D\vec{u}_f'/Dt$) is responsible for particle-bubble segregation around particle Stokes number near one.

A CFD-based model for minerals flotation machines has been developed in this dissertation. The objective of flotation models is to predict the recovery rate of minerals from a flotation cell. The developed model advances the state-of-the-art of pulp recovery rate prediction by incorporating validated theoretical collisions frequency models and detailed hydrodynamics from two-phase flow simulations. Spatial distributions of dissipation rate and air volume fraction are determined by the two-phase hydrodynamic simulations. Knowing these parameters throughout the machine is essential in understanding the effectiveness of different components of flotation machine (rotor, stator or disperser, jets) on the flotation efficiency. The developed model not only predicts the average pulp recovery rate but also it indicates regions of high/low recovery rates. The CFD-based flotation model presented here can be used to determine the dependence of recovery rate constant at any locality within the pulp based on particle diameter, particle specific gravity, contact angle, and surface tension.

Dedication

To my mother *Saadia Alshaer*, my father *Hassan Fayed*, my wife *Heba Elsewidy*, my father in law *Ahmed Elsewidy*, and my three sons *Ahmed*, *Adam*, and *Ali*

Acknowledgment

I would like to express my deepest appreciation to my advisor, Professor Saad A. Ragab who has the attitude of a genius; he continually and convincingly conveyed a spirit of adventure in regard to both basic research level and industrial applications. Without his guidance and persistent help this dissertation would not have been possible.

I would like to thank my committee member, Professor Muhammad Hajj, for his kind support. I would like also to thank Professors Slimane Adjerid, Professor Surot Thangjitham and Professor Gerald Luttrell for their efforts to make this thesis more meaningful.

My gratitude is due to my mother, my father and all people around me that helped and supported me to work for this PhD.

A special thanks are to be to my wife Heba and my sons, Ahmed, Adam and Ali, that they make my life full of happiness and fun.

We would like to acknowledge the financial support of FLSmidth Minerals, Inc., Salt Lake City, UT, that made this dissertation possible.

Contents

List of Figures

List of Tables

Nomenclature

$\bar{p}$	Filtered pressure field
$\bar{u_i}$	Filtered velocity field
β	Collision kernel, m^3/s
Δx	LES grid spacing
ϵ	turbulent kinetic energy dissipation rate
η	Kolmogorov length scale
λ	Taylor microscale
ν_f	Carrier phase kinematic viscosity
ν_t	Spectral eddy viscosity
Ω_i	Particle inertia
ρ_f	Carrier phase density
ρ_f	Carrier phase density
ρ_i	Particle density $i = p$ for particles and $i = b$ for bubbles
σ'	Ornstein-Uhlenbeck process standard deviation
τ'	Ornstein-Uhlenbeck process relaxation time scale
τ_i^*	Particle modified response time $i = p$ for particles and $i = b$ for bubbles
τ_k	Kolomogrov's time scale
τ_i	Particle response time $i = p$ for particles and $i = b$ for bubbles
τ_{ji}	Subgrid stress tensor

$\hat{\vec{R}}_{\vec{k}}$ complex-valued vector

$\vec{F}$ Stochastic forcing term

$\vec{K}$ Wavenumber vector

$\vec{R}$ Vector potential

$\vec{u}$ Instantaneous velocity field

$\vec{u}_f$ Carrier phase velocity at the center of each particle and bubble

$\vec{V}_i$ Instantaneous particle velocity

$\vec{X}_i$ Instantaneous particle position

A_c Annular free surface area, [m^2]

b Average loading parameter

C_A Added mass coefficient = 0.5

C_A Added mass coefficient

C_K Kolmogorov constant = 2.5

d collision radius

$D\vec{u}_f/Dt$ Carrier phase acceleration at the center of each particle and bubble

d_b Bubble diameter, [m]

D_d Draft tube inside diameter, [m]

D_p Standpipe inside diameter, [m]

d_p Particle diameter, [m]

D_r Rotor maximum diameter, [m]

dx DNS grid spacing

$E(k)$ turbulent kinetic energy spectrum

$g_{pb}(d)$ Particle-bubble radial distribution function (RDF) at contact

$g_{pp}(d)$ Particle-particle radial distribution function (RDF) at contact

H_p Standpipe height, [m]

H_r Rotor blade height, [m]

i Complex number $\sqrt{-1}$ or index

$I(N_f)$ Intermittency factor

k Wavenumber radius in spectral domain $= \sqrt{\vec{K} \cdot \vec{K}}$

k_1^* Local pulp rate constant, $1/s$

k_c Cutt-off wavenumber

k_1 Particle-bubble attachment rate constantm^3/s

k_2 Particle-bubble detachment rate constant$1/s$

L_f Lagrangian integral length scale

M_n Multipliers

N Rotor speed, [rpm]

N DNS grid size

n_a Particle-bubble aggregates number concentration $1/m^3$

N_b Number of bubbles

n_b Bubble number concentration $1/m^3$

N_f Number of multiplicative cascades $= dx/\Delta x$

n_{p1} Particle number concentration of free particles $1/m^3$

n_{p2} Particle number concentration of attached particles to bubbles $1/m^3$

n_{pT} Particle-bubble aggregates number concentration $1/m^3$

N_p Number of particles

N_t Number of time steps

P Power, [kW]

$p(\vec{x}, t)$ Pressure field of the carrier phase

P_a Probability of particle-bubble attachment

P_c Probability of particle-bubble collision

P_d	Probability of particle-bubble detachment $= 1 - P_c$
P_s	Probability of particle-bubble stabilization
Q_a	Air volume flow rate, [m^3/min]
Q_Δ	Enstrophy field between first and second test filter
Q_{sgs}	Subgrid enstrophy
R	Average pulp pseudo rate constant, $1/s$
Re_λ	Reynold number based on Taylor micro scale $= \rho_f u'/\nu_f$
S	Number of particles attached per bubble
St_i^*	Modified Stokes number
St_i	Particle Stokes number $i = p$ for particles and $i = b$ for bubbles
T_e	integral time scale or eddy life time
T_L	Lagrangian integral length scale
u_i'	Subgrid velocity field
u_i^Δ	Velocity field between the first and the second test filter
U_b	Bubble turbulent fluctuations, m/s
U_p	Particle turbulent fluctuations, m/s
U_t	Rotor tip speed, [m/s]
u_f'	Turbulent fluctuations, m/s
$u_{r.m.s}'$	root mean square of turbulent velocity
Z_2	Detachment frequency, $1/s$
r.m.s	root mean square

Chapter 1

Introduction

1.1 Motivation

Multiphase flows involve the motion of a fluid and other particulate phases (solid particles in gases or liquids or gaseous bubbles in liquids). The fluid is called 'carrier phase' and other phases in relative motion with the fluid are called dispersed phases. Applications of multiphase flows exist in many industries such as water treatment, mining and minerals separation, power generation, food processing, etc. In liquid-solid multiphase flows, solid particles are carried by the liquid and referred to as slurry flows. Slurry flows cover a wide range of applications of coal and minerals processing, water treatment, metal cutting water jets, and pulp & paper industries. Gas-solid/liquid particles flows are another example of multiphase flows. This type of multiphase flows has also a wide range of applications such coal fluidized beds, cement transportation, sprays and aerosols, milk drying, etc. Other phenomena that take place in nature such as sand dunes, sedimentation in rivers and rain formation are an evident examples of natural multiphase flows.

Three phase flows can be encountered in many industrial applications such as minerals flotation machines. In flotation machines, slurry, which include the valuable minerals particles mixed with gangue particles, are pumped into a tank. In mechanically agitated machines, a rotor is used to circulate the slurry and generate turbulence for air bubbles generation and dispersion in the tank pulp volume. The surfaces of the valuable minerals particles are treated by adding some surfactants to make them hydrophobic in direct flotation or hydrophilic in reverse flotation. In direct flotation, hydrophobic particles attach to air bubbles upon collisions and the particles-bubbles aggregates float upward by buoyancy to the froth phase. The froth flows over a weir on the top walls of the tank and minerals particles are collected in an additional annular tank 'launder' attached to the tank walls. In reverse flotation, Minerals particles precipitates to the tank bottom while gangue particles float up to the froth phase.

Design and modeling of such a complex flow has been established empirically in the past. Sophisticated experimental techniques such as particle image velocimetry 'PIV' and laser Doppler velocimetry 'LDV' have been developed to gain better understanding and improve different processes in multiphase flows. However, many of the experimental techniques have many limitations and high level of uncertainty in their measurements. Numerical simulation is another feasible approach that can overcome some of the shortcomings of the experimental techniques . The increased computational capabilities in the last two decades enabled the development of numerical models to be part of the design tools for such complex systems.

Three different approaches are used to simulate multiphase flows. First approach is the one fluid model, where at any point in space only one phase exists. In this model, dispersed phases are simulated by tracking their interfaces with the carrier phase. The second model is a two or multi-fluid model where at any point in space two or more phases co-exist. Each of the phases has its own transport equations averaged by the void fraction of each phase. The momentum equations of the different phases are coupled by the interfacial forces between different phases. This model is called Eulerian-Eulerian model and is recommended for high values of the dispersed phases void fraction. The third model is the Eulerian-Lagrangian model, where the dispersed phases are simulated by tracking a set of point mass particles, bubbles or droplets moving within the carrier phase. The tracking of these dispersed phases is done by solving equations of motion of each particle. This model is appropriate for very small values of void fraction.

In this dissertation, Eulerian-Lagrangian model is used to track a system of solid particles and bubbles in a homogeneous isotropic turbulent flow field. Effect of the dispersed phases on the modulation of the turbulence are neglected. Large number for particles and bubbles are used to improve the collisions statistics. Particle and bubbles sizes are taken to be on the order of the smallest dissipative turbulent scales (i.e Kolmogorov$'$ length scale). Particles and bubbles are allowed to overlap during the course of the simulation. Particle-particle and particle-bubble interactions during collision have been neglected. During the simulation, particle-particle and particle-bubble collisions are monitored. Statistical properties of particles and bubbles turbulent dispersion are monitored as well.

Both Direct Numerical Simulations (DNS) and Large-Eddy Simulations (LES) have been used to simulate homogeneous isotropic turbulent flow field. In DNS no turbulence model is used, and all scales from the integral length scales down to the smallest dissipative scales are well resolved. In LES large scales are resolved and small scales are modeled. Effects of small scales on the motion of large scales are modeled to close the filtered momentum equations of the carrier phase. A spectral eddy viscosity model has been used to drain off the turbulent kinetic energy of the large scales. Eddy viscosity is *an ad-hoc* viscosity that is added to the fluid viscosity to stabilize the LES simulations. Small particles and bubbles are affected by the motion of the subgrid scales fluctuations which have been filtered in the frame work of LES. For accurate LES simulation of small particles and bubbles collisions, subgrid velocity fluctuations have to be added to the large resolved scales. But since those fluctuations are not available in the course of an LES, they must be modeled in terms of the

resolved velocity scales. A new methodology has been developed to construct the subgrid velocity components of wavenumbers higher than the cutoff wavenumber using a multifractal approach. The resolved and the modeled SGS velocity fields are used to solve the equations of motion of the dispersed phases. Another approach is to obtain a frozen subgrid scales from a DNS field and adding these frozen subgrid scales to a dynamically evolving LES field.

As an application of the fundamental research conduced in this dissertation, a CFD-based flotation kinetics model has been developed and applied for froth flotation machines such as Wemco and Dorr-Oliver machines. The model predicts local values of attachment and detachment rates in the pulp volume of a flotation machine. The CFD-based flotation model developed in this dissertation and the associated two-phase flow data have been transferred to engineers at FLSmidth Minerals Inc (Salt Lake City, UT, USA). They used the model to develop more efficient rotors and stators for their flotation machines [24] and to optimize the flotation process of fine and coarse particles [20]

1.2 Objectives

The objectives of this dissertation are

- Develop a method for computing the collision frequency of bi-dispersed particles in turbulent flows.
- Validate theoretical and empirical collisions frequency models using DNS and LES.
- Develop a CFD-based kinetics model for minerals flotation machines.

The first objective is to compute the particle-particle (mono-disperse) and particle-bubble (bi-disperse) collision kernel as a function of particle Stokes number using DNS and LES. This requires finding the instantaneous particles and bubbles positions. Equations of motion of each particle and bubble are solved to find the instantaneous position. Therefore, the instantaneous number of collisions can be monitored and averaged spatially and temporally to calculate collisions kernel. Radial distribution function and radial relative velocity are directly calculated during the course of simulation. A new methodology is developed to construct the subgrid scales from the cutoff wavenumber down to dissipative scales in the frame work of LES. The modeled subgrid velocity fluctuations in combination with the resolved large scale field are used to track particles and bubbles in LES simulations

The second objective is to validate Zaichik el al [78] and [79] models that are valid for small particles and arbitrary Stokes number, respectively. Other models including Saffman-Turner [53], and Schubert-Abrahamson [58] models have been also studied. Assessments of such models are required to show their limitations.

The third objective is to build a CFD-based flotation kinetics model that can predict the local attachment and detachment rates in pulp volume of minerals flotation machines. Local values of turbulent dissipation rate and air and water void fractions are the input for this CFD-based flotation model.

1.3 Outline

This dissertation is composed of the following chapters.

1- Introduction

2- Particles Collisions Frequency Models

3- Direct Numerical Simulations of Collisions Frequency

4- Large-Eddy Simulations of Collisions Frequency

5- Two-Phase Flow in Wemco-0.8 m^3 Cell and Application of CFD-Based Flotation Model

6- Numerical Simulations of Two-Phase Flow in a Dorr-Oliver Flotation Cell Model

7- Conclusions and Future Work

8- References

9- Appendices

Chapter 2

Particles Collisions Frequency Models

2.1 Introduction

Collisions frequency of dispersed phases suspended in a turbulent carrier phase is a deciding factor in many industrial processes such as minerals flotation, liquids purification and nuclear power generation. In this study, we are interested in collisions of solid particles and gas bubbles in a turbulent liquid motion. The particle and bubble sizes are on the order of the small scales of turbulent fluctuations, and hence those scales have strong effects on the motion of colliding particles.

Two well known theoretical models for collisions frequency are due to Saffman and Turner [53] and Abrahamson [1]. Saffman and Turner model is valid for colliding particles whose response times are small in comparison to Kolmogorov time scale of the turbulence, that is to say, in the limit of zero Stokes number. Abrahamson model is applicable for cases where inertia effects of the colliding particles are dominant, which is the case for very high Stokes number. However, most of the industrial applications involve particles of finite Stokes number. Applications of the previously mentioned collisions models for practical Stokes numbers either overestimate or underestimate the collisions frequency. Considerable efforts have been expended to develop a more general collisions model that is applicable in the entire range of particles Stokes number.

William and Crane [72] developed a model for the relative motion of two particles or droplets of an intermediate Stokes number in gaseous turbulent flow. The added mass effect experienced by the particles moving through the carrier phase were neglected and Stokes drag law was used. Yuu [73] derived a model for the fluctuating relative velocity of two inertial particles. This model takes into consideration the added mass effect on the particles motion as well as the turbulent shear effect. Kruis and Kusters [32] found that both models of William and Crane [72] and Yuu [73] are not applicable for particle sizes on the order of

the inertial subrange of turbulence and the models fail to approach the zero Stokes limit according to Saffman and Turner [53] model. The approaches of William and Crane [72] for large particles and that of Yuu [73] for small particles have been included in one model by Kruis and Kusters [32] to formulate a universal collisions model. This new model is based on a very low mass loading, isotropic turbulence, Stokes drag law and for particles that are larger than the mean free path of the fluid.

Two mechanisms contribute to collisions rate between two different species of particles in turbulent flows: the transport mechanism and the accumulation effects. The accumulation effects are accounted for by the radial distribution function at contact and the transport effects are accounted by the mean value of the particles radial relative velocity [82]. Zhou et al. [83] extended their DNS simulations of particulate isotropic turbulent flows of mono-dispersed inertial particles to bi-dispersed particles. They derived new model called eddy particle interaction (EPI) for high inertia particles. The fluid velocity in this model was treated as a Monte-Carlo stochastic process with a fixed eddy lifetime as a Gaussian. The developed EPI model can predict the collision kernel for particle response time in the order of eddy life time scale. The model does not give reasonable prediction for collisions kernel near Stokes number of unity.

Another way to describe the dispersed phase motion in a turbulent flow theoretically is to solve the kinetic equation for the particle velocity probability density function. Zaichik and Pershukov [81] solved a stochastic equation of Langevin type that describes the velocity PDF of a particle ensemble. This model takes into account both the interaction between the particles and fluid fluctuations and particle-particle collisions effects. Zaichik and Alipchenkov [80] developed two theoretical models to predict the effects of clustering of inertial particles in in-homogeneous and homogeneous turbulent flows. The first model is based on a one-point PDF of particle velocity distribution in Gaussian random field. This model predicts intensity of fluctuations and concentration of particles in flat channel and round pipe flow. The second model is based on two-point PDF of particle velocity distribution in random Gaussian field. This model predicts relative velocity of particle pairs and their radial distribution velocity in homogeneous isotropic turbulence. Zaichik et al. [78] have developed a model to predict the collisions frequency between two different inertia particles. Their approach involves solving a system of three nonlinear ordinary differential equations that describe the radial distribution function, longitudinal and transverse velocity structure functions. This model [78] has been developed for small particles and only Stokes drag is considered. Another algebraic collisions model has been developed by Zaichik et al. [79]. In this model Stokes drag, pressure gradient and added mass forces are considered. In this chapter, collisions kernel models and their parameters are summarized and presented.

2.2 Theoretical Models for Collisions Kernel

Theoretical models for collisions frequency of two groups of particles suspended in homogeneous isotropic turbulence have been developed by many authors. Let n_i and d_i denote the number concentration and diameter of particles belonging to group i, respectively. Homogeneous isotropic turbulence implies spherical symmetry of the relative velocity of two colliding particles, and the collisions frequency can be expressed as (see [70])

$$Z_{12} = \beta n_1 n_2 \tag{2.1}$$

where β is collision kernel defined by

$$\beta = 2\pi d^2 \langle |w_r(d)| \rangle g_{12}(d) \tag{2.2}$$

where $d = (d_1 + d_2)/2$ is the collision radius, $\langle |w_r| \rangle$ is the mean radial component of the relative velocity of the two colliding particles, and g_{12} is the radial distribution function at contact.

The particle inertia is quantified by the ratio of the particle response time τ_p to the Lagrangian integral timescale T_L of the carrier fluid. Particle of diameter d has a response time τ_p

$$\tau_p = \frac{\rho_p}{\rho_f} \frac{d^2}{18\nu_f} \tag{2.3}$$

According to Zaichick et al. [79], when the added mass force is considered, the effective particle response time

$$\tau_p^* = \tau_p \left(1 + C_A \frac{\rho_f}{\rho_p} \right) \tag{2.4}$$

should be used instead of τ_p and C_A is the added mass coefficient. In case of a bubble with negligible density the effective particle response time is

$$\tau_b^* = C_A \frac{d^2}{18\nu_f} \tag{2.5}$$

Also, the eddy-particle interaction timescale T_{Lp} defined as

$$T_{Lp} = (T_{Lp}^l + 2T_{Lp}^n)/3 \tag{2.6}$$

should be used instead of T_L. Here

$$T_{Lp}^l = T_L/(1 + C_\gamma \gamma^2)^{1/2} \tag{2.7}$$

$$T_{Lp}^n = T_L/(1+4C_\gamma\gamma^2)^{1/2} \tag{2.8}$$

where $C_\gamma = 0.45$, and $\gamma = |\mathbf{V}_r|/u'$ is the drift parameter. Thus, the particle inertia is quantified by

$$\Omega_i = \tau_i^*/T_{Li} \tag{2.9}$$

The collision kernel models presented in this work can be written in a non-dimensional form

$$\frac{\beta}{u'd^2} = f\left(\frac{d_1}{\eta}, \frac{d_2}{\eta}, \frac{\rho_1}{\rho_f}, \frac{\rho_2}{\rho_f}, Re_\lambda\right) \tag{2.10}$$

where $u' = (\langle u_k' u_k' \rangle /3)^{1/2}$ is the turbulence intensity, $\eta = (\nu_f^3/\epsilon)^{1/4}$ is the Kolmogorov microscale, and $Re_\lambda = u'\lambda/\nu_f$ is the Reynolds number based on the Taylor microscale $\lambda = (15\nu_f u'^2/\epsilon)^{1/2}$. It is important to note that the collision kernel depends on four independent properties of the colliding particles; namely their sizes relative to Kolmogorov microscale and densities relative to the carrier phase density. Stokes number defined by

$$St_i = \frac{1}{18}\frac{\rho_i}{\rho_f}\left(\frac{d_i}{\eta}\right)^2 \tag{2.11}$$

may be introduced as a combination of density and size but, in general, it is not sufficient to reduce the number of independent variables from four. Isotropic homogeneous turbulent fluctuations of carrier phase are also characterized by three independent parameters, namely u', η and Re_λ. Alternatively, we can use u', ϵ, and ν_f.

The non-dimensional collision kernel is related to the non-dimensional mean radial velocity of colliding particles by

$$\frac{\beta}{2\pi u' d^2} = \frac{\langle |w_r(d)| \rangle}{u'} g_{12}(d) \tag{2.12}$$

where $\langle |w_r(d)| \rangle$ is the mean radial relative velocity at contact and $g_{12}(d$ is the radial distribution function at contact of the colliding particles. Radial relative velocity of the colliding particles are a measure the transport rate and radial distribution function are a measure of the number density of particles pairs that undergo collisions. Zaichik et al. [78] model provides a values for $g_{12}(d)$, however, all other models presented here assume that $g_{12}(d) = 1$. For the latter models, the non-dimensional collision kernel is equal to the non-dimensional mean radial relative velocity,

$$\frac{\beta}{2\pi u' d^2} = \frac{\langle |w_r(d)| \rangle}{u'} \tag{2.13}$$

2.2.1 Saffman-Turner Model

For zero-inertia particles ($\Omega_1 = \Omega_2 = 0$), the collisions kernel is given by Saffman and Turner [53] model

$$\beta_{ST} = \left(\frac{8\pi\epsilon}{15\nu_f}\right)^{1/2} d^3 \tag{2.14}$$

$$\frac{\beta_{ST}}{u'd^2} = \left(\frac{8\pi}{\sqrt{15}}\right)^{1/2} \frac{1}{\sqrt{Re_\lambda}} \frac{d}{\eta} \tag{2.15}$$

where $d = (d_1 + d_2)/2$. Assuming $g_{12} = 1$, we obtain a non-dimensional mean radial relative velocity

$$\frac{\langle |w_r(d)| \rangle_{ST}}{u'} = \frac{1}{2\pi} \left(\frac{8\pi}{\sqrt{15}}\right)^{1/2} \frac{1}{\sqrt{Re_\lambda}} \frac{d}{\eta} \tag{2.16}$$

For particles-bubbles collision, we have $d = (d_p + d_b)/2$.

2.2.2 Abrahamson-Schubert Model

For high inertia particles, Abrahamson [1] model gives

$$\beta_A = (8\pi)^{1/2} d^2 \left(U_1^2 + U_2^2\right)^{1/2} \tag{2.17}$$

where the root-mean-square velocity for each particle is

$$U_i = \frac{u'}{\left(1 + 1.5\tau_i\epsilon/u'^2\right)^{1/2}} \tag{2.18}$$

and τ_i is the particle response time. The non-dimensional mean radial relative velocity is given by

$$\frac{\langle |w_r(d)| \rangle_A}{u'} = \left(\frac{2}{\pi}\right)^{1/2} \left[\left\{ 1 + \frac{\sqrt{15}}{12\sqrt{Re_\lambda}} \frac{\rho_1}{\rho_f} \left(\frac{d_1}{\eta}\right)^2 \right\}^{-2} + \left\{ 1 + \frac{\sqrt{15}}{12\sqrt{Re_\lambda}} \frac{\rho_2}{\rho_f} \left(\frac{d_2}{\eta}\right)^2 \right\}^{-2} \right]^{1/2} \tag{2.19}$$

This model depends only the Stokes numbers of the colliding particles

$$\frac{\langle |w_r(d)| \rangle_A}{u'} = \left(\frac{2}{\pi}\right)^{1/2} \left[\left\{ 1 + \frac{3\sqrt{15}}{2\sqrt{Re_\lambda}} St_1 \right\}^{-2} + \left\{ 1 + \frac{3\sqrt{15}}{2\sqrt{Re_\lambda}} St_2 \right\}^{-2} \right]^{1/2} \tag{2.20}$$

In mineral flotation literature Eq(2.17) is still used but the root-mean-square velocity for the particles are replaced by root-mean-square of the velocity fluctuations of the colliding

particles (solid particles and air bubbles) relative to the carrier phase (water), where the latter velocities are given by Leipe and Mockel [35] (see also [59] and [58]].

$$U_i = \frac{0.4\epsilon^{4/9} d_i^{7/9}}{\nu_f^{1/3}} \left(\frac{\Delta\rho_i}{\rho_f}\right)^{2/3} \tag{2.21}$$

where $\Delta\rho_i = |\rho_i - \rho_f|$. The model obtained by substituting Eq(2.21) into Eq(2.17) will be called the Abrahamson-Schubert model to distinguish it from the original Abrahamson model. Its kernel is denoted by β_{AS}. In non-dimensional form it is written as

$$\frac{\beta_{AS}}{u' d^2} = \frac{0.4(8\pi\sqrt{15})^{1/2}}{\sqrt{Re_\lambda}} \left[\left(\frac{d_1}{\eta}\right)^{14/9} \left(\frac{\Delta\rho_1}{\rho_f}\right)^{4/3} + \left(\frac{d_2}{\eta}\right)^{14/9} \left(\frac{\Delta\rho_2}{\rho_f}\right)^{4/3}\right]^{1/2} \tag{2.22}$$

It is implicitly assumed $g_{12} = 1$, and hence the non-dimensional mean radial relative velocity is

$$\frac{\langle |w_r(d)| \rangle_{AS}}{u'} = \frac{1}{2\pi} \frac{0.4(8\pi\sqrt{15})^{1/2}}{\sqrt{Re_\lambda}} \left[\left(\frac{d_1}{\eta}\right)^{14/9} \left(\frac{\Delta\rho_1}{\rho_f}\right)^{4/3} + \left(\frac{d_2}{\eta}\right)^{14/9} \left(\frac{\Delta\rho_2}{\rho_f}\right)^{4/3}\right]^{1/2} \tag{2.23}$$

In applying Abrahamson and Abrahamson-Schubert models to particles-bubbles collisions, the bubble density ratio is assumed to be $\rho_b/\rho_f = 1/2$.

2.2.3 Zaichik-Simonin-Alipchenkov Model-2006

Zaichik et al. [78] presented two statistical models for predicting collision kernel of bi-disperse heavy particles in homogeneous isotropic turbulence. In the present work we will use the second model and refer it as Zaichik-2006 model. *Strictly speaking, application of this model should be limited to heavy small particles. Its application to the case of particle-bubble collisions may be questionable, but will be presented here only for reference.* The collision kernel β_{Z06} is given by

$$\frac{\beta_{Z06}}{u' d^2} = \left[\frac{8\pi S_{pll}(d)}{u'^2}\right]^{1/2} g_{ij}(d) \tag{2.24}$$

where S_{pll} is the longitudinal component of the particle velocity structure function evaluated at the collision radius $d = (d_1 + d_2)/2$. For this model the non-dimensional mean radial relative velocity is

$$\frac{\langle |w_r(d)| \rangle_{Z06}}{u'} = \frac{1}{2\pi} \left[\frac{8\pi S_{pll}(d)}{u'^2}\right]^{1/2} \tag{2.25}$$

To compute the collisions kernel, a two-point boundary-value problem governed by three coupled nonlinear ordinary-differential equations must be solved for particle velocity structure functions and radial distribution function, Zaichik et al. [78]. The system of three

equations are replaced by an equivalent system of five first-order equations that are solved using MATLAB. To execute the model and obtain the non-dimensional kernel and relative velocity, we must specify four parameters, namely the particles Stokes numbers St_1 and St_2, the collision radius d/η, and Taylor micro-scale Reynolds number Re_λ of the carrier phase. The particle density does not appear explicitly in the model; its effects appear only through the particle Stokes number.

2.2.4 Zaichik-Simonin-Alipchenkov Model-2010

Zaichik et al. [79] developed a statistical model for the collisions kernel of bi-disperse particles. The model applies to arbitrary values of density ratio and particle sizes. They defined a particle-to-fluid density parameter

$$A_i = \frac{1 + C_A}{\rho_i/\rho_f + C_A} \tag{2.26}$$

In Zaichik et al. [79], no distinction between A_1 and A_2 is made, and hence the parameter A appears unsubscripted in their formulas. In this work, we are interested in the collisions of solid particles with air bubbles in liquid, and hence the value of A_p is significantly different from that of A_b. Thus the formulas presented here take into consideration the different values of the particle-to-fluid density parameter for the two groups of colliding particles. For this model the non-dimensional mean radial relative velocity is

$$\frac{\langle |w_r(d)| \rangle_{Z10}}{u'} = \left(\frac{2}{\pi}\right)^{1/2} \left[\left(\frac{v_1'}{u'}\right)^2 + \left(\frac{v_2'}{u'}\right)^2 - 2\zeta_{12} \frac{v_1'}{u'} \frac{v_2'}{u'} \right]^{1/2} \tag{2.27}$$

$$\frac{v_i'}{u'} = \left[\frac{2\Omega_i + 2A_i^2\Omega_i^2 + z^2}{2\Omega_i + 2\Omega_i^2 + z^2} \right]^{1/2} \tag{2.28}$$

$$\zeta_{12} = \xi_1 \xi_2 F(d) \tag{2.29}$$

$$\xi_i = \frac{2\Omega_i + 2A_i\Omega_i^2 + z^2}{\left[(2\Omega_i + 2A_i^2\Omega_i^2 + z^2)(2\Omega_i + 2\Omega_i^2 + z^2)\right]^{1/2}} \tag{2.30}$$

$$F(d) = 1 - \left[1 - exp\left(-\frac{d/\eta}{(15C)^{3/4}}\right)\right]^{4/3} \left[\frac{15^3 (d/\eta)^4}{15^3 (d/\eta)^4 + (2Re_\lambda/C)^6}\right]^{1/6} \tag{2.31}$$

where $C = 2$, and $z = \tau_T/T_L$. Zaichik et al. [79] provided

$$T_L = \frac{2(Re_\lambda + 32)}{7\sqrt{15}} \left(\frac{\epsilon}{\nu_f}\right)^{1/2} \tag{2.32}$$

$$\tau_T = \left(\frac{2Re_\lambda}{a_o\sqrt{15}}\right)^{1/2} \left(\frac{\epsilon}{\nu_f}\right)^{1/2} \tag{2.33}$$

$$a_o = \frac{11 + 7Re_\lambda}{205 + Re_\lambda} \tag{2.34}$$

In minerals flotation industry, Abrahamson [1] model is widely used which is applicable for very high inertia particles. However particles in minerals flotations and other industrial applications have a wide range of Stokes number. Collisions models developed by Zaichik et al. [78] and [79] are applicable for a wide range of particles inertia. Zaichik-2006 [78] model provides radial relative velocity and radial distribution function while as Zaichik-2010 [79] model assumes radial distribution function of unity. Therefore, assessment of these models should be based on the comparison with DNS and LES for the radial relative velocity and radial distribution function instead of collisions kernel only.

Chapter 3

Direct Numerical Simulations of Collisions Frequency

3.1 Introduction

Three phase flow is composed of a carrier phase, and two dispersed phases which are solid particles and gaseous bubbles. Dispersed phases (particles or bubbles) respond to a wide range of turbulent scales according to their response time. The turbulent motion of the carrier phase is a homogeneous isotropic turbulent flow. Rogallo and Moin [52], among others, have demonstrated the viability of direct numerical simulations (DNS) for reproducing experimentally obtained data for many turbulent flows. Direct Numerical simulation (DNS) of the carrier phase is performed where all turbulent scales are well resolved and represented on the computational grid. No turbulence models are used with DNS. A pseudo-spectral DNS code has been developed to simulate homogeneous isotropic turbulence. In this chapter a method for computing the collision frequency of bi-dispersed particles in turbulent flows is developed. Theoretical models developed by Zaichik et al. [78] Zaichik et al. [79] are validated using radial relative velocity, radial distribution function and collisions kernel computed from DNS.

3.2 Direct Numerical Simulation (DNS)

3.2.1 Governing Equations for DNS

The flow field is a homogeneous isotropic turbulence in a periodic cube of side 2π. This turbulent flow is governed by the incompressible Navier-Stokes equations. Viscous effects dissipate the turbulent kinetic energy, and in the absence of external forcing the turbulence

will decay. Therefore, a forcing term is added to maintain statistically stationary turbulent flow field. Navier-Stokes equation can be written in the following form

$$\nabla.\vec{u} = 0 \tag{3.1}$$

$$\frac{\partial \vec{u}}{\partial t} + \vec{u}.\nabla\vec{u} = -\frac{1}{\rho_f}\nabla p + \nu_f \nabla^2 \vec{u} + \vec{F} \tag{3.2}$$

Herein $\vec{u}$ is the instantaneous velocity field, ρ_f is the density of the carrier phase and $p(\vec{x}, t)$ is the pressure field. Viscous effects dissipate the turbulent kinetic energy, and in the absence of external forcing the turbulence will decay. Therefore, a forcing term "$\vec{F}$ " is added to the RHS of Eq(3.2) to maintain statistically stationary turbulent flow field. The forcing vector is constructed in such a way as to make it divergence free, hence $\nabla.\vec{F} = 0$. The Fourier-Galerkin approach [8] has been used to rewrite Navier-Stokes equations in the Fourier space and have been solved in spectral domain. We demonstrate this approach by writing Navier-Stokes equation in spectral domain. Eqs 3.3 and 3.4 representing Navier-Stokes equation in spectral domain.

$$i\vec{K}.\widehat{\vec{u}} = 0 \tag{3.3}$$

$$\frac{\partial \widehat{\vec{u}}_{\vec{K}}}{\partial t} = \widehat{C}_{\vec{K}} + -\frac{i}{\rho_f}\vec{K}\widehat{p}_{\vec{K}} - \nu \left|\vec{K}\right|^2 \widehat{\vec{u}}_{\vec{K}} + \widehat{\vec{F}}_{\vec{K}} \tag{3.4}$$

where $\vec{K}$ is the wavenumber vector and $\widehat{\vec{C}} = -\widehat{\vec{u}.\nabla\vec{u}}$.

In this method, the acceleration of all Fourier modes in the forced range is augmented by random (in time) components, which are given by Ornstein-Uhlenbeck (OU) stochastic processes (e.g. Gillespie [19]). The OU process is defined by its standard deviation σ' and relaxation time scale τ'.

Following Eswaran and Pope [13] this forcing term is added to a range of low wavenumbers, $0 < k \leq K_f$, where K_f represents a radius of a sphere in the spectral space centered at the origin. Only modes within this sphere in the spectral domain are forced. This allow the added energy to cascade from low wavenumbers to high wavesnumbers because of the convective term $\vec{u}.\nabla\vec{u}$ in Navier-Stokes equation.

The forcing term in Eq(3.4) takes the form

$$\vec{\hat{F}}_{\vec{K}} = \vec{\hat{b}}_{\vec{K}} - \vec{K}\frac{\vec{K}.\vec{\hat{b}}_{\vec{K}}}{\left|\vec{K}\right|^2} \tag{3.5}$$

and $\vec{\hat{b}}_{\vec{K}}$ is a complex vector that is computed for the current time step $n+1$ from the previous time step n as follows

$$\left(\vec{\hat{b}}_{\vec{K}}\right)^{n+1} = \left(\vec{\hat{b}}_{\vec{K}}\right)^{n} e^{-\Delta t/\tau'} + \sigma' \left(\vec{\hat{R}}_{\vec{K}}\right)^{n} \sqrt{1 - exp(-2\Delta t/\tau')} \tag{3.6}$$

where $\vec{\hat{R}}_{\vec{k}}$ is a complex-valued vector whose components are normally distributed (Gaussian) random numbers with zero mean and unit variance (e.g. Press et al. [45]). The forcing term is updated at the beginning of each time step using Eqs(3.5) and (3.6), but it is held constant during the sub-steps of the time integration scheme. For the construction of the forcing term in the spectral domain, it is important to satisfy $\vec{\hat{F}}_{\vec{K}}(-\vec{K}) = \vec{\hat{F}}^{*}_{\vec{K}}(\vec{K})$, where modes of the forcing wavenumbers equals their complex conjugate.

Pressure term in Eq 3.4 is obtained by projecting this equation onto the wavenumber vector $\vec{K}$ and use the fact that this flow field is divergence free as well as the forcing term. The pressure term can be written as the following

$$\frac{\widehat{p}}{\rho_f} = -i\frac{\vec{K}.\widehat{\vec{C}}}{\left|\vec{K}\right|^2} \tag{3.7}$$

Convective nonlinear term is treated by a pseudo-spectral method and 3/2-rule for de-aliasing. In this method velocity field is interpolated spectrally to a finer grid $3N/2$ times the size of the DNS N grid. The term pseudo-spectral is due to computing the convective term on the finer grid nodes in the physical domain. A fast Fourier transform is used to obtain the convective acceleration term in spectral domain. In the finer grid $3N/2$, modes of wavenumbers higher than the maximum wavenumbers represented on the DNS N grid are aliased. De-aliasing takes place by considering only the modes of wavenumbers in the finer $3N/2$ grid up to the maximum wavenumber in the DNS N grid.

Following Rogallo [51] we use an integrating factor $e^{\nu_f \left|\vec{K}\right|^2 (t-t_n)}$ and Eq 3.4 can be rewritten as

$$(\frac{d}{dt} + \nu_f \left|\vec{k}\right|^2)\vec{\hat{u}}_{\vec{K}} = \vec{\hat{C}}_{\vec{K}} - \vec{K}\frac{\vec{K}.\vec{\hat{C}}_{\vec{K}}}{\left|\vec{K}\right|^2} + \vec{\hat{F}}_{\vec{K}} \tag{3.8}$$

Therefore, the limitation on the time step for stability is determined by the convective term. A low-storage third-order Runge-Kutta method [8] is used for time advancement.

$$\frac{d}{dt}\left[\widehat{\vec{u}}e^{\nu_f\left|\vec{K}\right|^2(t-t_n)}\right] = e^{\nu_f\left|\vec{K}\right|^2(t-t_n)}\left[\vec{\hat{C}}_{\vec{K}} - \vec{K}\frac{\vec{K}.\vec{\hat{C}}_{\vec{K}}}{\left|\vec{K}\right|^2} + \vec{\hat{F}}_{\vec{K}}\right] \tag{3.9}$$

3.2.2 Statistical Turbulent Properties

In spectral domain each Fourier mode of the turbulent 3D signal has a specific spectral radius k equal to $\sqrt{\left|\vec{K}\right|^2}$. Spectral domain is divided into a set of spherical shells that have the same center at wavenumber zero. Each spherical shell has a mean radius k_n and constant radial thickness dk_n.

All Fourier modes that lie within each spherical shell are found and their kinetic energies are summed to provide the energy in the shell.

$$E(k_n) = \frac{1}{2}\int_{\xi=k_n-\frac{dk_n}{2}}^{\xi=k_n+\frac{dk_n}{2}} \left|\widehat{\vec{u}}_{\vec{K}}(\xi)\right|^2 d\xi \tag{3.10}$$

The maximum value of k_n is $\frac{N}{2}$.

The instantaneous value provided by the integral 3.10 is then averaged over the simulation time after a transient period. The $r.m.s$ of the turbulent velocity (u') are computed from the energy spectrum.

$$\frac{3}{2}u'^2_{r.m.s} \equiv \frac{1}{2}q^2 = \int_0^{k_{max}} E(k)dk \tag{3.11}$$

and turbulent dissipation rate (ϵ) are calculated from the energy spectrum as well

$$\epsilon = 2\nu_f \int_0^{k_{max}} k^2 E(k)dk \tag{3.12}$$

where ν_f is the fluid kinematic viscosity. The 3D instantaneous energy, dissipation rate spectra and $r.m.s$ of the turbulent velocity ($u'_{r.m.s}$) are then averaged over time.

The Lagrangian integral length scale L_f is calculated as

$$L_f = \frac{\pi}{2u'_{r.m.s}}\int_0^{k_{max}} \frac{E(k)}{k}dk \tag{3.13}$$

Integral time scale (i.e eddy life time) can also be defined according to Eq 3.14

$$T_e \equiv \frac{L_f}{u'_{r.m.s}} \tag{3.14}$$

Taylor microscale λ is written as

$$\lambda = \sqrt{\frac{15\nu_f u'^2_{r.m.s}}{\epsilon}} \tag{3.15}$$

and the dissipative length scale η (i.e Kolmogorov scale) is defined by

$$\eta = \sqrt[4]{\frac{\nu_f^3}{\epsilon}} \tag{3.16}$$

3.3 Dispersed Phase Model

Dispersed phases are a system of particles and bubbles that move within the turbulent flow field. Equations of motion of the dispersed phases are solved to find instantaneous positions and velocities of particles and bubbles within the turbulent flow field. This treatment is well known by Eulerian-Lagrangian approach. In this section we are presenting the equation of motion of particles and bubbles. Stokes drag, added mass and pressure gradient forces are considered. Sizes of particles and bubbles are on the order of Kolmogorov′s length scale. An incomplete 3D Hermite interpolation scheme is used to find fluid velocities and tri-linear interpolation to find fluid accelerations at the center of each particle and bubble (see Appendix A). The interpolated fluid velocities and accelerations are used to integrate equations of motion of each dispersed phase. Collisions detection algorithm is presented in this chapter. A method to calculate radial distribution function (RDF) and radial relative velocity is presented.

The size of the dispersed phases are considered to be small (i.e particles and bubbles sizes are order of Kolmogorov′s length scale). Therefore point mass particles and/or bubbles assumption becomes feasible. Effects of the generated turbulent scales in the wake of the particles and bubbles are neglected because these scales are smaller than the particles and bubbles sizes and they are in the dissipative range of turbulent scales.

A system of solid particles and gas bubbles are tracked by solving Newton's equation of motion Eq 3.17. No limitations are imposed on the particle density. The added mass and pressure gradient terms are accounted for in the equations of motion as well as Stokes drag. The added mass and pressure gradient terms are essential when taking about bi-dispersed phases [22].

$$\frac{d\vec{V}_i(t)}{dt} = \frac{\vec{u}_f - \vec{V}_i(t)}{\tau_i} + \frac{\rho_f}{\rho_i}\frac{D\vec{u}_f}{Dt} + C_A\frac{\rho_f}{\rho_i}(\frac{D\vec{u}_f}{Dt} - \frac{d\vec{V}_i(t)}{dt}) \tag{3.17}$$

$$\frac{d\vec{X}_i(t)}{dt} = \vec{V}_i(t) \tag{3.18}$$

where $\vec{X}_i(t)$ and $\vec{V}_i(t)$ are the instantaneous position and velocity of particle i ($i = p$ for solid particles, and $i = b$ for bubbles). $\vec{u_f}$ and $D\vec{u}_f/Dt$ are the carrier phase velocity and acceleration evaluated at the instantaneous particle center. On the right side of Eq (3.17), the first term is the Stokes drag, the second term is the effect of pressure gradient in the carrier phase, and the third term is the effect of added (virtual) mass. The lift and Basset (or history) forces are neglected in this study basically to be consistent with the collision frequency theoretical models. There is no difficulty in including the lift force as it depends on the local vorticity vector and shear that are readily available in the course of simulation. The Basset force is important for gas bubbles in high frequency liquid turbulence as supported by experimental data (e.g. L'Espérance et al. [36]). Hjelmfelt and Mockros [23] showed analytically that the added mass force, pressure gradient, and Basset terms are all important for bubble motion in liquid turbulence. Their results also showed that neglecting only the Basset force can still produce reasonable amplitude and phase of bubble motion. However, the effects of the Basset force on the mean motion of particles and bubbles may not be significant as shown theoretically by Ahmadi and Goldschmidt [2]. Inclusion of the Basset force in particle tracking requires high computing resources especially when large numbers of particles and bubbles are used as in this study. Van Hinsberg and Boonkkamp [67] has developed an efficient method for computing the Basset force that might be helpful in future studies of the effects of such a force on collision frequency.

Under quiescent condition, gravity will influence the relative velocity of particles and bubbles, and hence the collision rate. However, for turbulent environment the dominant mechanism of collisions due to turbulence fluctuations. The present study isolates he effects of turbulence fluctuations from gravity effects. For practical applications such as mineral froth flotation, the turbulence dissipation rate is the controlling parameter of particle bubble collision.

Rearranging terms, we rewrite Eq(3.17) as

$$\frac{d\vec{V}_i(t)}{dt} = \frac{\vec{u}_f - \vec{V}_i(t)}{\tau_i^*} + A\frac{D\vec{u}_f}{Dt} \tag{3.19}$$

where

$$\tau_i^* = \tau_i(1 + C_A\frac{\rho_f}{\rho_i}) \tag{3.20}$$

and

$$A = \frac{1 + C_A}{\rho_i/\rho_f + C_A} \tag{3.21}$$

For gaseous bubbles $\rho_b/\rho_f \approx 0$, and hence Eqs(3.20) and (3.21) can be rewritten as

$$\tau_b^* = C_A \frac{d_b^2}{18\nu} \tag{3.22}$$

and

$$A = 1 + 1/C_A \tag{3.23}$$

Thus for spherical bubbles with $C_A = 0.5$ we get $A = 3$. If we neglect the effects of pressure gradient then $A = 1$. On the other hand, for heavy particles ($\rho_{pi}/\rho_f \gg 1$), we get $A = 0$.

Particle-particle and particle-bubble interactions are neglected. The response time defined as $\tau_{pi} = \rho_{pi} d_{pi}^2/18\mu$ is a measure of the particle inertia. Particle Stokes number is the ratio of the particle response time to the Kolmogorov time scale.

$$St_i = \frac{\tau_i}{\tau_K} \tag{3.24}$$

In Eq(3.19) fluid velocity and acceleration at the particles instantaneous position are found by interpolation. High order Lagrange interpolations produces large error oscillations at high velocity gradient regions whereas 3D Hermite interpolation does not produces such large errors. Therefore, an incomplete 3D Hermite interpolation is applied to find fluid velocities. Hermite interpolation requires fluid velocity components and their spatial derivatives at the eight corners of the cell containing the particle center. Spectral representation of the fluid velocity allows us to calculate velocity gradient accurately at the grid nodes. One velocity component and three derivatives at each corner, allow for a 32 degrees of freedom interpolation formula. The formula is given in Appendix (A). Tri-linear interpolation is used to determine fluid acceleration at center of each particle and bubble; interpolation formula is also given in Appendix (A).

In the present DNS, the values of dispersed phases void fraction exceed the accepted values for the validity of one-way coupling. This is because of the large number of bubbles and particles used in DNS. However, there are no interactions among the groups of dispersed phases; each particle and each bubble moves as if the other bubbles and particles did not exist in the turbulent field. We used large number of bubbles and particles to obtain large samples for collisions statistics. Furthermore, the neglect of the two-way coupling and pseudo turbulence is consistent with theoretical models that are used for comparison as well as other DNS of collisions kernel. Those effects are important and deserve a separate study.

3.4 Collisions Frequency Calculations

3.4.1 Collisions Kernel

Geometric collision of particle-particle and/or particle-bubble is considered. Particles and bubbles sizes are on the order of Kolmogrov′s length scale. Two different methods are used and compared to calculate collision kernel of mono-disperse and bi-disperse phases. The first method calculates the collisions rate of the particles and/or bubbles that are involved in a collision by direct counting following Sundaram et al. [63]. As shown in figure 3.1 three different types of collisions are presented. In type (I) collisions, the two particles are completely separated at the beginning of the time step and overlapped at the end of the time step. Some other particles may appear separated at the beginning and at the end of the time step but they are overlapped during the time step. This type of collisions is denoted as type (II). In the third type of collisions, the two particles are overlapped at the beginning and at the end of the time step but non-overlapped at some instant during the time step. It is clear from these three different scenarios that a collision event is considered if and only if the two particles were separated before getting overlapped, or vice versa which means that if these two particles remains overlapped or separated during the time step no collision event is considered. Wang et al. [68] assumed that the second and third types of collisions can be neglected since the time step is small enough. In this work, type (I) is directly computed based on the current and former positions of the particles to check for overlap and non-overlap conditions at the end and at the beginning of the time step. For those particles that were non-overlapped at the end and beginning of the time step, type (II) of collisions is checked. Based on the initial relative position and radial relative velocity of the colliding pairs, the time required for collision is estimated within the computational time step according to Eq 3.25 where $d = \frac{d_1+d_2}{2}$ is the mean collision radius of the two colliding particles. A collision event is recorded if the solution of Eq 3.25 for t_c is only positive and less than or equal to the computational time step ($0 \leq t_c \leq \Delta t$), Sundaram et al. [63]. Collisions detection algorithm is shown in figure 3.2 to compute collision kernel by direct counting.

Collision frequency is defined as the number of (particle-particle or particle-bubble) collisions per unit time per unit volume. Direct counting of particles-particles collisions involves $O(N_p^2)$ operations. Considering the high number of particles N_p this process is computationally expensive. Instead, the computational domain is divided into smaller sub-domains such that the search for particles encountering a certain particle will be in this smaller domain. According to Sundaram and Collins [64] the savings in computation time are proportional to the number of sub-domains of the system of particles. In our study we used 16^3 sub-domains. The collisions count are averaged over time and normalized by the number density of the colliding species to find the collision kernel as shown in Eq 3.26 and Eq 3.27.

$$|\vec{r}_{oi} - \vec{r}_{oj} + t_c\,(\vec{v}_{oi} - \vec{v}_{oj})| = d \tag{3.25}$$

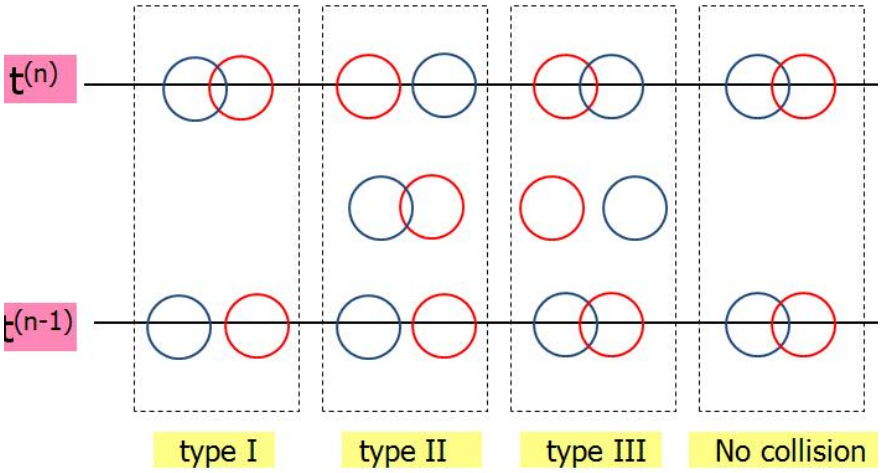

Figure 3.1: Collision types

where $\vec{r}_{oi}$ and $\vec{v}_{oi}$ are the initial particle position and velocity vectors at the beginning of the time step. Collisions kernel for particle-particle and particle-bubble calculated from the direct counting can written as,

$$\beta_{pp} = \frac{\left\langle \dot{N}_{pp} \right\rangle}{n_p n_p} \tag{3.26}$$

$$\beta_{pb} = \frac{\left\langle \dot{N}_{pb} \right\rangle}{n_p n_b} \tag{3.27}$$

where $\left\langle \dot{N}_{pb} \right\rangle$ and $\left\langle \dot{N}_{pb} \right\rangle$ are the spatial average of collision frequency per unit volume and n_p and n_b are the number density of the colliding particles and bubbles.

Two main statistical variables contribute to the collision kernel of the colliding particles; average radial relative velocity of the two colliding species $\langle |w_r(d)| \rangle$ and radial distribution function at contact g_{pp} or g_{pb}. Average radial relative velocity of the two colliding species $\langle |w_r(d)| \rangle$ is a measure of the transport effects and radial distribution function at contact g_{pp} or g_{pb} is a measure of the accumulation effects. The second method is to estimate collisions kernel using these two statistical variables based on spherical formulation. Following Wang et al. [69] and Wang et al. [70] spherical formulation is more accurate than the cylindrical formulation. Figure 3.3 shows a general description of spherical formulation used to calculate average radial relative velocity of the two colliding species $\langle |w_r(d)| \rangle$ and radial distribution function at contact g_{pp} or g_{pb}.

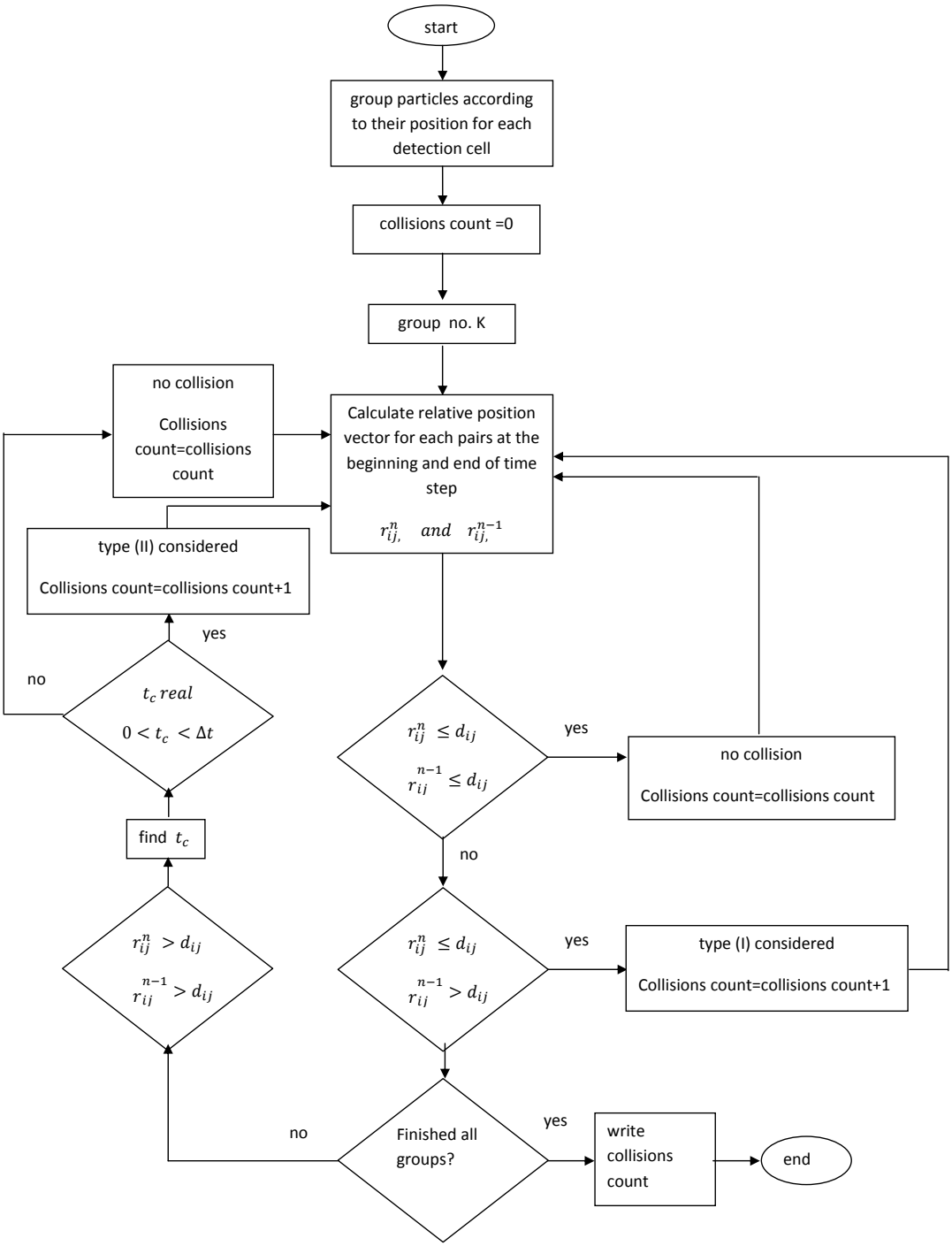

Figure 3.2: Collisions detection algorithm

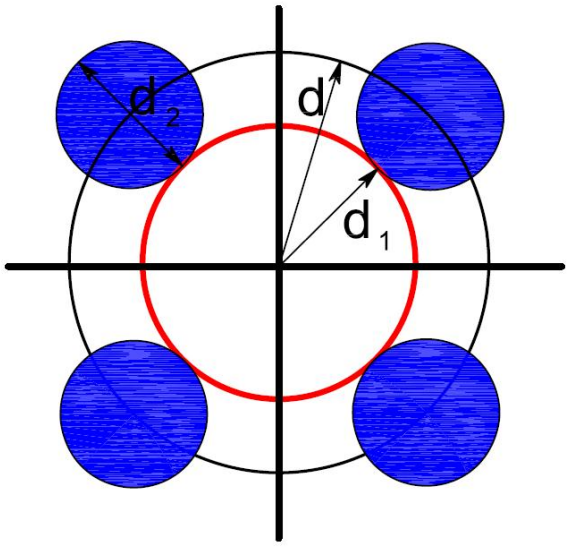

Figure 3.3: Geometric description of spherical formulation

The estimated collision kernel is calculated according to Eq 3.28 for particle-particle and Eq 3.29 for particle-bubble collisions. The following subsections discuss the calculation of RDF and radial relative velocity of the colliding species.

$$\beta_{pp(est.)} = 2\pi d^2 \langle |w_r(d)| \rangle \, g_{pp}(d) \tag{3.28}$$

$$\beta_{pb(est.)} = 2\pi d^2 \langle |w_r(d)| \rangle \, g_{pb}(d) \tag{3.29}$$

3.4.2 Radial Distribution Function and Radial Relative Velocity

Radial distribution function (RDF) at contact is a measure of the average colliding particles concentration. It can be defined as the ratio of the spatial average of number of pairs at contact per unit volume of the spherical shells ($\overline{N_{lm}}$) to the average number of possible pairs per unit volume of the computational box ($N_l \times N_m$) where particles are assumed to be uniformly distributed within the computational domain.

$$g_{lm}(d) = \frac{\langle \overline{N_{lm}} \rangle}{N_l \times N_m} \; l = 1, 2 \; m = 1, 2 \tag{3.30}$$

where ($d = (d_m + d_l)/2$) is the collision radius. Index (1) denotes particles and (2) denotes bubbles. Repeated indices imply a mono-disperse case. N_l and N_m, is the total number of

particles and bubbles in the computational domain, respectively. Wang et al. [70] used a spherical shell of radial thickness, r, $(d(1-\frac{\delta}{2}) < r < d(1+\frac{\delta}{2}))$ and δ chosen to be 2%. Each time step, total number of pairs that exists within the spherical shells is monitored then averaged over the total number of time steps. Eq (3.30) is rewritten as

$$g_{lm}(d) = \frac{N_{lm-total\ pairs} \times V_{box}}{V_{shell} \times N_t \times N_l N_m} \tag{3.31}$$

where (N_t) is the total number of time steps used to count for the total number of pairs at contact, and $(V_{box} = (2\pi)^3)$.

In this study, the two colliding particles are not necessarily of equal sizes as given in Table 3.2. Particles and bubble are allowed to overlap which is consistent with existing theoretical models. Under this condition, the calculations of RDF and $(\langle|w_r(d)|\rangle)$ are sensitive to the shell inner and outer radii. It is found that the use of a spherical shell with radial distance r in the range $(d(1-\frac{\delta}{2}) < r < d(1+\frac{\delta}{2})\ )$ underpredicts the radial distribution function. This is due to some particles or bubbles that contributes to the collision kernel in the direct counting are being overlapped while their centers fall outside the shell, and hence they do not contribute to the radial distribution function. Instead, we use a spherical shell of radius in the range $(\min(r_{p1}, r_{p2}) < r < d(1+\frac{\delta}{2}))$ to capture the contribution of such particles and obtain a more realistic values for the radial distribution function (RDF). However, the radial relative velocity $(\langle|w_r(d)|\rangle)$ has to be calculated within a spherical shell as recommended by Wang et al. [70] as it counts for the mass flux of the colliding particles as computed in Eqs (3.28) and (3.29) at the collision radius. We used $\delta = 4\%$. The ratio of the statistical estimated kernel to the direct computed kernel are depicted in figures 3.4a-3.4d, The ratio is close to one except for Stokes number near unity where the deviation from one is around 10%.

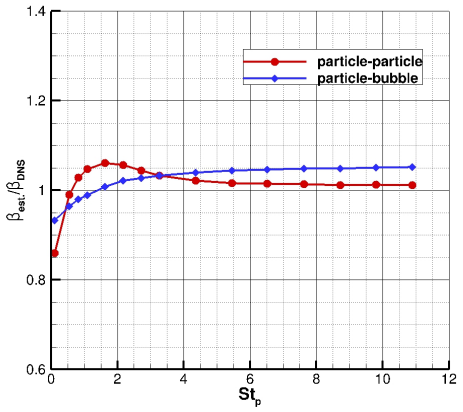

(a) $Re_\lambda = 57$, $N = 64$

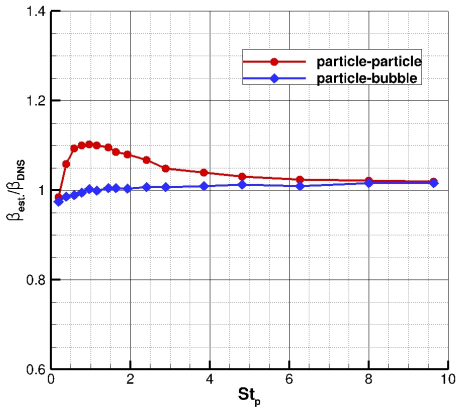

(b) $Re_\lambda = 77$, $N = 128$, simulation (II)

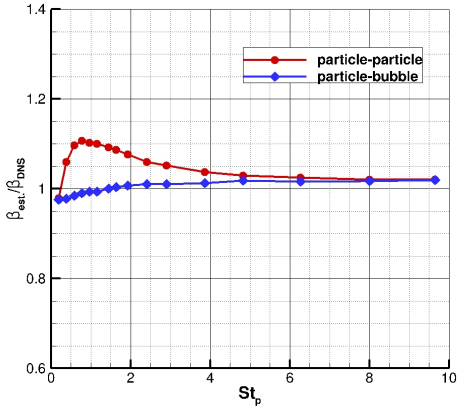

(c) $Re_\lambda = 77$, $N = 128$, simulation (III)

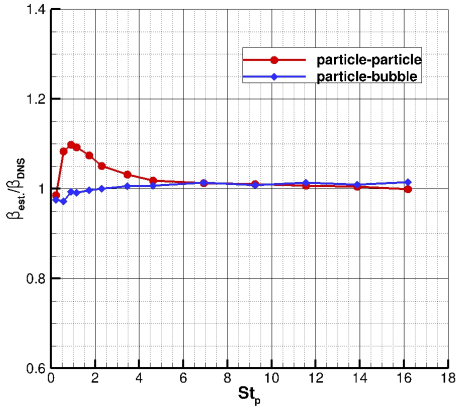

(d) $Re_\lambda = 96$, $N = 256$

Figure 3.4: Ratio of estimated collision kernel to directly counted collision kernel

3.5 Results

Navier-Stokes equation is a deterministic equation that is highly sensitive to initial conditions. Different initial conditions gives different instantaneous realizations. However, mean statistical properties of the turbulent flow fields are the same for the same turbulent Reynolds number. Turbulent kinetic energy and turbulent dissipation rate spectra have been validated by comparison with other results in the literature. In order to precisely assess the performance of theoretical models, collision kernel, radial distribution function (RDF) and radial relative velocity of the colliding species are compared with the same quantities computed in frame work of DNS.

3.6 DNS Code Validation

The computational domain is a cube of side B. We introduce a reference length $L_r = B/2\pi$, and a reference velocity V_r. Since the flow is incompressible, these two reference values are sufficient to non-dimensionalize all dependent (velocity) and independent variables (time and space coordinates). The input parameters that define the forced isotropic turbulence are: number of grid nodes in each space direction, N, range of forced Fourier modes, K_f, kinematic viscosity ν_f, standard deviation, σ, and time scale, τ, of Ornstein-Uhlenbeck stochastic process. All of these parameters are made non-dimensional by L_r and V_r. Different simulation parameters are summarized in Table (3.1).

The DNS spectra have been validated by comparisons with DNS spectra obtained by Eswaran and Pope [13] for $Re_\lambda = 54.1$ (the comparisons are not shown here). Statistically steady carrier phase turbulence fluctuations have been established first before tracking the dispersed phases. Afterwards, the equations of motion of particles and bubbles are advanced simultaneously with the carrier phase equations for an additional N_t time steps [Table (3.1)], and collisions statistics are collected. The 3D energy and dissipation spectra for three Reynolds numbers $Re_\lambda = 57$, 77, and 96 are shown in Figures (3.5a-3.5c). In the three simulations presented here the maximum resolved wavenumbers are $k_{max}\eta = 1.55$, 1.31, and 1.94. The spectra show that dissipative scales are well resolved.

3.7 Particles and Bubbles Parameters

Fayed and Ragab [22] studied the collisions frequency of mono/bi-disperse particles in a frozen turbulent flow filed. They noticed a large uncertainty associated with this approach particularly for Stokes number near unity. For this reason, all simulations (I-IV) listed in table(3.2) have been obtained using "dynamic" turbulence velocity fields approach. In this approach the equations of motions of the dispersed phases are integrated simultaneously with

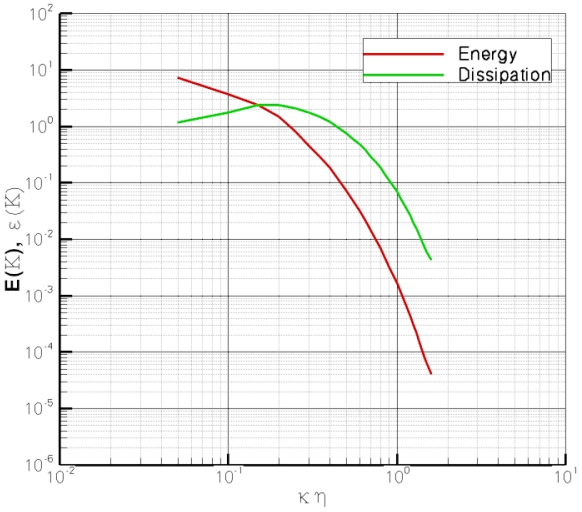

(a) $Re_\lambda = 57$, $N = 64$

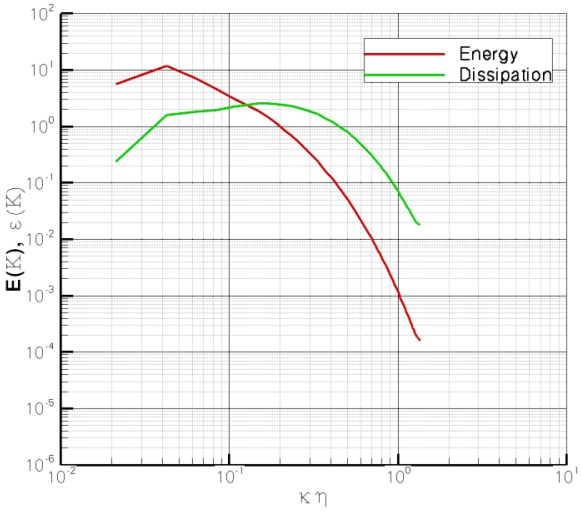

(b) $Re_\lambda = 77$, $N = 128$

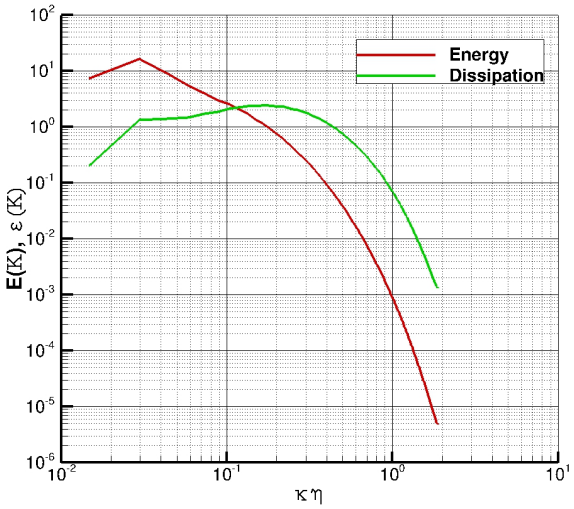

(c) $Re_\lambda = 96$, $N = 256$

Figure 3.5: DNS 3D energy and dissipation spectra

Table 3.1: Isotropic Turbulence Simulation Parameters

simulation	A	B	C
grid size N	64	128	256
kinematic viscosity ν_f	0.06575	0.04	0.026315
OU process σ'	2.4693	30.0	30.0
OU process τ'	0.164	0.00111	0.00111
forced wavenumbers K_f	$\sqrt{2}$	$2\sqrt{2}$	$2\sqrt{2}$
time step Δt	0.001	0.0005	0.0002
turbulence Reynolds number Re_λ	57	77.2	96.3
Kolmogorov length scale η	0.0486	0.02044	0.01519
dissipation rate ϵ	52.7	371.4	344.6
velocity fluctuation (rms) u'	5.2	8.74	8.64
Taylor microscale λ	0.72	0.3534	0.2933
integral length scale L_f	1.6	1.0	0.968
resolved wavenumbers $k_{max}\eta$	1.55	1.31	1.94
number of time steps for collision statistics N_t	6000	6000	4000

the equations of the carrier phase using the same time step and time advancement scheme.

Table 3.2 summarizes the different particle parameters used. All simulations (I) to (IV) were conducted in an evolving turbulent flow field. For each simulation, particle and bubble diameters are fixed and the particle Stokes number is varied by changing the particle response time, which allows us to study the effects of Stokes number on radial distribution function, radial relative velocity and collisions kernel. The effect of bubble size is studied through the comparison of simulation (II) and (III).

Table 3.2: Particles Parameters

Simulation	I	II	III	IV
Turbulence Reynolds number Re_λ	57	77	77	96
Number of particles (P_1) N_p	64^3	64^3	64^3	64^3
Number of bubbles (or particles P_2) N_b	32^3	32^3	32^3	32^3
Particle diameter d_p/η	0.61	0.61	0.61	0.829
Bubble diameter d_b/η	3.05	1.22	3.05	2.488

Direct numerical simulation of isotropic turbulent flow enables direct calculations of collisions frequency and proved to be very useful for validation of theoretical models. Sundaram and Collins [64] demonstrated that collisions frequency of mono-dispersed inertial particles suspended in dynamic isotropic turbulent flow is a function of particle Stokes number and

bounded from below by Saffman Turner [53] model and from above by Abrahamson model [1]. These results have been confirmed by Zhou et al. [82]. Wang et al. [70] studied the collisions frequency of mono-dispersed particles in a frozen isotropic turbulent flow. All of the simulations conducted by Wang et al. [70] and Zhou et al. [83] allow overlap of particles during collisions. Whereas, Sundaram and Collins [64] considered hard sphere perfectly elastic collisions. In these previous studies Stokes drag is the only force considered in the particles equations of motion. In this work we are interested in studying the effects of pressure gradient on the collisions of mono-disperse and bi-disperse and then, the case of bi-disperse will be extended to study particles and bubbles collisions.

3.8 Effects of Pressure Gradient

Dispersed phases are tracked by solving equations of motion of each phase as given by Eq 3.19. First term in the right hand side of Eq 3.19 is Stokes drag, and second term is a combination of the added mass and pressure gradient forces acting on each phase. In this section statistical collisions parameters of mono-disperse and bi-disperse phases at $Re_\lambda = 96$ without pressure gradient term in the RHS of Eq 3.19 are studied.

Mono-disperse phase *particles1-particles1* refers to the collisions within the same group of particles. Different Stokes number of the mono-disperse phase is obtained by varying particles densities while as their sizes remain constant. Bi-disperse *particles1-particles2* term means that collisions take place among particles in one group of fixed size and varying density and the other group which has fixed size and density. In these simulations, first group *particles1* Stokes number is varying $0.23 \leq St_p \leq 16.18$ and their diameters d_{p1} equal 0.829η for all Stokes number. The second group *particles2* has Stokes number of 0.174 and their diameters d_{p2} equal 2.488η. Radial relative velocity $\langle|w_r(d)|\rangle$ at contact, for mono-disperse is compared with and without pressure gradient in Eq 3.19 as shown in Figure 3.6a. There is no significant effects of pressure gradient on the radial relative velocity $\langle|w_r(d)|\rangle$ for mono-disperse because of their small sizes. Excellent agreement between radial relative velocity $\langle|w_r(d)|\rangle$ from DNS with no pressure gradient and Zaichik et al. [78] model while as Zaichik et al. [79] over predicts radial relative velocity at contact for mono-disperse. Radial relative velocity $\langle|w_r(d)|\rangle$ for bi-disperse phases is shown in Figure 3.6b. This figure shows excellent agreement between radial relative velocity $\langle|w_r(d)|\rangle$ from DNS with no pressure gradient and Zaichik et al. [78] model and Zaichik et al. [79] for bi-disperse except for some small difference at very small Stokes number between DNS and Zaichik et al. [79].

To illustrate the accumulation of the mono-disperse and bi-disperse phases in high strain regions, snapshots of *particles1* and *particles2* are picked for $Re_\lambda = 96$. The *particles1* Stokes number is $St_{p1} = 0.924$ and *particles2* Stokes number is $St_{p2} = 0.174$. Particles1 and particles2 positions whose centers fall in a thin slice of thickness $2d_{p2}$ that is parallel to the $xy-$plane of the computational box are projected onto the mid-plane of that slice. The projected centers and enstrophy contours are shown Figures 3.7a and 3.7b, where the

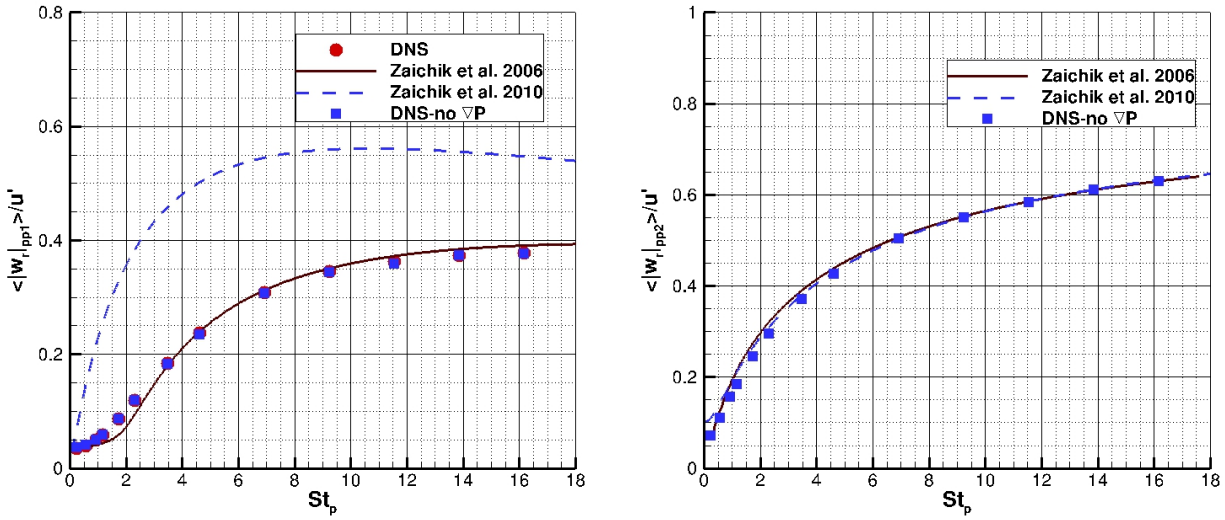

(a) Particle-particle radial relative velocity $\langle|w_r(d)|\rangle$ (b) Particle-bubble radial relative velocity $\langle|w_r(d)|\rangle$

Figure 3.6: Effects of Pressure gradient and added mass forces on radial relative velocity $\langle|w_r(d)|\rangle$ at $Re_\lambda = 96$, $N = 256$

particles are shown by small white circles. The red isles are regions of high vorticity while the blue isles are regions of high strain rate. Particles1 and particles2 are preferentially concentrated (accumulated) in high strain region as observed by Maxey [39], Wang et al. [68] and Zhou at al. [83].

Radial distribution function (RDF) is another important factor that contribute to the collisions kernel. Effects of pressure gradient on RDF of the mono-disperse is nearly negligible for $St_{p1} > 2.0$ as shown in Figure 3.8. Effects of pressure gradients on RDF for mono-disperse increases as Stokes number decrease, 7% at $St_{p1} = 0.924$, 13% at $St_{p1} = 0.577$ and 25% at $St_{p1} = 0.23$ higher than DNS with pressure gradient. Pressure gradient tends to move particles to the vortex core while as their inertia tends to move particles outside the vortex. Pressure gradient term reduces the migration rate of small inertia particles to the high strain regions. RDF of mono-disperse agrees qualitatively with Zaichik et al. [78]. For the bi-disperse, RDF is near to one over a wide range of particles1 Stokes number. It should be noted that if the two particles groups have the same Stokes number, RDF of the mono-disperse and bi-disperse will be equal. At small Stokes number $St_{p1} < 2.0$, RDF of the bi-disperse is slightly increasing and approach that of the mono-disperse phase at the smallest Stokes number $St_{p1} = 0.23$. At $St_{p1} > 2.0$ RDF of the bi-disperse nearly equal one (about 0.95). At large Stokes number, Particles1 motion is not fully correlated with the motion of the carrier phase that result in random distribution of particles1 while as particles2 undergo preferential concentration. Zaichik et al. [78] model produces RDF of nearly one at all Stokes number for the bi-disperse.

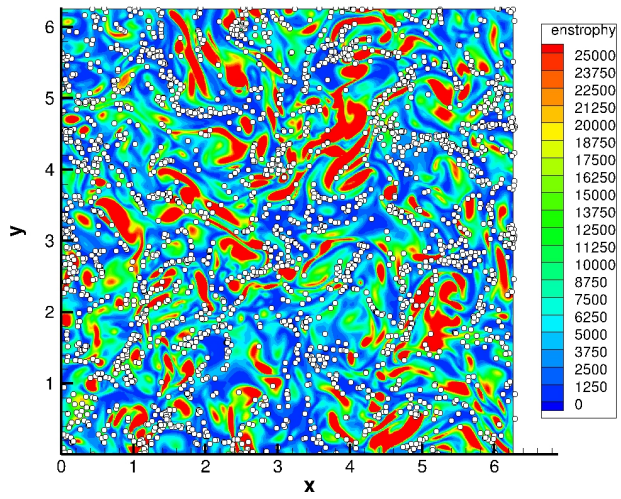

(a) Particles1 accumulation in high strain regions

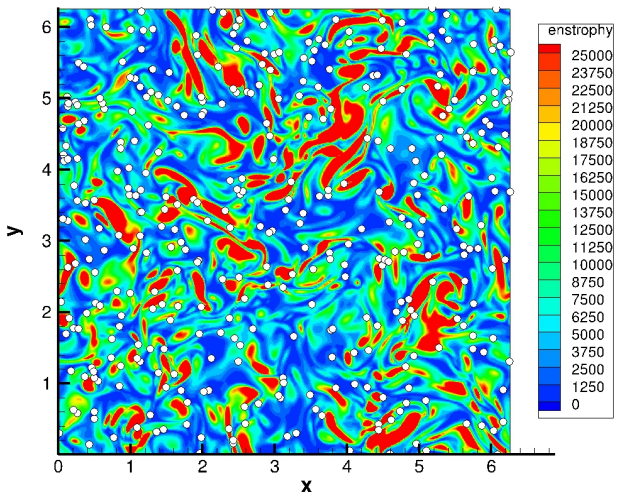

(b) Particles2 accumulation in high strain regions

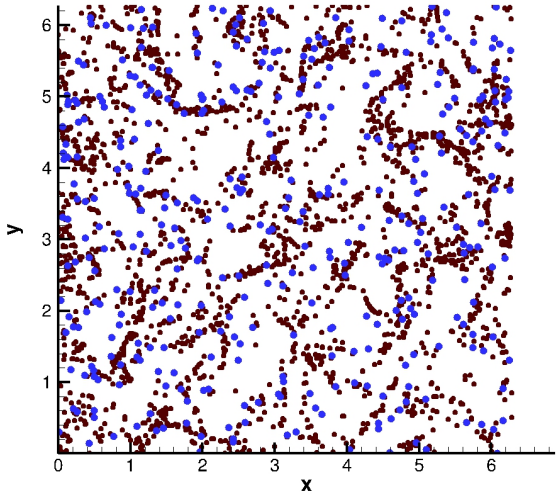

(c) Particles1-Particles1 preferential concentration

Figure 3.7: A snapshot of particles1-Particles2, $St_p = 0.924$, $Re_\lambda = 96$, $N = 256$ without pressure gradient

Collisions kernel is the product of radial relative velocity $\langle |w_r(d)| \rangle$ and radial distribution function as given by Eqs 3.28 and 3.29. Effects of pressure gradient and added mass forces on the collisions kernel is shown in Figures 3.9a and 3.9b. Negligible effects on the mono-disperse collisions kernel is observed for $St_{p1} > 2.0$ and small differences are observed for $St_{p1} < 2.0$ due differences in RDF. Collisions kernel of the bi-disperse has very good agreement between DNS without pressure gradient and Zaichik et al. [78] for $St_{p1} < 2.0$ as shown in Figure 3.9b. Small differences are observed for $St_{p1} > 2.0$ due to differences in RDF.

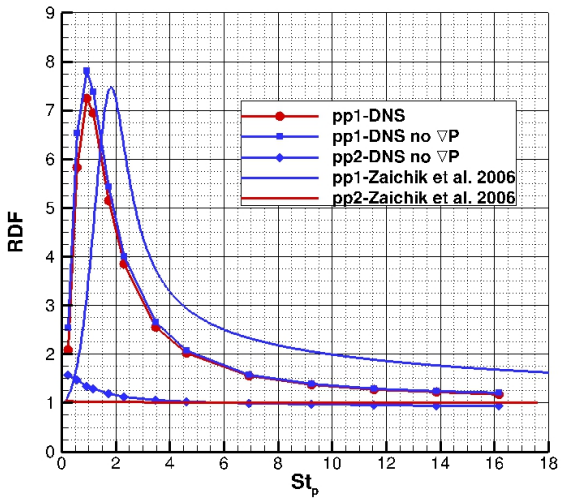

Figure 3.8: Effects of Pressure gradient and added mass forces on radial distribution function RDF

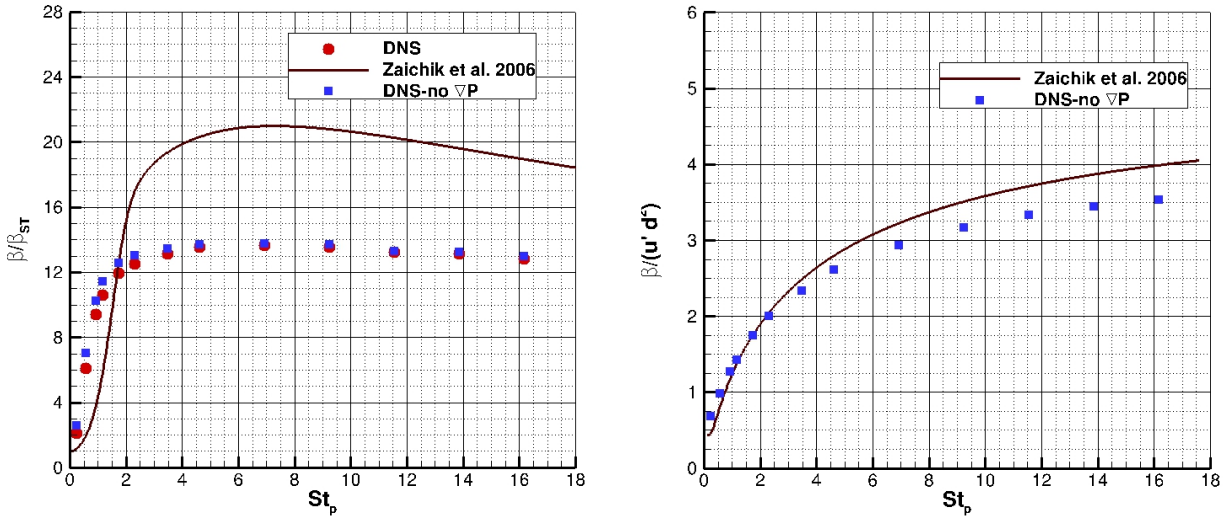

(a) Particle-particle collisions kernel

(b) Particle-bubble collisions kernel

Figure 3.9: Effects of Pressure gradient and added mass forces on collisions kernel at $Re_\lambda = 96$, $N = 256$

3.9 Particles and Bubbles Segregation

In this section, inertial particles and inertialess particles (bubbles) collisions are studied. Collisions takes place between particles of fixed size and varying density and bubbles which has fixed size and zero inertia. It is well known that preferential concentration of inertial particles occurs for Stokes numbers near unity (Maxey [39], Wang et al. [68], Zhou at al. [83]). Due to centrifugal accelerations, particles accumulate in high-strain regions between vortex cores. On the contrary, gas bubbles in liquid tend to migrate into vortex cores. Hence particles-bubbles segregation is possible, and it can result in radial distribution functions being less than one. As an example, heavy particles and gas bubbles suspended in the field of a steady column vortex will be completely segregated, where particles will be expelled from the vortex core while bubbles will accumulate in the vortex core. In this ideal situation, the radial distribution function at collision for particle-bubble collisions will be nearly zero. Thus, particles-bubbles segregation has an important effect on the particle-bubble collisions rate.particles-bubbles segregation is possible as observed by Julyan et al. [65] in chaotic flows, and it can result in radial distribution functions being less than one.

To demonstrate this phenomenon, we consider collisions of solid particles (mono-disperse) and solid particles with gaseous bubbles (bi-disperse) at turbulence Reynolds numbers $Re_\lambda = 57$, $Re_\lambda = 77$ and $Re_\lambda = 96$, as presented in Table (3.1) and Table(3.2). To illustrate the accumulation of the mono-disperse and bi-disperse phases, snapshots of particles and bubbles

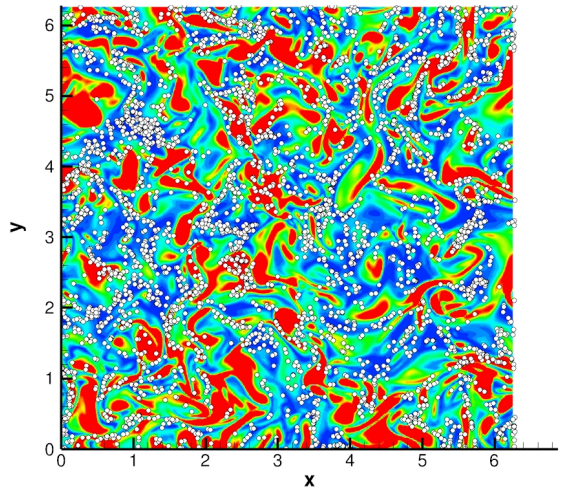

(a) Particles accumulation in high strain regions

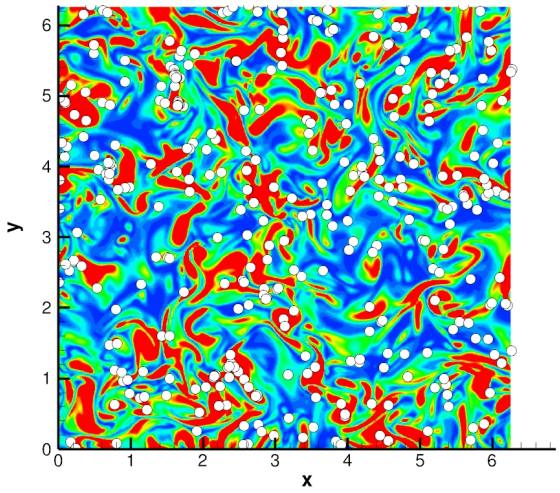

(b) Bubbles accumulation near high vorticity regions

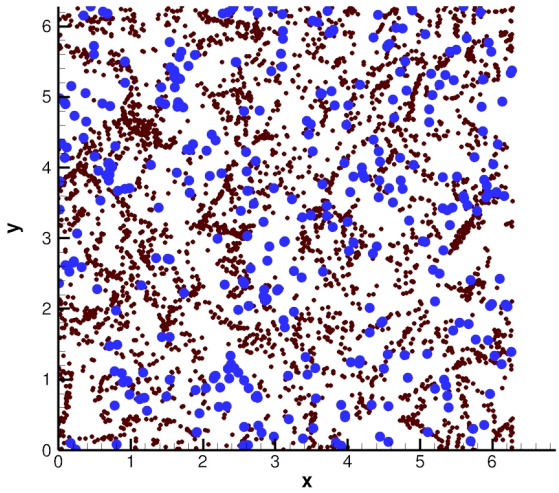

(c) Particles-bubbles segregation

Figure 3.10: A snapshot of particles-bubbles segregation, $St_p = 0.924$, $Re_\lambda = 96$, $N = 256$

are picked for $Re_\lambda = 96$. The particle Stokes number is $St_p = 0.924$. Particles positions whose centers fall in a thin slice of thickness $2d_b$ that is parallel to the $xy-$plane of the computational box are projected onto the mid-plane of that slice. The projected centers and enstrophy contours are shown Figure (3.10a), where the particles are shown by small white circles. The red isles are regions of high vorticity while the blue isles are regions of high strain rate. The figure demonstrates the well known preferential concentration (accumulation) of solid particles at Stokes number near unity. Particles accumulate in the isles of high strain rate between vortex cores. Bubbles positions whose centers also fall in the same slice are projected on the same plane at the same instant of time and are shown in Figure (3.10b). We recall that the bubble diameter in this simulation is $d_b = 2.488\eta$. The bubbles tend to concentrate in regions of high vorticity in and around vortex cores. The relative positions of particles and bubbles in the slice are shown in Figure (3.10c), they are partially segregated. The segregation is enhanced by the pressure gradient term that forces the bubbles toward the low pressure regions.

3.10 Theoretical Models Assessment for particle-bubble collisions

Theoretical collisions model usually predict the two main statistical collisions parameters , radial distribution function (RDF) and radial relative velocity, under certain turbulent conditions (i.e. r.m.s of turbulent velocity fluctuations and turbulent dissipation rate). By knowing these two quantities, theoretical models should provide us with the RDF and radial relative velocity. In order to fairly validate and assess the performance of these theoretical models, RDF and radial relative velocity are compared independently with that calculated from DNS. The overall performance of each model is assessed by comparing collisions kernel with the collisions kernel from direct calculations in DNS. DNS collisions results are obtained by fixing the bubble and particle diameters as given in Table (3.2), and varying the particle density.

3.10.1 Radial Distribution Functions

Comparisons between DNS and theoretical models are presented at different Reynolds number. The particle Stokes number, St_p, is then computed from Eq(2.11). The same procedure is applied when computing collision kernel, RDF and radial relative velocity using the theoretical models by Zaichik et al. [78], and [79]. *Strictly speaking, application of Zaichik et al. [78] model model should be limited to heavy small particles. Its application to the case of particle-bubble collisions may be questionable, but it is presented here only for reference.* Radial distribution functions for mono-disperse (particles-particles), g_{pp}, and bi-disperse (particles-bubbles), g_{pb}, are shown in Figures 3.11a-3.11c and 3.12a-3.12d. For

mono-disperse collisions, the radial distribution function, g_{pp}, is always greater than one, and as a result of preferential concentration it has a narrow peak near Stokes number of one. It approaches one for very small and very high Stokes numbers. Zaichik et al. [78] model predicts RDF for mono-and bi-disperse phases while Zaichik et al. [79] assumes one for RDF. Comparison between RDF calculated from DNS and that predicted by Zaichik et al.'s [78] model qualitatively agree for the mono-disperse phase. This model predicts variation of RDF with particle Stokes number for different Re_λ similar to that by DNS, however, the peak of the RDF is around $St_p = 1.8$ instead of one. Simulation (II) is not shown because the results are identical to simulation (III) for the mono-disperse case.

Zaichik et al. [78] model has been applied to predict the RDF for the case of bi-disperse particle-bubble collisions. Figures 3.12a-3.12d show the comparison between the RDF by DNS and this model. Pressure gradient and added mass forces enhance the segregation of inertial particles and bubbles. This implies that the RDF is less than unity as evident from these figures. Added mass and pressure gradient terms in the equations of motion of particles are included in DNS. However, Zaichik et al. [78] model predicts RDF for this case of particle-bubble to be approximately equal to one. This behavior of the model is due to neglecting the effects of pressure gradient and added mass forces in the model. These terms are more significant for large bubbles. In simulation (II) the bubble diameter is 1.22η whereas for simulation (III) it is 3.05η. As evident in Figure 3.12b-3.12c the model, in which those effects are neglected, shows better agreement with DNS for the smaller bubble diameter. Zaichik et al. [79] take into consideration the effects of these two forces in finding the radial relative velocity, however, it does not provide a model for the RDF; which is assumed to be one. Hence, theoretical kernels for particles-bubbles collisions that assume unity for the radial distribution function stand to overestimate the collisions kernel.

3.10.2 Radial Relative Velocity

As shown by Eqs(2.12) and (2.13), the non-dimensional collision kernel $\beta/2\pi u' d^2$ and mean radial relative velocity $\langle |w_r(d)| \rangle / u'$ are equal only if the radial distribution function $g_{ij}(d)$ is unity. For models that assume the radial distribution function to be one, the assessment should be based on comparisons of the mean radial relative velocity $\langle |w_r(d)| \rangle / u'$ rather than the collision kernel $\beta/2\pi u' d^2$. Zaichik et al. [78] model has a restriction on the particle size to be on the order of the smallest turbulent length scale while Zaichik et al. [79] model is developed to be applicable for an arbitrary particle size. Figures (3.13a-3.13c) depict the comparison between $\langle |w_r(d)| \rangle$ calculated from DNS and that predicted from the two models, Zaichik et al. [78] and [79] for mono-disperse collisions. Radial relative velocity $\langle |w_r(d)| \rangle$ from DNS and Zaichik et al. [78] model asymptotically approach the value of $\langle |w_r(d)| \rangle$ calculated from Saffman-Turner [53] model at very small particles Stokes number. Both radial relative velocity $\langle |w_r(d)| \rangle$ from DNS calculations and Zaichik et al. [78] have very good agreement over a wide range of particle Stokes number. However, Zaichik et al. [79]

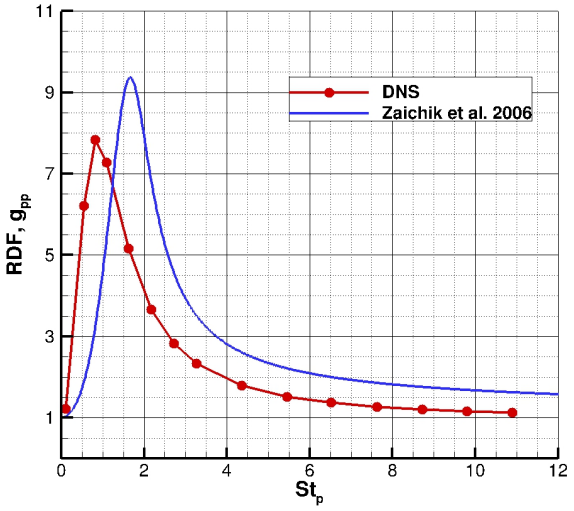

(a) $Re_\lambda = 57$, $N = 64$

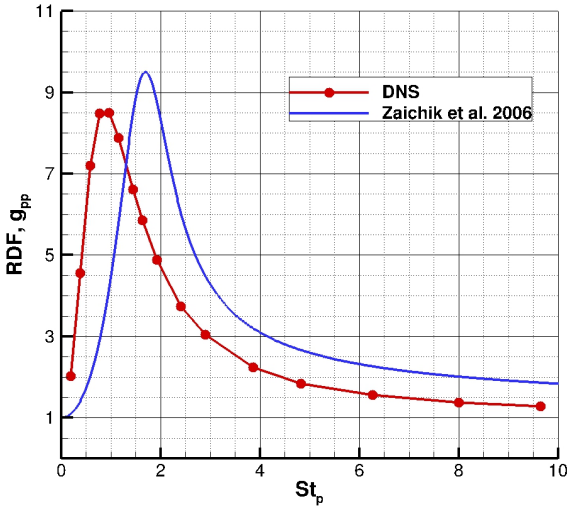

(b) $Re_\lambda = 77$, $N = 128$, simulation (III)

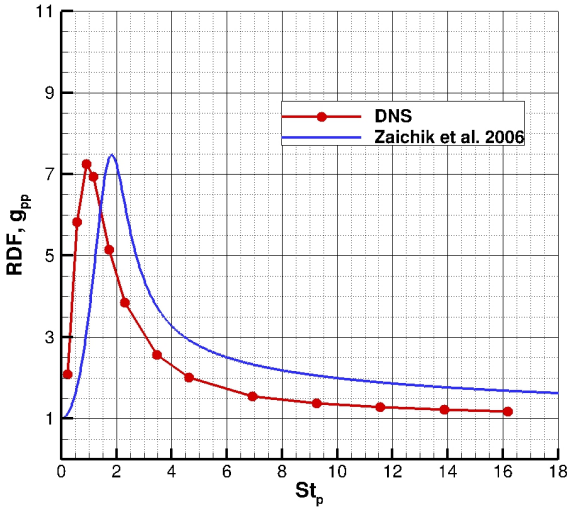

(c) $Re_\lambda = 96$, $N = 256$

Figure 3.11: RDF comparison of DNS and Zaichik et al. [78] model for mono-disperse particle-particle collisions

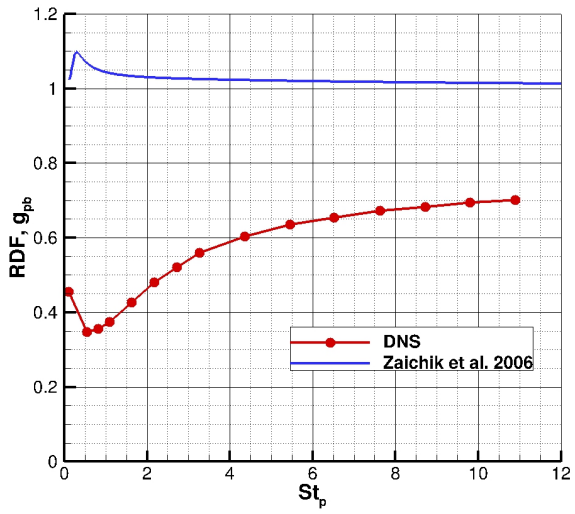

(a) $Re_\lambda = 57$, $N = 64$

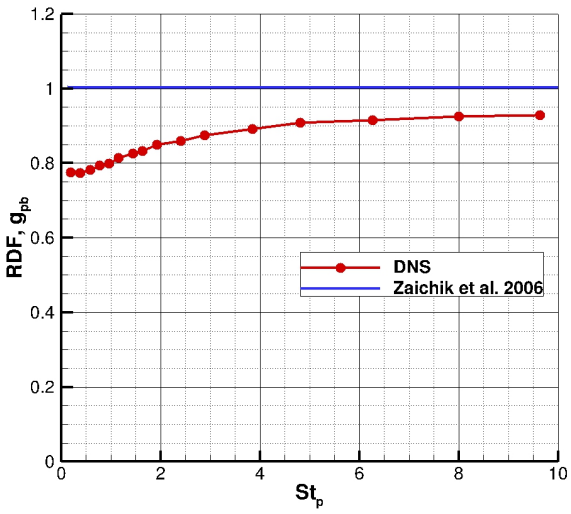

(b) $Re_\lambda = 77$, $N = 128$, simulation (II)

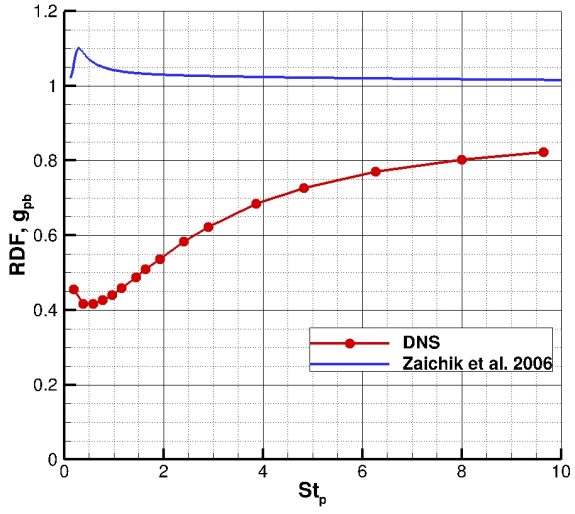

(c) $Re_\lambda = 77$, $N = 128$, simulation (III)

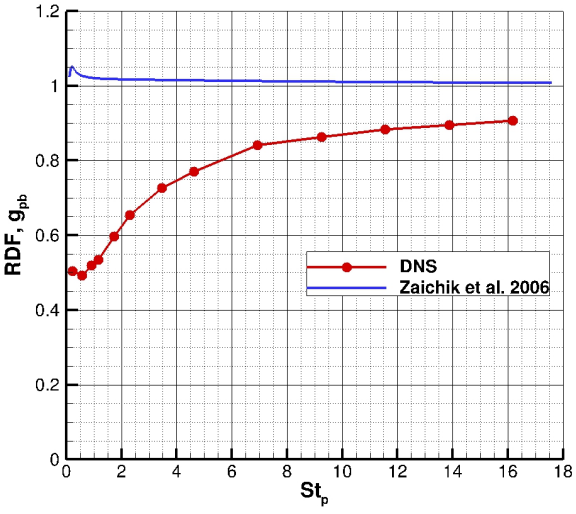

(d) $Re_\lambda = 96$, $N = 256$

Figure 3.12: RDF comparison of DNS and Zaichik et al. [78] model for bi-disperse particle-bubble collisions

model overpredicts the radial relative velocity $\langle|w_r(d)|\rangle$ of mono-disperse (particle-particle) collisions.

The radial relative velocity of the bi-dispersed phase (particle-bubble) for different Reynolds numbers are compared and shown in Figures (3.14a-3.14d). These figures show good agreement between radial relative velocity $\langle|w_r(d)|\rangle$ calculated by DNS and both models developed by Zaichik et al. [78] and [79]. Again, the comparison is remarkably good for simulation (II) with smaller bubble diameter. Overall, Zaichik et al. [79] is in better agreement with DNS for small Stokes number since it has a better representation of the effects of the particle size.

3.10.3 Collisions Kernel

Since Zaichik et al. [78] model predicts both RDF and $\langle|w_r(d)|\rangle$, comparisons between DNS and this model for collisions kernel normalized by Saffman-Turner [53] are shown in Figure 3.15a-3.15c for mono-disperse particle-particle collisions. Collisions kernel calculated from DNS and this model approach collisions kernel calculated from Saffman-Turner [53] in the limit of very small Stokes number. The agreement between collisions kernel calculated from DNS and this theoretical model is qualitatively good. Despite the very good agreement for radial relative velocity $\langle|w_r(d)|\rangle$ between DNS and this model; the shift of the maximum value in the RDF is responsible for these differences between collisions kernel calculated from DNS and this theoretical model. For the case of bi-disperse (particle-bubble) the segregation behavior has a significant effect on the comparison between DNS calculations and Zaichik et al. [78] model prediction as shown in Figure (3.16a-3.16d). It is shown in these figures that Zaichik et al. [78] model over predicts the collisions kernel because it does not consider particle-bubble segregation or over predict RDF although it has a very good agreement with DNS for radial relative velocity $\langle|w_r(d)|\rangle$.

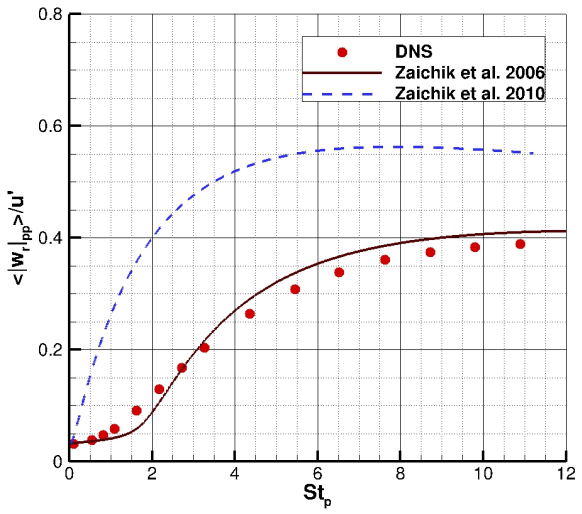

(a) $Re_\lambda = 57$, $N = 64$

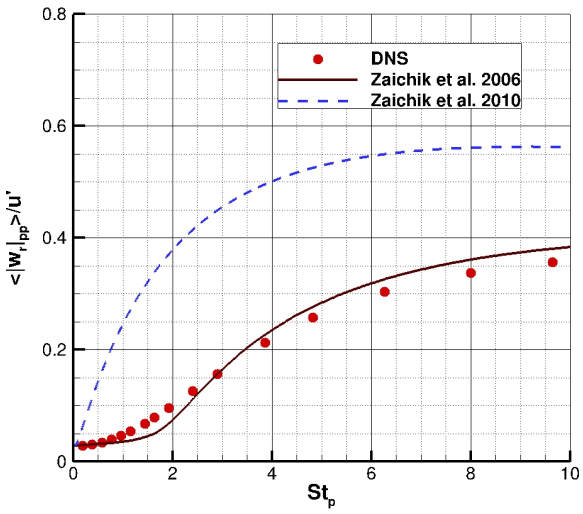

(b) $Re_\lambda = 77$, $N = 128$, simulation (III)

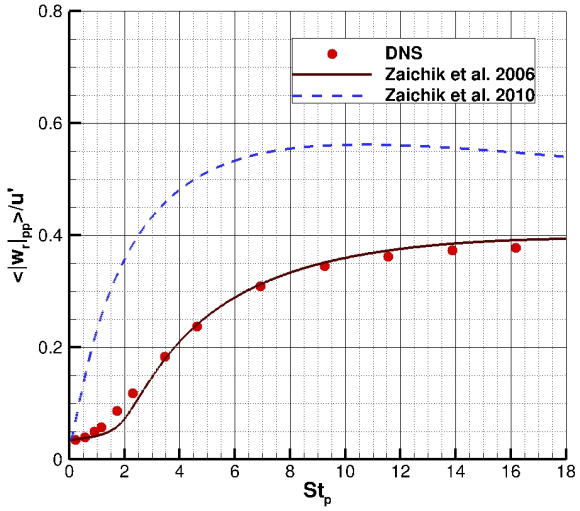

(c) $Re_\lambda = 96$, $N = 256$

Figure 3.13: $\langle |w_r(d)| \rangle$ comparison of DNS, Zaichik et al. [78] and Zaichik et al. [79] models for mono-disperse particle-particle collisions

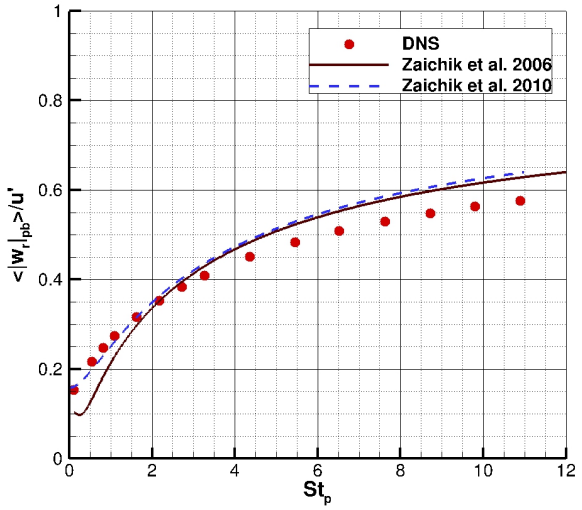

(a) $Re_\lambda = 57$, $N = 64$

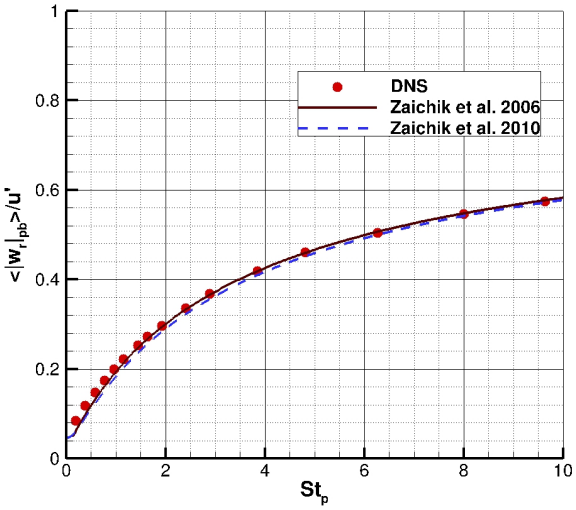

(b) $Re_\lambda = 77$, $N = 128$, simulation (II)

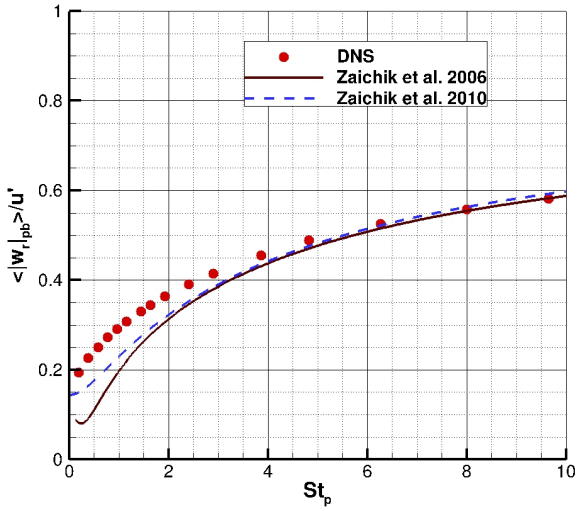

(c) $Re_\lambda = 77$, $N = 128$, simulation (III)

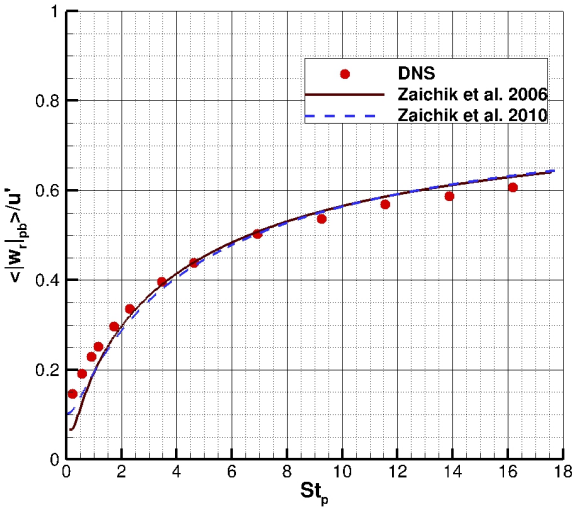

(d) $Re_\lambda = 96$, $N = 256$

Figure 3.14: $\langle |w_r(d)| \rangle$ comparison of DNS, Zaichik et al. [78] and Zaichik et al. [79] models for bi-disperse particle-bubble collisions

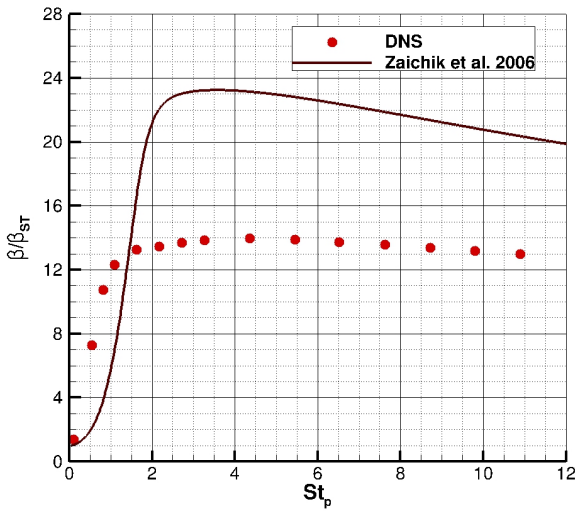

(a) $Re_\lambda = 57$, $N = 64$

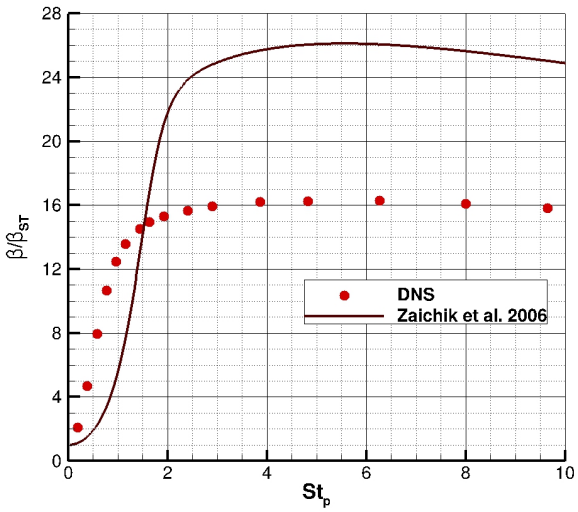

(b) $Re_\lambda = 77$, $N = 128$, simulation (III)

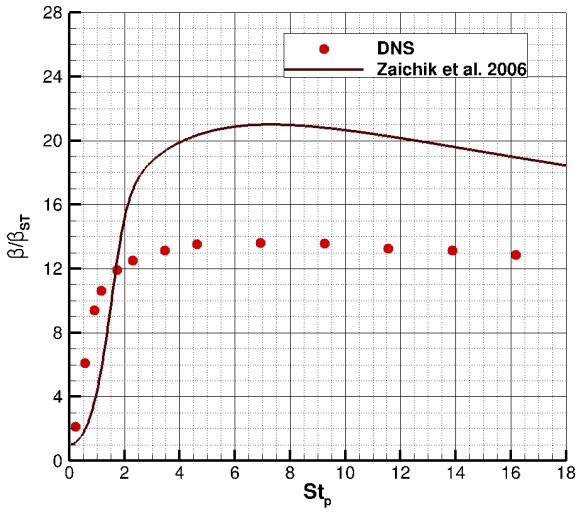

(c) $Re_\lambda = 96$, $N = 256$

Figure 3.15: Collisions kernel comparison of DNS and Zaichik et al. [78] model for monodisperse particle-particle collisions

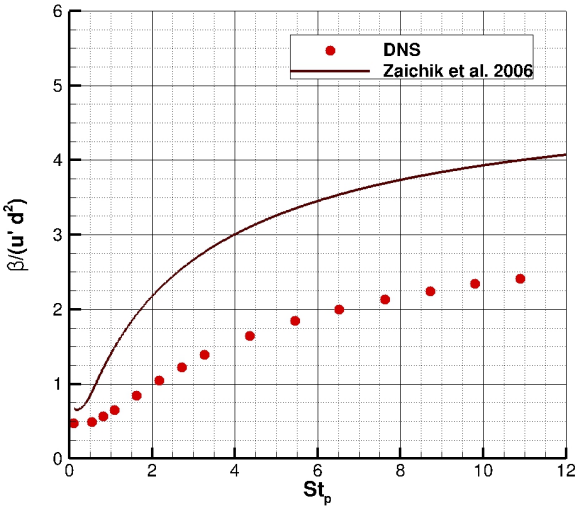

(a) $Re_\lambda = 57$, $N = 64$

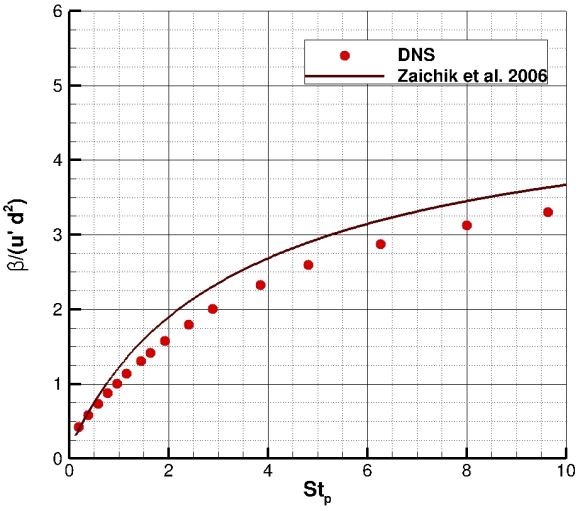

(b) $Re_\lambda = 77$, $N = 128$, simulation (II)

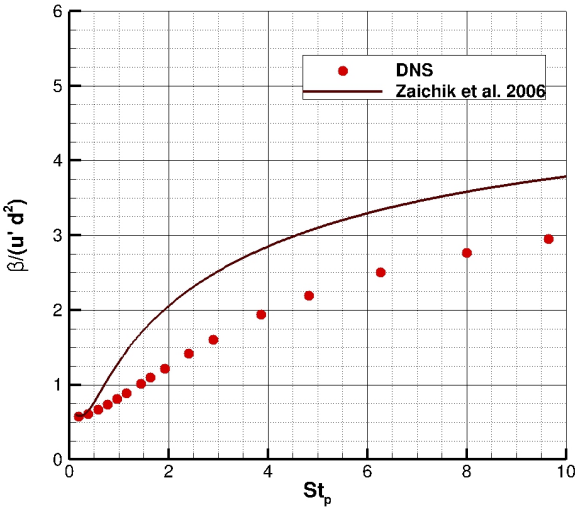

(c) $Re_\lambda = 77$, $N = 128$, simulation (III)

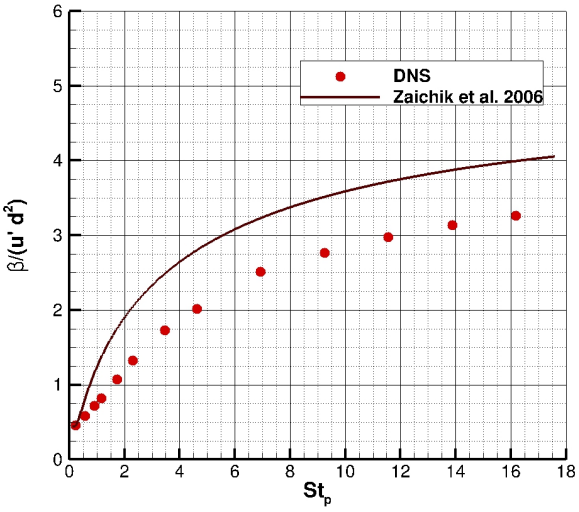

(d) $Re_\lambda = 96$, $N = 256$

Figure 3.16: Collisions kernel comparison of DNS and Zaichik et al. [78] model for bi-disperse particle-bubble collisions

Chapter 4

Large-Eddy Simulations of Collisions Frequency

4.1 Introduction

In DNS approach, Navier-Stokes equations are solved numerically without any use of turbulence models. The grid is fine enough to resolve all scales of turbulence from the large energetic scales down to the dissipative scales. However, this kind of numerical treatment is too expensive in terms of CPU time and computer memory usage even if parallel computations are applied. Grid size N required to conduct DNS depends on the turbulence Reynolds number. An estimate is given by

$$N^3 = O(Re_\lambda^{\frac{9}{2}}) \tag{4.1}$$

where Re_λ is Reynolds number based on Taylor microscale (λ) and turbulent intensity u'. This implies that for many practical applications at high Re_λ, DNS is an unfeasible approach. An alternative approach is Large-Eddy Simulations (LES) in which a coarser grid is used to resolve the large scales up to a cutoff wavenumber that is usually in the inertial sub-range of the energy spectrum. A turbulence model is then used to represent the effects of the subgrid stresses on the dynamics of large scales and to drain off kinetic energy from those scales. Two main categories of subgrid turbulence models have been developed in the literature: Structural models and functional models. In structural models, the subgrid stress term is calculated directly from an estimated subgrid velocity field. Functional models estimate the subgrid stress term based on an *ad hoc* viscosity coefficient. In this chapter LES of particles and bubbles collisions are studied and compared with that of DNS at the equal turbulence Reynolds number.

For the purpose of tracking small particles with diameters on the order of Kolmogorov

length scale, the full instantaneous unfiltered velocity field of the carrier phase is needed. This means that the velocity field $\vec{u}(\vec{x},t)$ is needed on a fine grid appropriate for resolving all turbulent scales of the Re_λ under consideration, and we will call such a fine grid the DNS grid. The large scales component of the velocity field is resolved using LES on a coarser grid. New method for the synthesis of the subgrid velocity fluctuations on the DNS grid is presented. A multifractal representation of the energy cascade is used to synthesize subgrid vorticity field. Then a Poisson's solver is used to find a vector potential whose curl gives the subgrid velocity field. The subgrid velocity field from a multifractal approach is added to the resolved field using LES to construct the total velocity field pn the DNS grid. For the sake of demonstration of the importance of the subgrid fluctuations on particle tracking, another approach is tested in which the subgrid filed is determined by filtering the large scales of DNS field at one instant of time. The subgrid fluctuations thus obtained are frozen in time while the large scales are determined from dynamically evolving large-eddy simulation. In other words, the large scales evolve in time while the subgrid filed is fixed.

4.1.1 Subgrid Models

The first eddy viscosity model has been developed by Smagorinsky [61]. This model is proposed based on dimensional reasoning, however it is an *ad-hoc* approach. Germano et al. [42] developed a dynamic model by which Smagorinsky "constant" is calculated as the simulation progress in time, and hence becomes function of space and time. The dynamic model overcomes many of shortcomings of Smagorinsky [61] model. Kraichnan [31] proposed a spectral eddy viscosity model in accordance with Kolmogorov's 2/3 law. In this model, spectral eddy viscosity is calculated globally in the same sense like Smagorinsky's [61] model. Metais and Lesieur [41] modified Kraichnan's [31] model to find this artificial viscosity locally in the spectral domain. All of these eddy viscosity-based subgrid models depend on a non-physical *ad-hoc* viscosity to close the filtered momentum equation. These models have good performance in many types of simulations but none of them provides an estimation of the subgrid velocity fluctuations.

Structural subgrid models is another approach to calculate the subgrid stress terms. Bardina et al. [18] developed a structural model to calculate the subgrid stresses directly from the resolved flow velocities. Their model considers small scales in the resolved field to be large eddies for the unresolved flow field. The subgrid stresses are estimated by applying a second test filter. The average subgrid velocities are considered to be the difference between the resolved velocities and second filtered velocities. However, Bardina's [18] model failed to drain sufficient turbulent kinetic energy from large scales to small scales, and an *ad-hoc* viscosity is included to stabilize the simulation.

Domaradzki and Saiki [55] estimated the subgrid velocity by expanding the resolved large scales velocity field to the subgrid velocity scales two times smaller than the grid scales in the spectral domain. The first step is a deconvolution by an approximate inversion of the

filtering operation. The non-linear step is applied to generate a range of subgrid scales on a grid two times smaller than the coarse LES grid. In the second step phases of the newly generated subgrid wavenumbers are adjusted in order to correspond to the small resolved scales generated by the nonlinear interactions of large scale.

Another approach to model the subgrid scales structurally is to invert the resolved velocities by using top-hat filter inversion an in Stolz's model [62]. This method of getting the unfiltered quantities originates from a mathematical basis and has no clear physical basis. The model relies explicitly on a multi-top hat filters in the truncated series that approximates the inversion of the top hat filters. This means that modes of high wavenumbers do not exist in the obtained subgrid velocities in Stolz's model [62] although it is a stable model.

Scotti and Meneveau [40] developed new mathematical tool (fractal interpolation) to synthesis the subgrid velocity field. Fractal interpolation, is a combination of standard interpolation schemes and some stochastic parameters. It can interpolate the resolved velocity field down to any level of resolution. The resulting subgrid velocity is used to calculate subgrid stresses in a direct way. However, there is no proof that resolved velocity or the synthetic field has a fractal structure. Burton [6] showed that the gradient quantities such as enstrophy and turbulent dissipation rate of a 3D ($N = 512^3$) homogeneous isotropic turbulence exhibit a multifractal behavior. Probability density function of multifractal multipliers has been constructed for different scales. PDF of the multifractal multipliers show a scale invariant.

Enstrophy and dissipation of homogeneous isotropic turbulence show a multifractal because of the nonlinear mechanisms of turbulence [6]. These velocity gradient-based quantities undergo continuous stretching, and folding that produce multifractal behavior. Burton and Dahm [7] estimated the subgrid enstrophy of the small scales using Kolmogorov's 2/3 law. A spectrally sharp cut-off test filter has been applied to determine the enstrophy of the inertial scales between the second and first filters. The enstrophy of the second filter is used to determine the subgrid enstrophy by integrating enstrophy spectrum from the test filter wavenumber to the maximum required wavenumber in the inertial sub-range. The subgrid vorticity magnitude is estimated from a 3D stochastic multiplicative cascade process down to the smallest scales. Multipliers that are used in the multiplicative cascade process are drawn from the PDF of the scale-invariant multipliers of a 3D given DNS data for isotropic homogeneous turbulence. The orientation of the vorticity field is estimated by neglecting the correlation between the multipliers and the angles in the orientation cascade. It has been taken to be the orientation of the second test filtered subgrid scales. Biot-Savart law is then applied to calculate the averaged subgrid velocity field from the subgrid vorticity field analytically on the LES grid nodes.

In the model derivation by Burton and Dahm [7], a spectral sharp cut off filter has been used to determine the magnitude of enstrophy between first and second test filter. Nevertheless, a top hat test filter is used to determine the velocity field between the first filter and the second test filter. The subgrid velocity fluctuations for high wavenumber are still unknown for grid points finer than the LES grid points.

Effects of subgrid scales on the collisions of dispersed phases in homogeneous isotropic turbulence have been investigated by Fede and Simonin [16] where drag is the only term considered in the particle equation of motion. They found that effects of SGS velocity fluctuations are negligible for large particles stokes number ($St_p > 5.0$) while SGS velocity fluctuations are essential for small particles Stokes ($St_p \leq 0.5$) [16]. Jin et al. [25] demonstrated the effects of SGS velocity fluctuations on the collisions of particles and reached the same conclusion as that by Fede and Simonin [16]; SGS velocity fluctuations are needed for particles of small Stokes number in the frame work of LES.

Some efforts have been expended in stochastically modeling the subgrid scales fluctuations. Fede et al. [17] derived Langiven to estimate the variance of the subgrid fluctuations along the particle path. The model enable reasonable predictions of the particles kinetic energy. Nevertheless, this model failed to predict particles concentration leading to more uniform distribution of the particles.

4.2 Governing Equations for LES

The flow field is a forced homogeneous isotropic incompressible turbulence in a periodic cube of side 2π. A pseudo-spectral method with sharp cutoff filter in the spectral domain is used. The cutoff wavenumber is $k_c = \pi/\Delta x$. Filtered Navier-Stokes equations are written as,

$$\frac{\partial \bar{u}_i}{\partial x_i} = 0 \tag{4.2}$$

$$\frac{\partial \bar{u}_i}{\partial t} + \frac{\partial \bar{u}_i \bar{u}_j}{\partial x_j} = -\frac{1}{\rho_f}\frac{\partial \bar{p}}{\partial x_i} + \nu_f \frac{\partial^2 \bar{u}_i}{\partial x_j \partial x_j} - \frac{\partial \tau_{ji}}{\partial x_j} + F_i \tag{4.3}$$

where $\bar{u}_i(x_i, t)$ is the instantaneous filtered velocity field, and $\bar{p}(x_i, t)$ is the filtered pressure field. The subgrid stress term τ_{ij} is given by

$$\tau_{ij} = \overline{u_i u_j} - \bar{u}_i \bar{u}_j \tag{4.4}$$

where u_i is the unfiltered velocity, and it is decomposed into resolved $\bar{u}_i$ and subgrid u'_i components.

Burton and Dahm [7] developed a subgrid model that estimates subgrid velocity field using Biot-Savart law. In this model, subgrid stress tensor τ_{ij} is calculated directly from the average estimated subgrid velocity components u'_i. Burton and Dahm [7] used a second top hat filter to find the velocity field u_i^{Δ} between the first and the second test filter although a spectral sharp cut-off filter was used in the model derivation.

$$u_i^{\Delta} \equiv \bar{u}_i - (\bar{u}_i)_{2\Delta} \tag{4.5}$$

The average subgrid velocity fluctuations evaluated at the LES grid points are written in a simplified form as the following

$$\langle u_i(\vec{x})\rangle = I(N_f)A(N_f)\sqrt{(}\kappa)u_i^{\Delta} \tag{4.6}$$

$$I(N_f) = C_I 2^{-(13/6)N_f}\left\langle (M_1 M_2 .....M_{N_f})^{1/2}\right\rangle^{-N_f} \tag{4.7}$$

where C_I is a universal constant and equal to 0.37, Burton and Dahm [7].

$$A(N_f) \equiv 2^{3N_f/2}[2^{4N_f/3}-1]^{1/2}\left\langle (M_1 M_2 .....M_{N_f})^{1/2}\right\rangle^{N_f} \tag{4.8}$$

and

$$\tau_{ij} = \mathbf{B}(\overline{\bar{u}_i u_j^{\Delta}} + \overline{u_i^{\Delta}\bar{u}_j}) + \mathbf{B}^2\overline{u_i^{\Delta}u_j^{\Delta}} \tag{4.9}$$

where

$$\mathbf{B} \equiv 0.47\ 2^{-2N_f/3}[2^{4N_f/3}-1]^{1/2} \tag{4.10}$$

Top hat filter in spectral domain can be written as follows

$$\widehat{\vec{\bar{u}}} = G(\vec{K}) \bullet \widehat{\vec{u}} \tag{4.11}$$

and

$$G(\vec{K}) = \frac{\sin(k_x\Delta/2)}{\Delta/2}\frac{\sin(k_y\Delta/2)}{\Delta/2}\frac{\sin(k_z\Delta/2)}{\Delta/2} \tag{4.12}$$

where Δ is the filter width. Spectrally sharp cut-off filter is applied by zeroing out all modes of wavenumber greater than a specific cut-off wavenumber

In this dissertation, top hat filter and spectral sharp cut-off filter has been used to find u_i^{Δ} in Eq 4.5 to verify the subgrid stress model developed by Burton and Dahm [7]. In our simulations, the model failed to drain-off enough turbulent kinetic energy of large resolved scales for either of the filters. Therefore, a functional subgrid spectral eddy viscosity model due to Chollet-Lesieur [9] is used (See also Sagaut [54] and Jin et al. [25]).

$$\nu_t(k|k_c) = \nu_t^{+}(k/k_c)\sqrt{\frac{E(k_c)}{k_c}} \tag{4.13}$$

$$\nu_t^{+}(k|k_c) = C_K^{-3/2}[0.441 + 15.2exp(-3.03k_c/k)] \tag{4.14}$$

The Kolmogorov constant is $C_K = 2.5$ as given by Jin et al. [25].

The pressure gradient term is eliminated by taking the divergence of the momentum equation and imposing the incompressibility condition and the fact that the forcing term is also divergence free.

$$\left[\frac{d}{dt} + (\nu_f + \nu_t)\left|\vec{K}\right|^2\right]\vec{\hat{u}}_{\vec{K}} = -\vec{\hat{C}}_{\vec{K}} + \vec{K}\frac{\vec{K}.\vec{\hat{C}}_{\vec{K}}}{\left|\vec{K}\right|^2} + \vec{\hat{F}}_{\vec{K}} \tag{4.15}$$

where

$$\vec{\hat{C}}_{\vec{K}} = \widehat{(\vec{u}.\nabla\vec{u})}_{\vec{K}} \tag{4.16}$$

is the convective nonlinear term of the resolved scales and is treated by a pseudo-spectral method and 3/2-rule for de-aliasing. Following Rogallo [51] we use an integrating factor $e^{(\nu_f+\nu_t)\left|\vec{k}\right|^2(t-t_n)}$ to integrate the viscous term in Eq(4.15) analytically.

$$\frac{d}{dt}\left[\vec{\hat{u}}e^{(\nu_f+\nu_t)\left|\vec{K}\right|^2(t-t_n)}\right] = e^{(\nu_f+\nu_t)\left|\vec{K}\right|^2(t-t_n)}\left[-\vec{\hat{C}}_{\vec{K}} + \vec{K}\frac{\vec{K}.\vec{\hat{C}}_{\vec{K}}}{\left|\vec{K}\right|^2} + \vec{\hat{F}}_{\vec{K}}\right] \tag{4.17}$$

After a transient period, the 3D energy spectrum $E(k)$ is averaged over time. In Eq(4.13), $E(k_c)$ is also updated at the beginning of each time step but is held constant during the Runge-Kutta sub-steps.

4.3 Synthesis of Instantaneous Subgrid Velocity Field

For particle tracking in turbulent flow, the full instantaneous velocity field of the carrier phase is needed. This means that the velocity field $u_i(x_i, t)$ is needed on a fine grid appropriate for resolving the turbulent field for Re_λ under consideration, and we call such a fine grid the DNS grid. The large scale fluctuations are resolved on a coarse grid. We propose to extend Burton and Dahm [7] multifractal approach to explicitly synthesis instantaneous subgrid velocity field u_i'. The subgrid vorticity field is synthesized and then the corresponding velocity field can be obtained by solving the vector Poisson's equation instead of the Biot-Savart law. The subgrid enstrophy in an LES cell is estimated from the resolved (LES) field computed at the center of that cell. A scale-invariant multiplicative cascade process is used to distribute the subgrid enstrophy to a finer grid within each LES cell. The orientation of the subgrid vorticity is determined by an additive cascade from the orientation of the vorticity of the small resolved scales. Small scales of the resolved field u_i^Δ are defined by Eq 4.5.

Small scales of the resolved LES scales u_i^Δ are found by applying explicit sharp cut-off filter. The curl of u_i^Δ field and the enstrophy Q_Δ are calculated at the center of each computational LES cell. The subgrid entropy of the cell is estimated as follows,

$$Q_{sgs} = \kappa Q_{\Delta} \left[\left(\frac{k_{\eta}}{k_{\Delta}} \right)^{\frac{4}{3}} - 1 \right] \tag{4.18}$$

and $\kappa = (1 - 2^{-4/3})^{-1}$. The ratio k_{η}/k_{Δ} is equal to the number of cascade steps N_f

$$N_f = \log_2(\frac{\Delta}{\eta}) = \log_2(\frac{k_{\eta}}{k_{\Delta}}) \tag{4.19}$$

$$\left| \vec{\omega'} \right| (\vec{x}, t) = \left[Q_{sgs} \; 2^{3N_f} \prod_{n=1}^{N_f} M_n(\vec{x}, t) \right]^{\frac{1}{2}} \tag{4.20}$$

where M_n is a multiplier $0 \leq M_n \leq 1.0$. These multipliers are obtained from a scale invariant multipliers distribution $P(M)$. Burton [6] obtained the PDF (P(M)) from a DNS of isotropic homogeneous turbulence. We propose an approximation given by

$$P(M) = \frac{\pi}{2} sin\pi M, \qquad 0 \leq M \leq 1 \tag{4.21}$$

The second process is an orientation cascade of the generated vorticity field. Burton and Dahm [7] showed a weak correlation between vorticity orientations at two successive scales if the values of the multiplier M is low (i.e close to zero). On the other side for large values of M (i.e close to unity), there is a very strong correlation between orientation of two successive scales. The orientation of scale $n+1$ is related to the orientation of scale n by the cone angle ϕ as shown in Fig. 4.1. Based on the DNS data presented by Burton and Dahm [7], we propose the following equation for the probability distribution of decorrelation angle between the orientation of two consecutive stages in the cascade,

$$P(cos(\phi)) = \frac{\alpha}{2sinh\alpha} e^{\alpha cos(\phi)} \tag{4.22}$$

where

$$\alpha = \alpha_o M^2 \tag{4.23}$$

and α_0 is a constant that can be found by comparison with the DNS results. We found it to be equal to 55 when comparing with the conditional probability distribution $P(cos(\phi); M)$ in Burton and Dahm's [7] paper.

The orientation of the vorticity at stage n is defined by the unit vector $\vec{e}_n$. To obtain $\vec{e}_{n+1}$, we first rotate the coordinate system so that the new $z-$axis coincides with $\vec{e}_n$. In the rotated system we have

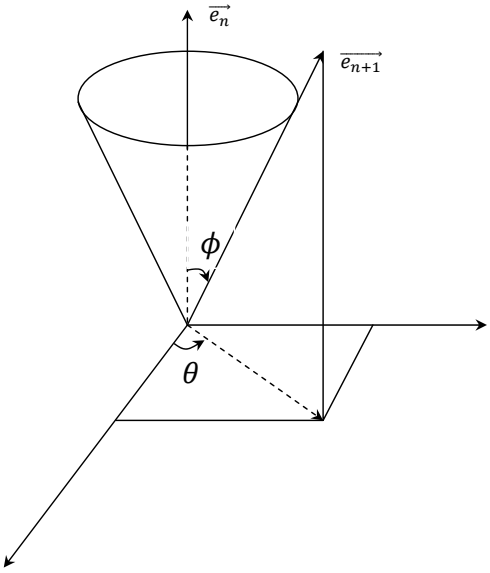

Figure 4.1: Schematic representation of two successive vorticity scale orientations

$$\vec{e}_{n+1} = sin\phi cos\theta\hat{i} + sin\phi sin\theta\hat{j} + cos\phi\hat{k} \tag{4.24}$$

where θ is a uniformly distributed random angle in the range $0 \leq \theta \leq 2\pi$. This orientation cascade process is applied at each multiplicative process to produce vorticity magnitude and direction at each node of the DNS grid. The subgrid velocity field at the DNS grid nodes is found by solving Poisson's equation for the vector potential $\vec{R}$ that is assumed to be a divergence free vector. Then the velocity field is given as the curl of $\vec{R}$. All the calculations for solving the Poisson's equation and curl are conducting in the spectral domain. This explicit multifractal process is used to generate the subgrid velocity field at the nodes of the DNS grid according to Eq 4.26.

$$\nabla^2\vec{R} = -\vec{\omega'} \tag{4.25}$$

$$\vec{u'} = \nabla \times \vec{R} \tag{4.26}$$

4.4 Collisions Frequency without Subgrid Velocity Fluctuations

In this section, the effects of subgrid velocity fluctuations on the motion of dispersed phases are neglected. Drag, pressure gradient and added mass forces of the resolved field are considered in the equation of motion of the particles. Particles tracking has been performed without the SGS velocity fluctuations using the same numerical procedures presented in chapter two to investigate the effects of neglecting the SGS scales on the collisions of particles and bubbles.

4.4.1 Dispersed Phase Model

In order to compare between DNS and LES predictions of collisions frequency, we considered the case of dispersed phases of particles and bubbles having the parameters of case IV given in Table 3.2 and $Re_\lambda = 96$. An Eulerian-Lagrangian approach is used. Stokes drag, added mass and pressure gradient forces of the resolved LES field are considered.

$$\frac{d\vec{V}_i(t)}{dt} = \frac{\vec{\overline{u}}_f - \vec{V}_i(t)}{\tau_i^*} + A\frac{D\vec{\overline{u}}_f}{Dt} \tag{4.27}$$

where $\vec{\overline{u}}$ is the resolved velocity and $\frac{D\vec{\overline{u}}_f}{Dt}$ is the resolved acceleration fields of the carrier phase. An incomplete 3D Hermite interpolation scheme is used to find fluid velocities and tri-linear interpolation to find fluid accelerations at the center of each particle and bubble. The interpolated fluid velocities and accelerations are used to integrate equations of motion of each dispersed phase. Collisions detection algorithm described in chapter 3 is used to find collisions statistical parameter in frame work of LES. Equation 4.27 is solved for a system of solid particles and gas bubbles. The instantaneous positions of the particles are determined by solving the following equations

$$\frac{d\vec{X}_i(t)}{dt} = \vec{V}_i(t) \tag{4.28}$$

where $\vec{X}_i(t)$ and $\vec{V}_i(t)$ are the instantaneous position and velocity of particle i ($i = p$ for solid particles, and $i = b$ for bubbles). Equations 4.28 and 4.27 are solved simultaneously with the LES equations of carrier phase.

Values of dispersed phases void fraction exceed the accepted values for the validity of one-way coupling. This is because of the large number of bubbles and particles used. However, there are no interactions among the groups of dispersed phases; each particle and each bubble

moves as if the other bubbles and particles did not exist in the turbulent field. We used large number of bubbles and particles to obtain large sample for collision statistics.

4.4.2 LES Code Validation

Both LES code and DNS code have the same input parameters for the forcing term in Navier-Stokes equations for case C in table 3.1. DNS results are obtained on a grid $N = 256$ points while LES results are for grid $N = 32$ points. Spectral eddy viscosity subgrid model [9] and multifractal subgrid model [7] are tested here by comparing the turbulent kinetic energy spectra of the LES and DNS. In our LES code, the multifractal subgrid stress model developed by Burton and Dahm [7] failed to drain the turbulent kinetic energy of the large scales. Therefore all LES simulations of particles and bubbles collisions in this work are conducted using spectral eddy viscosity model [9].

The LES energy spectrum is compared at $Re_\lambda = 96$ with the DNS $N = 256$ energy spectrum and good agreement is obtained as shown in figure 4.2.

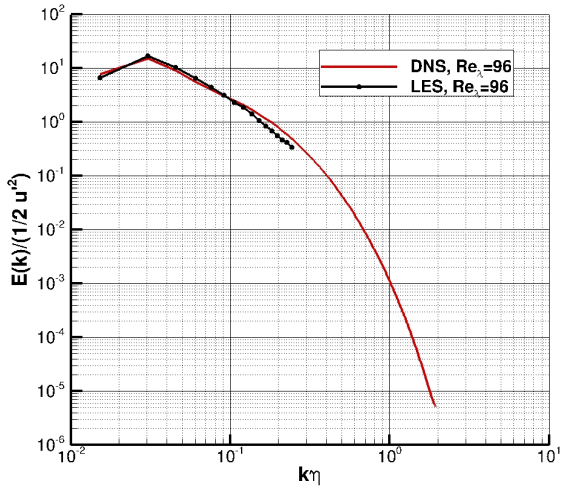

Figure 4.2: Comparison of energy spectrum between the present LES (N=32) and DNS (N=256)

4.4.3 Radial Distribution Function at Contact

Many studies showed that preferential concentration of inertial particles occurs for Stokes numbers near unity (Wang et al. [68], Zhou at al. [83], Fayed and Ragab [15]). Due to centrifugal accelerations particles accumulate in high-strain regions between vortex cores. On the contrary, gas bubbles in liquid tend to migrate into vortex cores, (Maxey [39] and

Fayed and Ragab [15]). Hence particles-bubbles segregation is possible as observed by Julyan et al. [65] in chaotic flows, and it can result in radial distribution functions being less than one as first obtained by Fayed and Ragab [15] in homogeneous isotropic turbulence.

To demonstrate the segregation phenomenon, we consider a case of collisions of solid particles (mono-disperse) and solid particles with gaseous bubbles (bi-disperse) using LES at a turbulence Reynolds numbers $Re_\lambda = 96$. Snapshots of particles and bubbles positions at particles Stokes close to unity $St_p = 0.924$ are shown in Figures 4.3a-4.3b. Particles positions whose centers fall in a thin slice of thickness $2d_b$ that is parallel to the $xy-$plane of the computational box are projected onto the mid-plane of that slice. The projected centers and enstrophy contours are shown Figure 4.3a, where the particles are shown by small white circles. The red isles are regions of high vorticity while the blue isles are regions of high strain rate. Particles accumulate in the high strain regions while bubbles accumulate in high vorticity regions. However, bubbles concentration in the high vorticity regions is less evident in this LES data as compared to DNS as shown Figure 3.10b. This is due to neglecting the effects of subgrid scales velocity fluctuations and associated pressure gradient when the bubbles and particles are tracked in the LES resolved field. The relative positions of particles and bubbles in the slice are shown in Figure 4.3c, they are partially segregated. The segregation is still observed in the LES data due to the pressure gradient term of the resolved scales that forces the bubbles toward the low pressure regions.

Radial distribution functions (RDF) for mono-disperse (particles-particles) $g_{pp}(d)$, and bi-disperse (particles-bubbles), g_{pb}, are shown in Figures 4.4 and 4.5. Radial distribution function has been computed in the frame work of LES without SGS velocity fluctuations (i.e only resolved field is used). Figure 4.4 shows the comparison between DNS radial distribution function and that of LES for particle-particle collisions. For Stokes numbers less than unity $St_p < 1.0$, DNS results are higher than LES while RDF from LES is higher for $1.0 < St_p < 10$. Subgrid velocity fluctuations in DNS tend to move low inertia particles to high strain regions that result in higher RDF than that of LES. In the intermediate range of Stokes number $1.0 < St_p < 10$, large scales motion tend to move particles to high strain regions. We recall the definition of Stokes number that is the ratio of the particle response time to the Kolmogorov time scale. However, when we neglect the subgrid scale velocity fluctuations, the time scale of the resolved field is definitely large than the Kolmogorov time scale. Therefor, the equivalent Stokes number when conducting LES is lower than that in DNS. This results in higher RDF by LES than by DNS as shown in Figure 4.4. For Stokes number greater than ten ($St_p \geq 10.0$), effects of the SGS scales on the RDF are negligible because of the negligible correlation of the particles with motion of SGS fluctuations. Effects of pressure gradient of subgrid scales on the RDF of the mono-disperse phase are negligible because of the small size of the particles where Stokes drag is the leading order term.

Radial distribution functions of the bi-disperse (particle-bubble) $g_{pb}(d)$, are depicted in Figure 4.5. DNS study shows an RDF less than one for the case of particle-bubble due to particles and bubbles segregation. This segregation is due to the pressure gradient term in

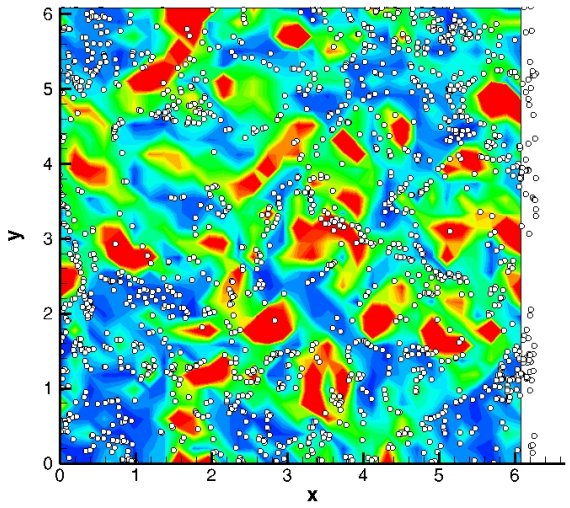

(a) Particles accumulation in high strain regions

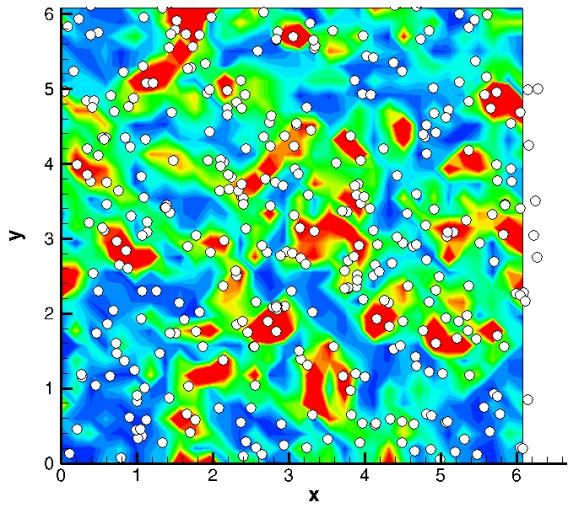

(b) Bubbles accumulation near high vorticity regions

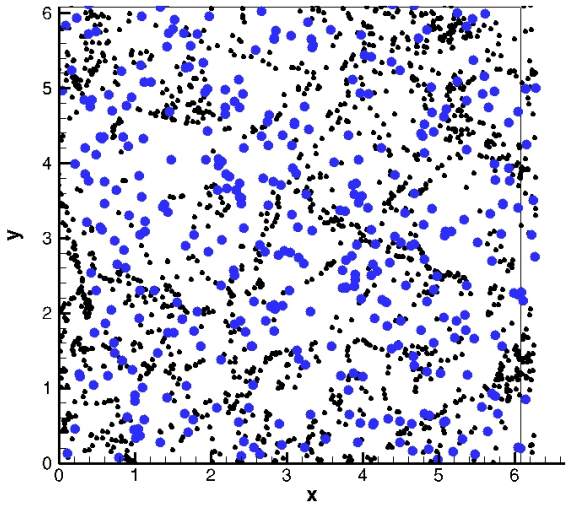

(c) Particles-bubbles segregation

Figure 4.3: Particles-particles preferential concentration and particle-bubble segregation, $Re_\lambda = 96$, LES results

the equations of motion of bubbles. Maximum segregation between particles and bubbles occurs around particles Stokes number of unity. In the present LES study, pressure gradient and added mass forces that stem from SGS scales are not considered. Because of their low inertia, bubbles motion is influenced by the pressure gradient term including the pressure gradient of the SGS fluctuations. As a result of not including the effects of the SGS pressure gradient on the motion of the bubbles, the RDF for particles-bubbles collisions is not as low as that predicted by DNS around Stokes number equal to one. For particles with Stokes number greater than $St_p \geq 10.0$, effects of SGS scales on RDF of particles and bubbles collisions are negligible. Although the effects of pressure gradient is negligible on particles motions at high Stokes numbers, the effects on bubbles motions is still important and shows in the lower than one RDF for particles Stokes number greater than 10. Therefore, SGS velocity fluctuations and SGS carrier phase acceleration are needed for accurate calculations of RDF in LES. Comparison with Zaichik et al. [78] model is also included in Figure 4.5. *Strictly speaking, application of Zaichik et al. [78] model model should be limited to heavy small particles. Its application to the case of particle-bubble collisions may be questionable, but it is presented here only for reference.*

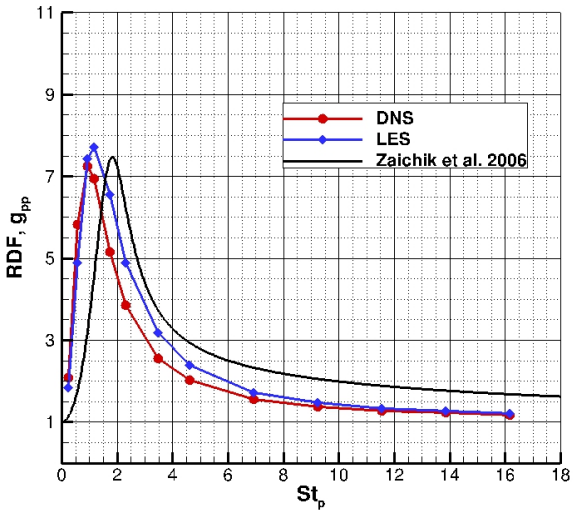

Figure 4.4: RDF comparison of DNS, present LES and Zaichik et al. [78] model for particle-particle collisions

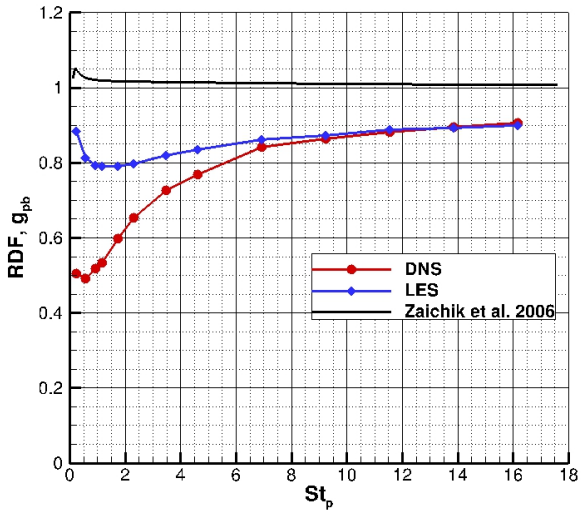

Figure 4.5: RDF comparison of DNS, present LES and Zaichik et al. [78] model for particle-bubble collisions

4.4.4 Mean Radial Relative Velocity

Effects of SGS velocity fluctuations in the LES on the mean radial relative velocity at contact $\langle |w_r(d)| \rangle$ of particle-particle have been shown in Figure 4.6 by comparison with that of the DNS. Subgrid turbulent fluctuations increase the $r.m.s$ fluctuations of the particles that results in higher radial relative velocity at contact $\langle |w_r(d)| \rangle$ by DNS than that by LES for Stokes numbers $St_p < 10$. Effects of SGS turbulent fluctuations on the radial relative velocity of the mono-disperse is negligible for Stokes number $St_p \geq 10$.

Bubbles represent low inertia particles. Subgrid turbulent fluctuations affects the $r.m.s$ fluctuations of bubbles as well as small inertia particles. As shown in Figure 4.7, differences in radial relative velocity at contact $\langle |w_r(d)| \rangle$ of particle-bubble from DNS and that of LES are negligible at small Stokes number. At high particles Stokes number, particles do not respond to the small scale fluctuations while bubbles are very sensitive to small scales. For particle Stokes number greater than 8, it is observed that radial relative velocity at contact $\langle |w_r(d)| \rangle$ from LES is higher than that of DNS. The higher level in LES is unexpected, but it is due to the less accurate interpolation in the coarse grid of the LES. This interpolation error affects the motion of the bubbles more than the particle's motion because at high stokes number the particles will have higher relative velocity to the carrier phase than the bubbles.

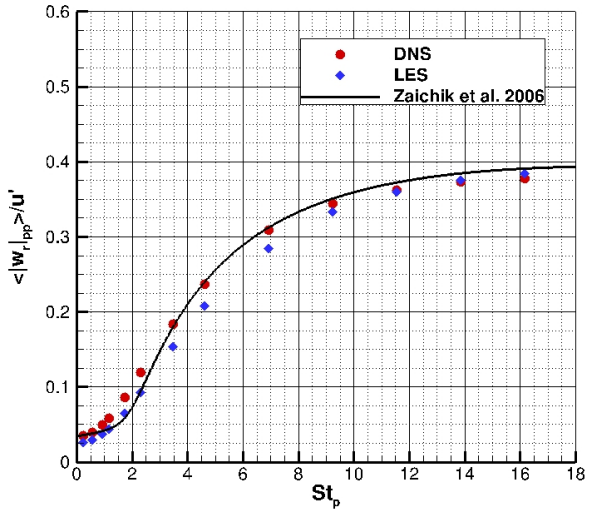

Figure 4.6: $\langle |w_r| \rangle$ comparison of DNS, present LES and Zaichik et al. [78] model for particle-particle collisions

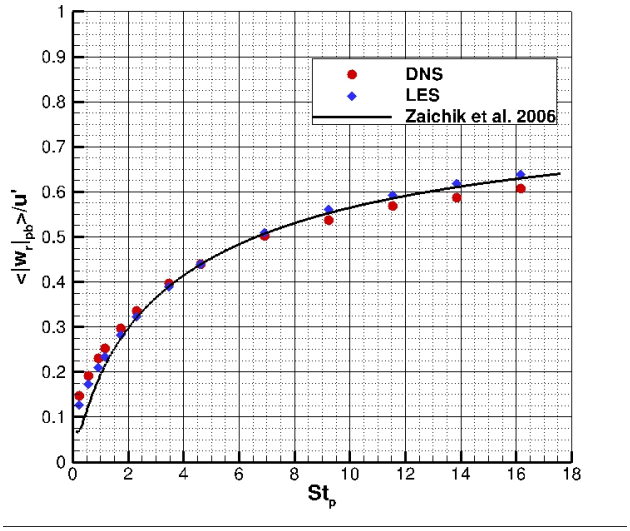

Figure 4.7: $\langle |w_r| \rangle$ comparison of DNS, present LES and Zaichik et al. [78] model for particle-bubble collisions

4.4.5 Collisions Kernel

LES collisions kernel for mono-disperse (particle-particle) normalized by Saffman-Turner [53] is compared with that of the DNS and Zaichik et al. [78] model in Figure 4.8. Collisions kernel calculated from DNS and LES are approaching collisions kernel calculated from Saffman-Turner [53] for very small Stokes number. For Stokes number less than 2.0 Collisions kernel from LES is lower than that of DNS because of lower RDF and radial relative velocity as shown in Figures 4.4- 4.6. The higher collisions kernel in LES for Stokes number greater than 2.0 is due to the over prediction of RDF in that range of Stokes number. Jin et al. [25] have reached the same conclusion. There is qualitative agreement among collisions kernel calculated from DNS, LES and Zaichik et al. [78] theoretical model.

Collisions kernel for bi-disperse (particle-bubble) normalized by $u'd^2$, where $d = (d_p + d_b)/2$ is the collision radius, from LES is compared with that of the DNS and Zaichik et al. [78] model in Figure 4.9. LES collisions kernel for particle-bubble is higher than that of DNS collisions kernel for the investigated range of Stokes number. This is due to higher RDF of the bi-disperse for $0 \leq St_p \leq 10.0$ and higher particle-bubble relative velocity $\langle |w_r(d)| \rangle$ at large Stokes number.

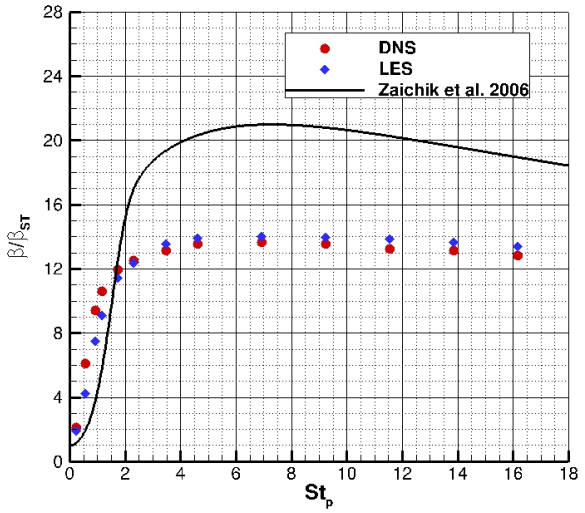

Figure 4.8: Collisions kernel comparison of DNS, present LES and Zaichik et al. [78] model for particle-particle collisions

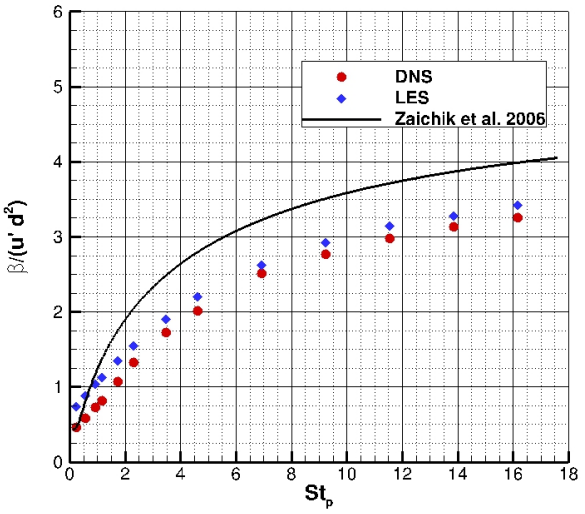

Figure 4.9: Collisions kernel comparison of DNS, present LES and Zaichik et al. [78] model for particle-bubble collisions

4.5 Effects of Subgrid Scale Fluctuations

In Large-Eddy simulations, large scales of the carrier phase fluctuations are resolved and effects of small scales on the motion of large scales are modeled. Small scales are important for tracking particles and bubbles of sizes on the order of Kolmogorov′s length scale as shown in the previous section. The equation of motion of dispersed phases is given by

$$\frac{d\vec{V}_i(t)}{dt} = \frac{(\vec{\overline{u}}_f + \vec{u'}_f) - \vec{V}_i(t)}{\tau_i^*} + A\left(\frac{D\vec{\overline{u}}_f}{Dt} + \frac{D\vec{u'}_f}{Dt}\right) \tag{4.29}$$

In LES, the subgrid velocity fluctuations $\vec{u'_f}$ and its total time derivative should be synthesized using data from simulated large resolved scales. In this dissertation, we investigated different approaches for the synthesis of $\vec{u'_f}$. Synthesis of the acceleration term is still a challenge and is left for future work. It is important for bi-disperse particle-bubble collisions at small particles Stokes number.

The subgrid velocity filed is synthesized in two steps. The first step is the generation of the subgrid vorticity field from the vorticity of the large resolved scales using a multifractal cascade. The second step is to determine the subgrid velocity filed knowing its vorticity filed. The second can be accomplished either by using Biot-Savart law or by solving a Poisson's equation for the vector potential and then computing the velocity by taking the curl of the potential. Here we solved Poission's equation.

To test the Poisson's solver in the spectral domain, we conducted a priori test in which the sugrid vorticity is obtained by filtering a DNS velocity field, and then computing the subgrid vorticity. We then solve Eq 4.25 and use Eq 4.26. from the resolved large scales to to Poisson′s solver is used to calculate the velocity field from a vorticity field. Figures (4.10a- 4.12b) depict the comparison between the subgrid velocity field obtained from the filtered DNS velocity field and the subgrid velocity components from the Poisson Solver. The comparison shows that both velocity fields are identical as expected. This means that if we are able to construct the right subgrid vorticity field, we can easily obtain an appropriate subgrid velocity field.

The multifractal methodology presented in Section 4.3 is used constructed the subgrid fluctuations from the enstrophy of the resolved scales. In this methodology, a sharp cut-off filter is used to obtain u_i^{Δ} and Eq 4.18 to estimate Q_{sgs} at the center of each LES cell. The estimated subgrid enstrophy Q_{sgs} in Eq 4.20 is used to calculate the subgrid vorticity magnitude. The subgrid vorticity directions are computed according to Eqns (4.23 - 4.24). This vorticity field is used as an input to Poisson's solver to find the subgrid velocity field.

We note that the LES is conducted on a coarse grid of $N = 32$ while the DNS is conducted of a grid $N = 256$. Figures 4.13a and 4.13b shows a comparison between the synthesized subgrid enstrophy filed and subgrid enstrophy field obtained by high-pass filter of a DNS data. The estimated subgrid enstrophy shows random distribution while the filtered DNS enstrophy

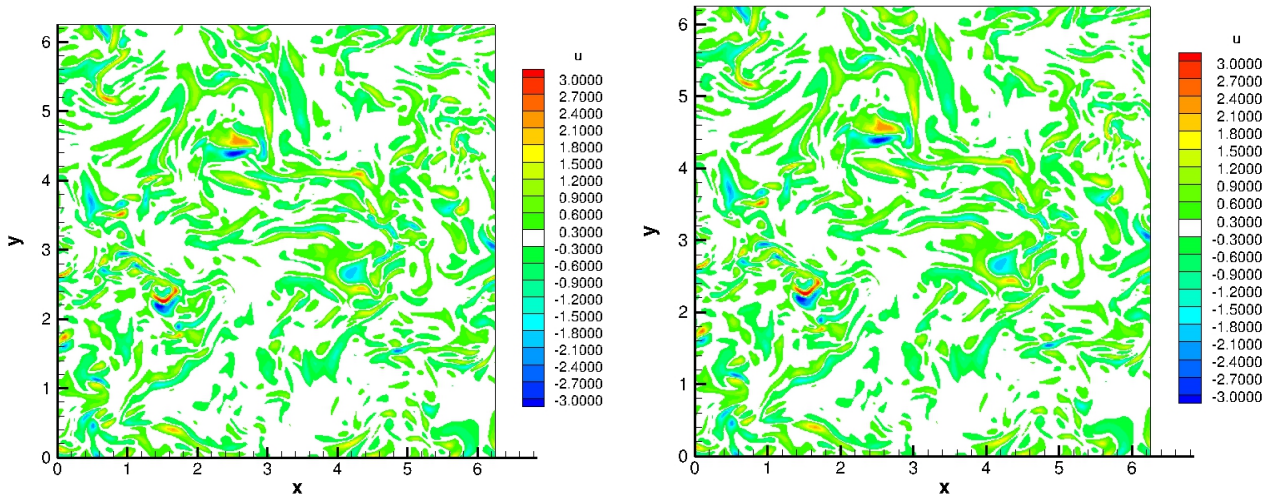

(a) u component from Poisson's solver

(b) u component from DNS

Figure 4.10: Subgrid u-velocity component

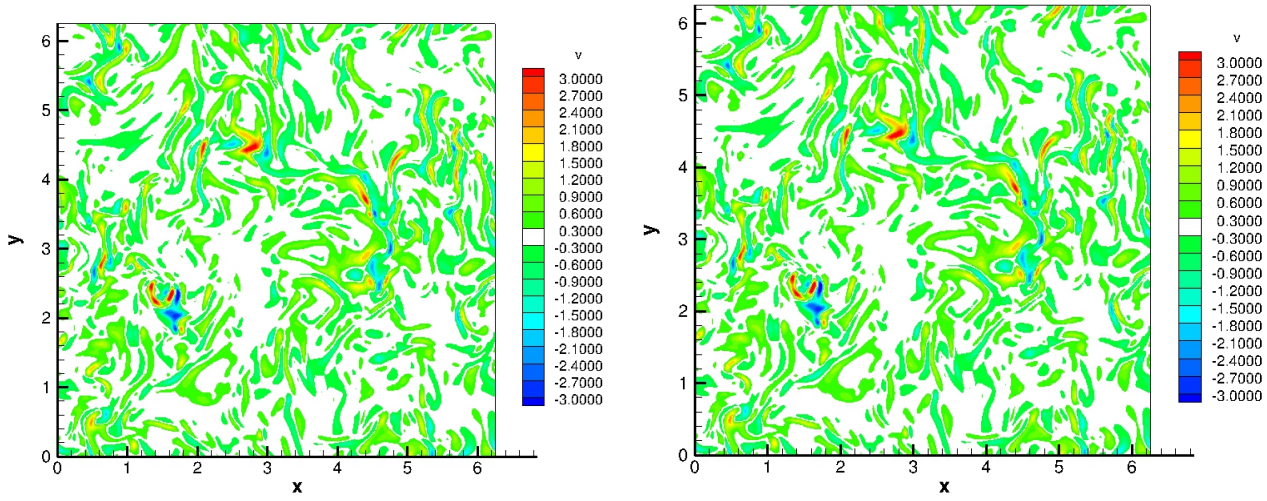

(a) v component from Poisson's solver

(b) v component from DNS

Figure 4.11: Subgrid v-velocity component

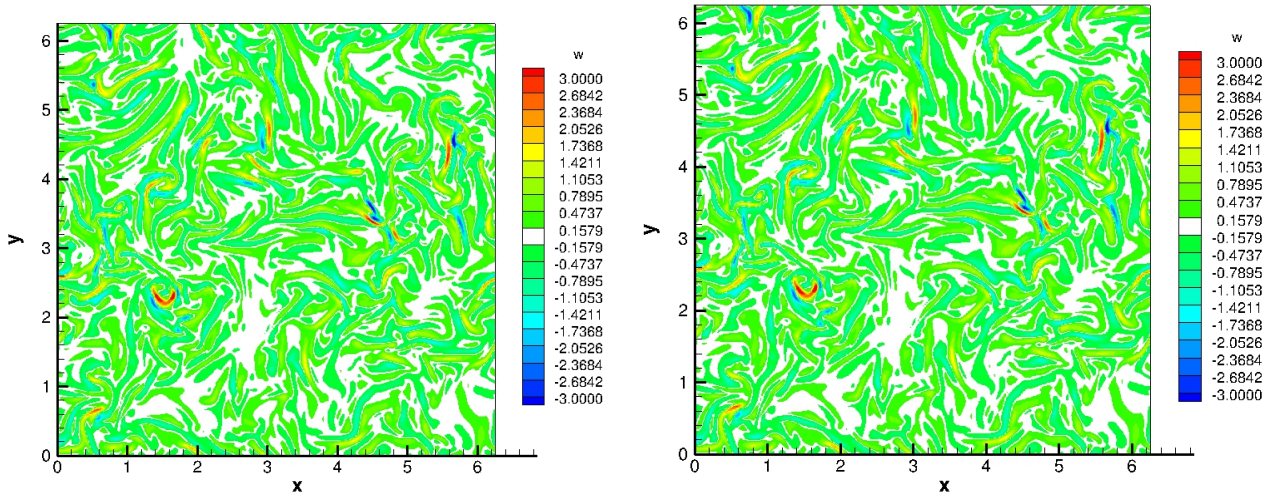

(a) w component from Poisson's solver

(b) w component from DNS

Figure 4.12: Subgrid w-velocity component

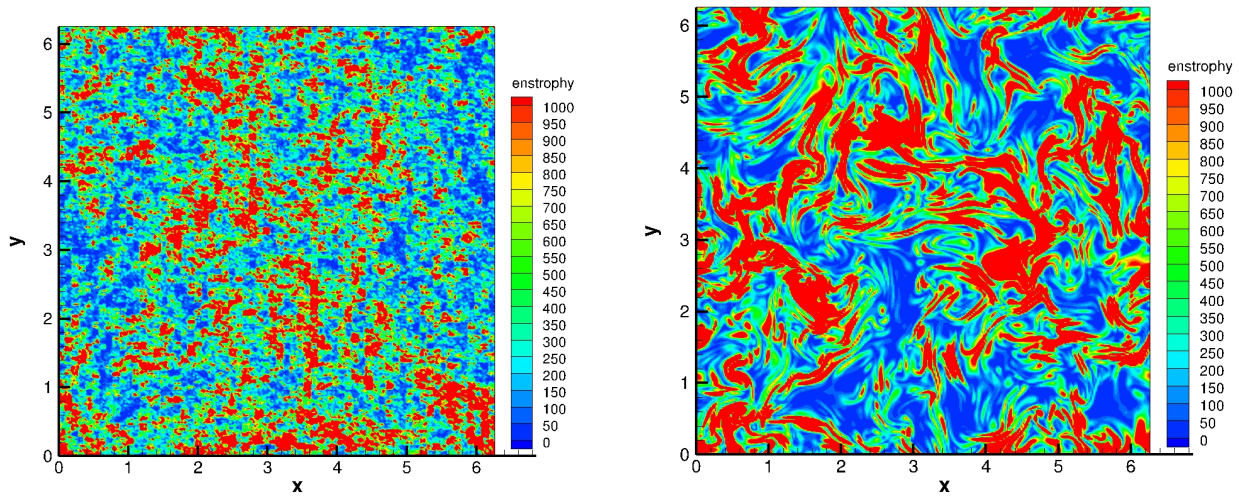

(a) Synthesized subgrid enstrophy field

(b) Filtered DNS subgrid enstrophy field

Figure 4.13: Comparison between synthesized and DNS filtered subgrid enstrophy filed

field shows coherent structures. This happens due to the random number distribution used to determine the multipliers M_n used in the multiplicative cascade process. The multiplicative cascade processes tend to concentrate more energy in the very small scales. An alternative approach for distributing the vorticity among the different subgrid scales should be used.

We also conducted particles and bubbles tracking in a velocity filed whose large scales are determined by an evolving LES whereas its subgrid velocity fluctuations are given by a filtered DNS field. The large scales of the DNS filed are removed by a spectrally sharp filter. This subgrid velocity field is frozen (does not change with time) and added to the resolved velocity field as needed by Eq 4.29. This approach is not practical since the purpose of LES is used for flow cases where DNS is not feasible; but it is done here only for the sake of comparison with other approaches.

The resolved and subgrid velocity components at the instantaneous positions of particles and bubbles are found by Hermite interpolation. This means that Hermite interpolations are conducted twice; first on the coarse grid for the LES field and then on the fine grid for the subgrid field. The two interpolated velocities are added and used in the equations of motion of particles and bubbles (see Eq 4.29). Tri-linear interpolation on the coarse LES grid is used to find the acceleration of the resolved field as needed by Eq 4.29. The subgrid acceleration field $D\vec{u_f'}/Dt$ is dropped in this study.

Figures 4.4 and 4.5 show the RDF for mono (particle-particle) and bi-disperse (particle-bubble) collisions obtained by DNS, LES without the effects of subgrid velocity on particle tracking, LES with frozen subgrid velocity field, and subgrid velocity field synthesized by the multifractal approach. For particle Stokes number greater than 2, including the subgrid fluctuations by different approaches produced minor changes on the RDF. Around Stokes number, the RDF by LES with frozen subgrid field is in better agreement that of DNS. For the particle-bubble RDF, adding the subgrid velocity field produced minor changes and relative to neglecting the effects of subgrid velocity fluctuations. As expected the effects of the SGS scales on the RDF are negligible for large Stokes number ($St_p \geq 10.0$).

It is clear now that just adding any subgrid velocity field to the resolved velocity field is not enough to improve the results for RDF of the mono/bi-disperse phases. This subgrid velocity field has to be dynamically correlated to the motion of the large scales and subgrid acceleration field $D\vec{u_f'}/Dt$ has to be considered especially for bubble-particles collisions..

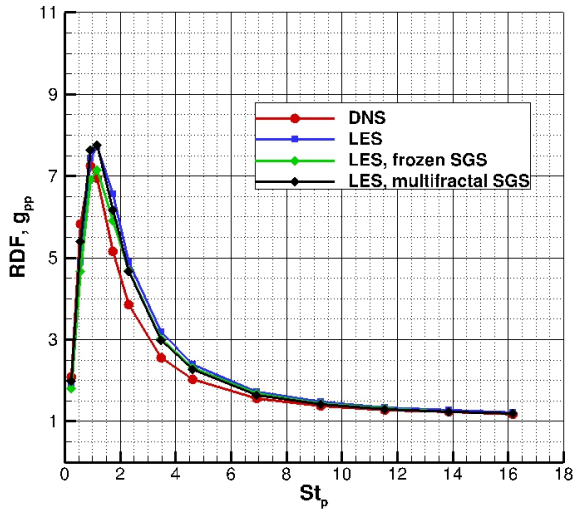

Figure 4.14: RDF comparison of DNS, LES and LES with subgrid velocity field for particle-particle collisions

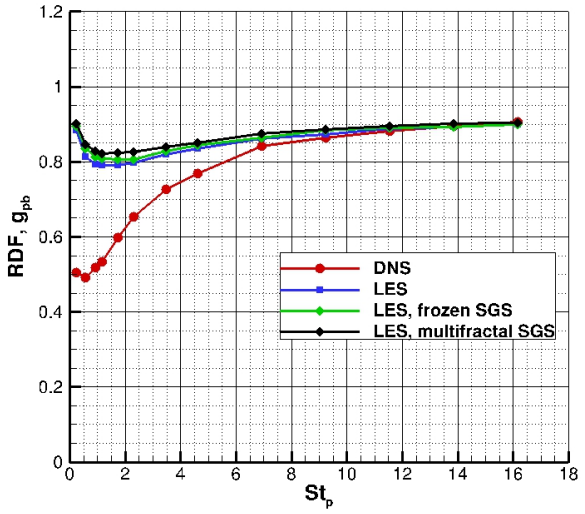

Figure 4.15: RDF comparison of DNS, LES and LES with subgrid velocity field for particle-bubble collisions

Figures 4.16- 4.17 show the effects of adding SGS velocity fluctuations to the LES velocity filed on the mean radial relative velocity at contact $\langle |w_r(d)| \rangle$ by comparison with that of the DNS. Small improvements are observed at small Stokes number. Radial relative velocity at contact $\langle |w_r(d)| \rangle$ is higher when adding the multifractal SGS than when using frozen SGS field. This is due to the way of constructing the multifractal field using a cascade multiplicative process which takes the energy from large scales and impart it to small scales randomly. Effects of subgrid velocity field on the collisions kernel of mono-disperse and bi-disperse are shown in Figures 4.18a- 4.18b. Collisions kernel from LES is lower than that of DNS for Stokes number $St_p \leq 2$ and higher than collisions kernel from DNS with and without SGS. For particles-bubbles collisions kernel from LES is consistently higher than that of DNS because of higher RDF at small Stokes number and higher radial relative velocity at high Stokes number.

We conclude from this study that for accurate particle tracking in LES the subgrid velocity fluctuations must be dynamically realizable field (temporally and spatially correlated with the large scale motion). Adding random SGS velocity fluctuations is not enough to capture the correct radial distribution functions of dispersed phases especially for bubbles-particles collisions where the pressure gradient term (or acceleration $D\vec{u_f'}/Dt$) is responsible for particle-bubble segregation around particle Stokes number near one.

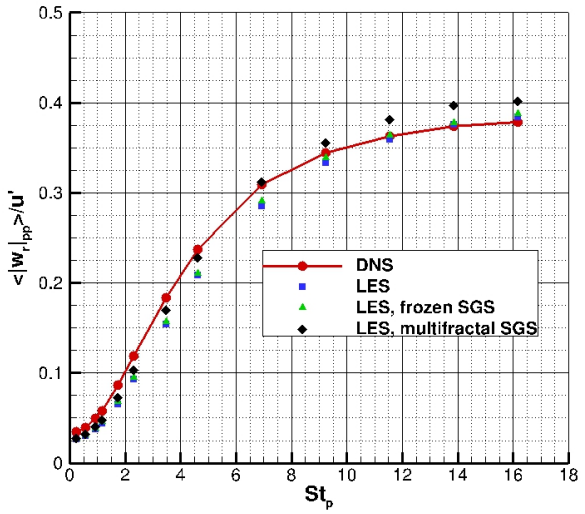

Figure 4.16: $\langle |w_r| \rangle$ comparison of DNS, LES and LES with subgrid velocity field for particle-particle collisions

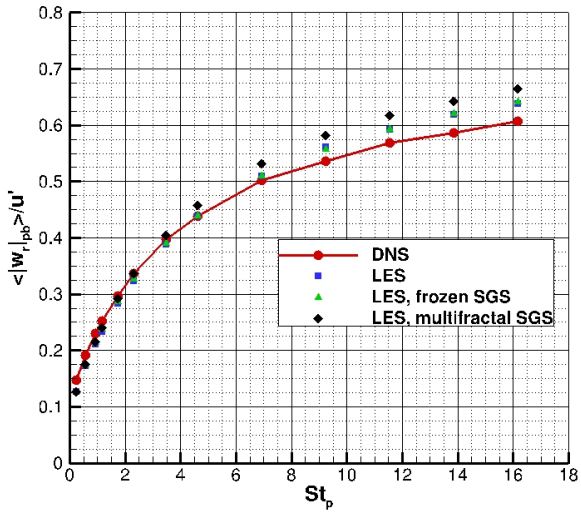

Figure 4.17: $\langle |w_r| \rangle$ comparison of DNS, LES and LES with subgrid velocity field for particle-bubble collisions

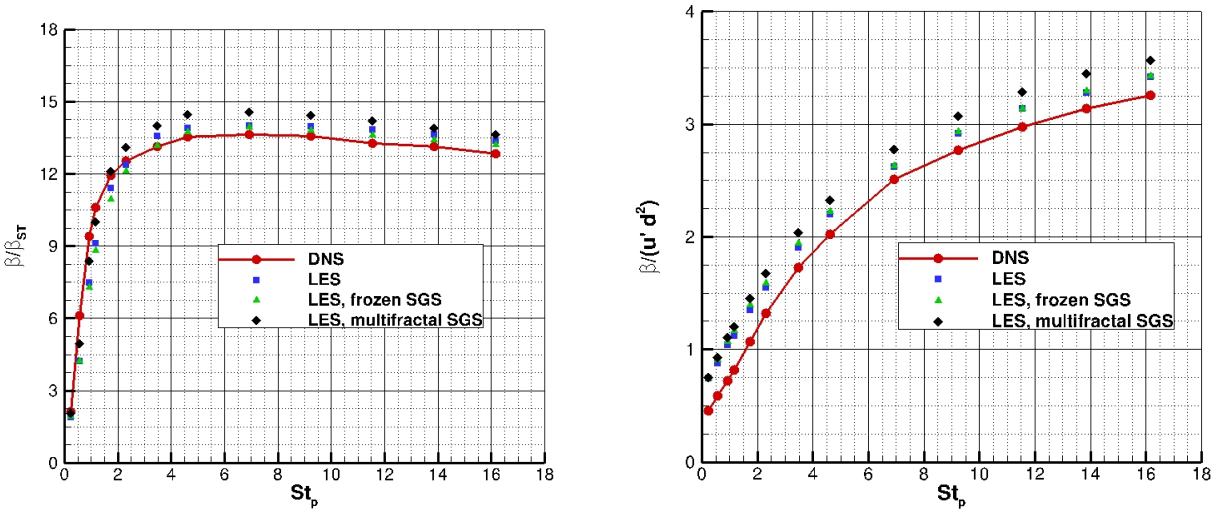

(a) Mono-disperse phase

(b) Bi-disperse phase

Figure 4.18: Effect of subgrid scales on collisions kernel

Chapter 5

Two-Phase Flow in Wemco-0.8 m^3 Cell and Application of CFD-Based Flotation Model

5.1 Introduction

Hydrodynamic processes in minerals froth flotation machines are examples of complex multiphase flow phenomena. The idea of minerals flotation is based on collisions and attachment of the valuable minerals particles to gaseous bubbles in direct flotation. In reverse flotation, the gangue material particles are floated and valuable minerals particles sink to the machine bottom. Collisions rate between particles and bubbles is a critical factor for minerals recovery by flotation machines. Collisions rate depend on the local turbulent dissipation rate in the pulp phase. Other factors such as attachment and detachment rate of particles-bubbles aggregates depend on turbulent dissipation rate as well as surface chemistry of particles and bubbles. Two-phase flow simulations of flotation machines provide spatial distribution of air void fraction and turbulent dissipation rate. A CFD-based flotation model has been developed in this work as an application of the theoretical collisions model. The model provides local values of collisions rate between particles and bubbles as well as probabilities of attachment, collisions and stabilization. In this chapter we present flotation model as a first rate equation. The rate constant in this equation depends on the local collisions frequency, probability of attachment, and probability of stabilization. The CFD-based flotation model and results presented in this chapter have been transferred as a technical report ([49]) to FLSmidth Minerals Inc, Salt Lake City, UT, USA. Engineers at FLSmidth minerals Inc have used the model to develop more efficient rotors and stators for their flotation machines [24] and to optimize the flotation process of fine and coarse particles [20]

5.2 Flotation Model: First-Order Rate Equation

The objective of a flotation model is to predict the rate of recovery (rate of mass flow of useful minerals collected from a flotation cell.) Flotation is usually modeled as a first-order rate process that is given by the fundamental equation

$$\frac{dn_{p1}}{dt} = -k_1 n_{p1} n_b + k_2 n_a \tag{5.1}$$

where n_{p1} is the particle number density (number of particles per unit volume) of free particles (not attached to bubbles), n_b is the number density of bubbles available for attachment (not fully loaded bubbles), n_a is the number concentration of particle-bubble aggregates (bubbles that cannot accept more particles but can loose particles by detachment mechanisms), k_1 is the particle-bubble attachment rate constant, and k_2 is the particle-bubble detachment rate constant. We note the difference in the dimensions (units) of k_1 (m^3/s) and k_2 (1/s). The total particle number concentration n_{pT} is

$$n_{pT} = n_{p1} + n_{p2} \tag{5.2}$$

where n_{p2} is the number concentration of particles attached to bubbles. All number concentrations are functions of time and location in a flotation cell.

Theoretical flotation models have been developed by Yoon and Lutrell [76], Pyke et al. [48], Bloom and Heindel [5], and Koh and Schwarz [30] among others. The model presented here is largely based on the model summarized by Koh and Schwarz [30], referred here to as KS2006. In KS2006, a bubble is either fully loaded (cannot accept more particles) or clean (no particles attached). The number of particle-bubble aggregates is proportional to the total number of bubbles,

$$n_a = b n_{bT} \tag{5.3}$$

where b is an average loading parameter, which varies with time and position. The number of clean bubbles (those available for attachment) is

$$n_b = (1 - b) n_{bT} \tag{5.4}$$

The rate equation (5.1) can now be written as

$$\frac{dn_{p1}}{dt} = -k_1 (1 - b) n_{p1} n_{bT} + k_2 b n_{bT} \tag{5.5}$$

The number of particles (S) that can be attached to a bubble is given by the ratio of surface area of the bubble to the projected area of the particle.

$$S = 4\left(\frac{d_b}{d_p}\right)^2 \tag{5.6}$$

Such an estimation is not realistic. In KS2006, only half of that number is assumed as a first approximation.

$$S_{max} = 0.5S = 2\left(\frac{d_b}{d_p}\right)^2 = \frac{n_{p2}}{bn_{bT}} \tag{5.7}$$

Rearranging, we obtain b,

$$b = \frac{n_{p2}}{S_{max}n_{bT}} = \frac{n_{p2}}{2n_{bT}}\left(\frac{d_p}{d_b}\right)^2 \tag{5.8}$$

5.3 Attachment Models

Collisions frequency (Z_{12}) of two groups of disperse species (e.g. particles and bubbles) is the number of collisions per unit volume per unit time ($\mathrm{m}^{-3}\ \mathrm{s}^{-1}$). It is proportional to the product of the number densities n_1 and n_2 of the two groups ($Z_{12} = \beta n_1 n_2$), where β is called the collisions kernel (m^3/s). The attachment rate constant (k_1, m^3/s) is defined as the product of particle-bubble collisions kernel times probabilities (or efficiencies). This is because not every collision event leads to successful attachment of a particle to a bubble. Thus, the attachment rate constant is written as

$$k_1 = \beta P_c P_a P_s \tag{5.9}$$

where P_c, P_a, and P_s are probabilities of particle-bubble collision, adhesion, and stabilization. Multiplication by P_c is questionable since it should be considered as a part of the collisions kernel. Apparently including P_c is a remnant of the original model that was developed under quiescent conditions. This collisions probability P_c should be eliminated because collisions kernel is modeled under turbulent conditions, and the assumption of laminar flow is irrelevant. When turbulence is the mechanism of collisions of particles and bubbles, "quiescent" conditions should be defined as the turbulent fluctuations u'_f and turbulent dissipation rate that maximizes the attachment rate and minimizes detachment.

The collision kernel β is perhaps the most important ingredient of the attachment rate constant k_1. For turbulent flow, two classical models are in use. The first is Saffman and Turner model [53], which is applicable in the limit of zero particle Stokes number. The second is Abrahamson model [1] which is applicable in the limit of infinite particle Stokes number. The form of the later model is usually written [58] as

$$\beta = 5\left(\frac{d_p + d_b}{2}\right)^2 \left(U_p^2 + U_b^2\right)^{1/2} \tag{5.10}$$

where U_p and U_b are the turbulent (rms) fluctuating velocities of the particles and bubbles relative to the carrier liquid, respectively. Leipe and Mockel [35] formula (not the original formula by Abrahamson [1]) is used for these velocities,

$$U_i = \frac{0.4\epsilon^{4/9} d_i^{7/9}}{\nu_f^{1/3}} \left(\frac{|\rho_i - \rho_f|}{\rho_f}\right)^{2/3} \tag{5.11}$$

where ϵ is dissipation rate of the turbulent kinetic energy per unit mass (W/kg), ν_f and ρ_f are the kinematic viscosity and density of the liquid, respectively. ρ_i and d_i are density and diameter of the colliding particles $i = p$ for particles and $i = b$ for bubbles. The mass density for a bubble is assumed to be equal $0.5\rho_f$, as if the bubble mass is the virtual mass of a spherical bubble. Equation (5.11) implies that high dissipation results in higher collision rates between bubbles and particles, and in this regard high dissipation has favorable effects on flotation.

The probability (efficiency) of collision P_c is given by a formula due to Yoon and Luttrell [76],

$$P_c = (\frac{3}{2} + \frac{4}{15} Re_b^{0.72}) \frac{d_p^2}{d_b^2} \tag{5.12}$$

where the bubble Reynolds number is defined by $Re_b = d_b U_b / \nu_f$. In the actual implementation of the model, Eq (5.12) is used if $P_c \leq 1$ otherwise $P_c = 1$.

The expression for probability of adhesion P_a is also derived by Yoon and Luttrell [76],

$$P_a = sin^2(2tan^{-1} exp[\frac{-(45 + 8Re_b^{0.72}) U_b t_{ind}}{15 d_b (d_b/d_p + 1)}]) \tag{5.13}$$

where t_{ind} is the induction time, which is determined by an empirical formula due to Dai et al. [11]:

$$t_{ind} = \frac{75}{\theta} d_p^{0.6} \tag{5.14}$$

where t_{ind} is measured in seconds, θ is particle-bubble contact angle in degrees, and d_p in meters.

The formula proposed by Schulze [60] and modified by Bloom and Heindel [5] for the probability of stabilization P_s is used

$$P_s = 1 - exp[A_s(1 - 1/min(1, Bo^*))] \tag{5.15}$$

where the modified Bond number is defined by

$$Bo^* = \frac{d_p^2[\Delta\rho g + 1.9\rho_p\epsilon^{2/3}(d_p/2 + d_b/2)^{-1/3}] + 1.5d_p(4\sigma/d_b - d_b\rho g)sin^2(\pi - \theta/2)}{|6\sigma sin(\pi - \theta/2)sin(\pi + \theta/2)|} \tag{5.16}$$

where $A_s = 0.5$ is an empirical constant suggested by Bloom and Heindel [5]. And where σ is the surface tension, $\Delta\rho = \rho_p - \rho_f$, and g is the gravitational acceleration.

5.4 Detachment Models

The particle-bubble detachment rate constant (k_2) is defined by

$$k_2 = Z_2 P_d = Z_2(1 - P_s) \tag{5.17}$$

The probability of detachment P_d is assumed to be equal to $(1 - P_s)$. KS2006 justified the inclusion of P_s in both k_1 and k_2 because the processes involve different turbulent eddies acting independently of each other. The detachment frequency Z_2 is given by Bloom and Heindel [4] as

$$Z_2 = \frac{\sqrt{C_1}\epsilon^{1/3}}{(d_p + d_b)^{2/3}} \tag{5.18}$$

where $C_1 = 2$ is an empirical constant. We note in Equation (5.18) the adverse effects of dissipation, that high dissipation results in destabilization of particle-bubble aggregates.

5.5 Two-Phase Flow in Wemco-0.8 m^3 Cell

Wemco is a self-aerated mechanical flotation machine. The rate of air flow through the machine cannot be arbitrarily specified, and can be determined only by operating the machine. For a given machine, the rate of air flow depends on the rotor speed (RPM) among other operating conditions such as rotor submergence depth. Moreover, the rate of air flow may vary significantly with time to the extent that air is temporarily "exhaled" by the standpipe instead of being "inhaled". Computer simulations of such a machine should predict the time-history of the rate of air flow, and the average rate is an output of the simulations. The unknown rate of air flow and the possibility of "breathing" require careful treatments of the standpipe and pulp-froth interface boundary conditions.

5.5.1 Cell Geometry and Simulations Parameters

The main components of Wemco-0.8m^3 machine as shown in Figure 5.1 include a six-blade rotor, a disperser, a draft tube, and standpipe. Details of the different components are shown in Figure 5.2a-5.2d. The disperser has 34 holes arranged in two parallel horizontal rows. Seventeen semi-circular rods are attached to the inner surface of the disperser. Air is drawn into the machine through a hole in the top of standpipe. The machine is assembled in Figure 5.3. The simulated Wemco-0.8m^3 model does not have a disperser hood or tank baffles. The main dimensions are given in Table 5.1.

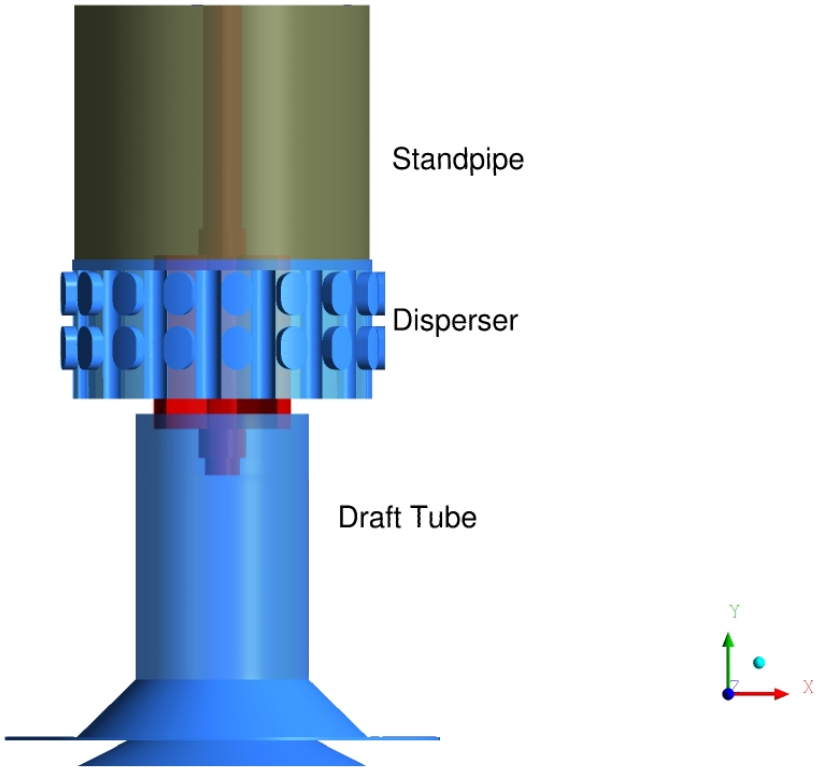

Figure 5.1: Core of the Wemco-0.8m^3 machine: Rotor, disperser, draft tube, and standpipe

The boundary treatment at the air opening in top of the standpipe allows air to enter or exit from the standpipe above rotor. There is no valve or any other device that obstructs air from flowing back to the ambient through the air inlet hole. If air flow is reversed it may also carry a small amount of water with it. A container, which is connected to the standpipe only through the air inlet hole, is added for the purpose of numerical simulations only. Its function is to hold any water which might be expelled and is to be recovered when air flows back into the machine. Atmospheric pressure is prescribed at the top of that container. This treatment is unique to the present simulations of a self aerated machine, and it allows the machine to "breath" for some operating conditions.

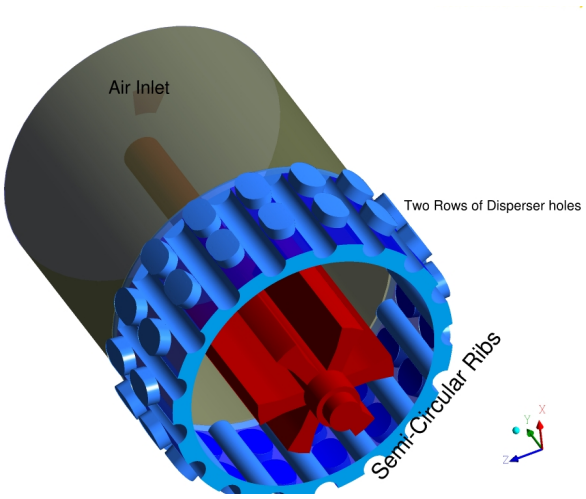

(a) Six-blade rotor, disperser and standpipe

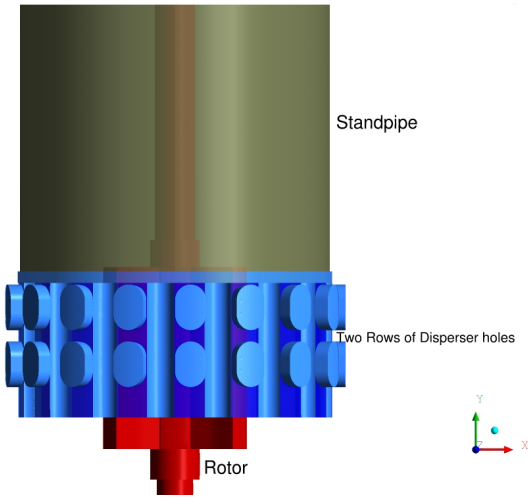

(b) Relative vertical position of rotor and disperse

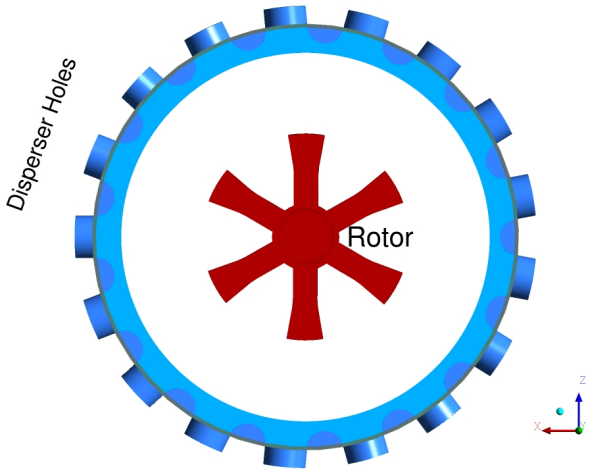

(c) Radial clearance between rotor and disperser

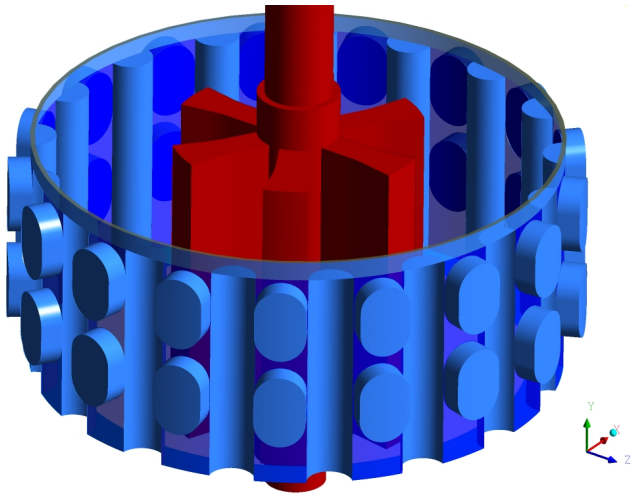

(d) Rotor and disperser

Figure 5.2: Details of Wemco-0.8m^3 rotor, disperser, and standpipe

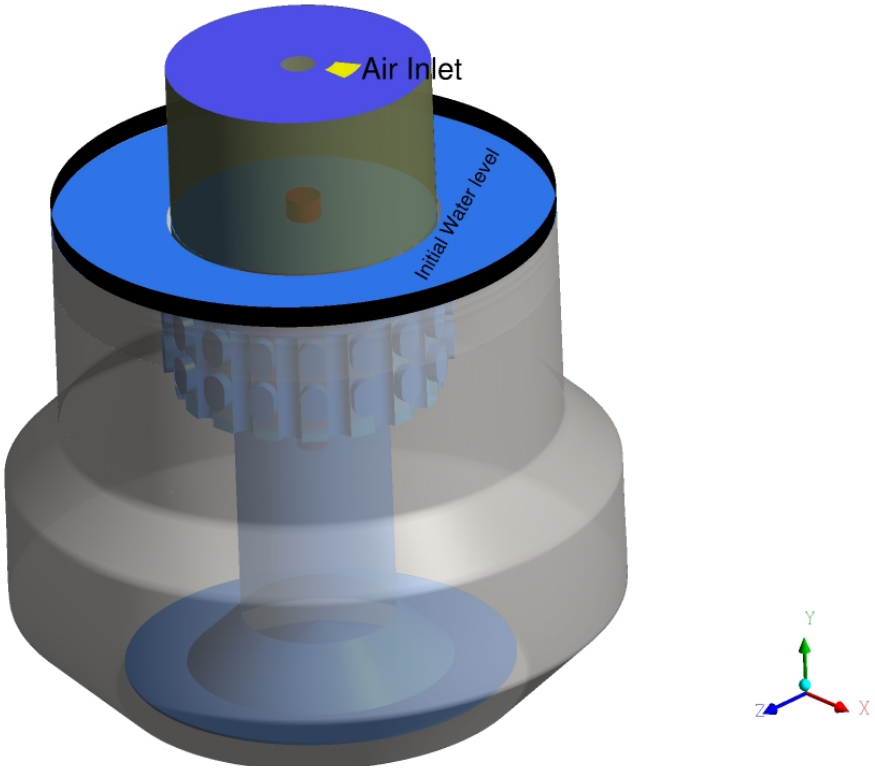

Figure 5.3: Wemco-0.8m^3 assembly: tank, air-inlet and initial water level

An important operating assumption used in the present simulations is that the amount of water in the tank remains constant during operation. That is to say no water is allowed to flow over the weir. This condition may not be precisely satisfied in the actual machine operation; but it is a realizable situation. To guarantee that no water exits the tank, the tank wall is extended vertically above the weir edge thereby creating an overflow tank. The overflow tank exists only in the computer model and is not a part of the actual machine. Atmospheric pressure is prescribed at the top of the overflow tank. The actual tank is initialized with 100% water up to a certain level to be defined later, and the rest of the actual tank and overflow tank are initialized with 100% air. The function of the overflow tank is to permit the water level to rise due to the accumulation of air in the pulp, and at the same time it does not allow water to exit the computational domain. As air accumulates in the pulp, the initial water surface rises pushing air out of the top of the extended tank. If air flow direction is reversed and air is expelled from the standpipe, air will enter from the top of the overflow tank in response to the dropping pulp surface in the tank. No boundary conditions are needed at the interface between the actual tank and the overflow tank. The governing equations of the two-phase flow are solved in both tanks simultaneously allowing air and water to flow back and forth between the tanks as required by the transport equations.

Table 5.1: Main dimensions and operating conditions for Wemco-0.8m^3 cell

Quantity	Magnitude
Rotor maximum diameter, D_r (m)	0.22
Rotor blade height, H_r (m)	0.257
Standpipe diameter, D_p (m)	0.438
Standpipe height, H_p (m)	0.383
Draft tube inside diameter, D_d (m)	0.256
Tank maximum diameter, D_t (m)	1.016
Rotor speed, N (rpm)	620
Rotor tip speed, U_t (m/s)	7.14
Reynolds number, $Re = \rho N D^2/60\mu$	0.5×10^6

As shown in Figure 5.4, the initial water level in the actual tank is 851.58 mm above the tank bottom; which is 36.28 mm below the overflow level (edge of actual tank). The rotor submergence depth (distance between initial free surface and rotor top) is 94.45 mm. The part of the computational domain below the initial water level is initialized ($t = 0$) with 100% water and the part above that level is initialized by 100% air.

5.5.2 Air Flow Rate and Power

The rate of air flow drawn into the machine varies with time as shown in Figure 5.5a for three assumed bubble diameters. It is evident that the air flow is unsteady and momentarily may reach zero or become slightly negative; air is flowing out of the standpipe. Little effects of the bubble diameter is observed. The power (the computed rotor torque is multiplied by angular velocity) depicted in Figure 5.5b also varies with time; it also shows negligible effects of bubble diameter. We note that the computed power does not account for power consumed to generate the bubbles by break down the continuous air stream. For bubble diameter of 0.7 mm, the running average of air flow rate and power defined by

$$\tilde{Q}_a(t) = \frac{1}{t}\int_0^t Q_a(\tau)d\tau \tag{5.19}$$

$$\tilde{P}(t) = \frac{1}{t}\int_0^t P(\tau)d\tau \tag{5.20}$$

are shown in Figure 5.6. The time averaged air flow rate is converging to 0.35 m^3/min and the power to 1.43 kW. The time-averaged air capacity coefficient $C_a = Q_a/ND_r^3$ is 0.053. Nelson et al. [43] reported measured values of C_A for large Wemco cells (for example Wemco-160 SmartCell) in the range 0.13 to 0.17; which are much greater than the present CFD predicted value for the smaller 0.8m^3 model. However, the CFD predicted air rise velocity $Q_a/A_c = 0.35/0.382 = 0.92$ m/min is in the measured range of 0.80 to 1.24 m/min as reported also by Nelson et al. Experimental data for the rate of air flow in the Wemco-0.8m^3 model are needed for validation of CFD results.

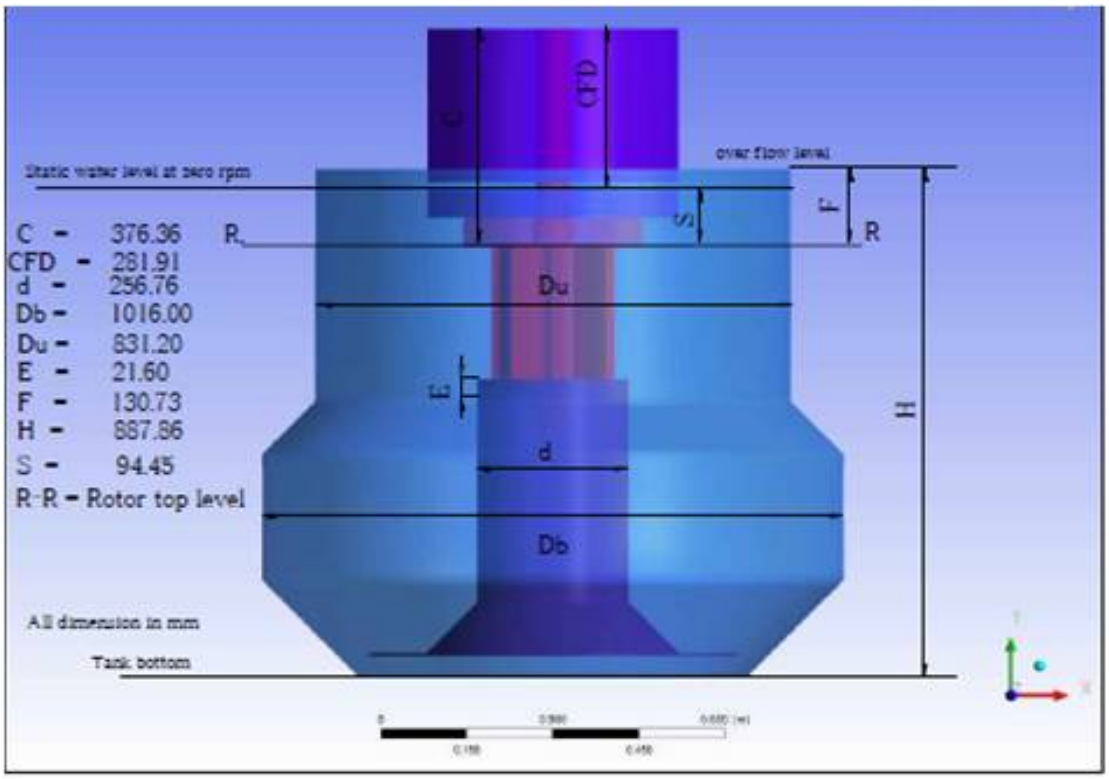

C : canister top level from the rotor top
CFD: static water level at zero rpm from the canister top
d : draft tube diameter
Db: Tank bottom diameter
Du: upper tank diameter
E : engagement distance
F : overflow level from the rotor top
H : Tank height
S : rotor submergence

Figure 5.4: Wemco-0.8m^3 initial water level

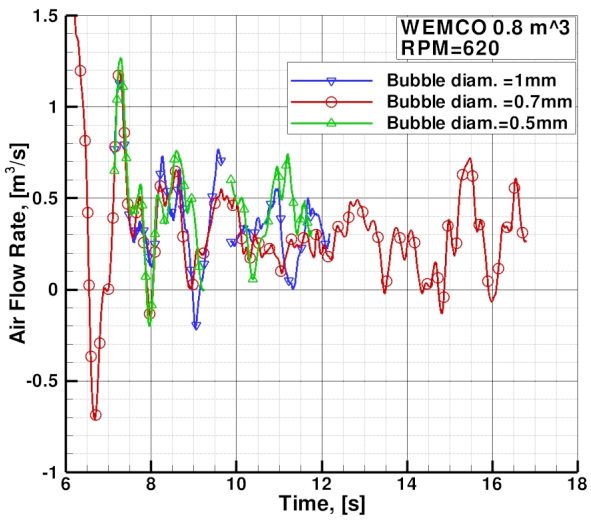

(a) Variation of air volume flow rate with time

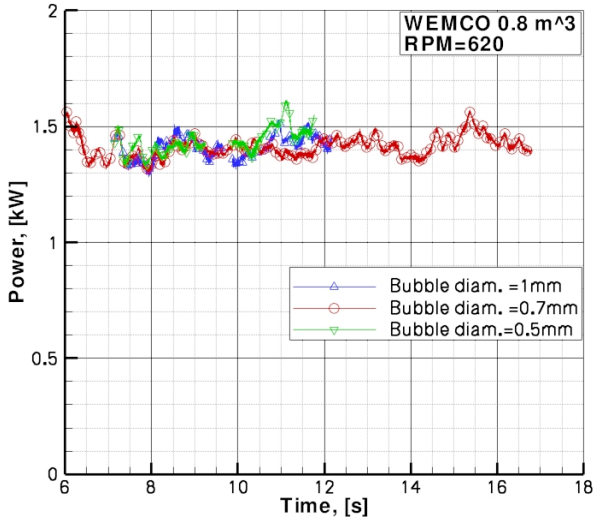

(b) Variation of power with time

Figure 5.5: Effects of assumed bubble diameter on air flow rate and power, $d_b = 0.5,\ ,0.7$ and 1.0 mm

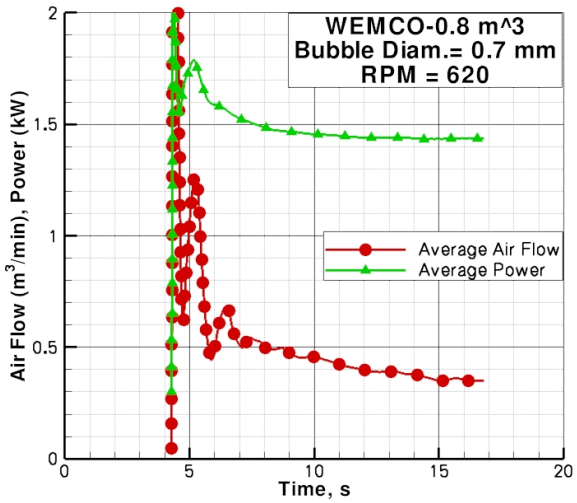

Figure 5.6: Running average of air flow rate and power

5.5.3 Flow Pattern and Velocity Field

The flow pattern in the Wemco rotor is very complex and unsteady. Analysis of the velocity field and air volume fraction in the rotor region will shed light on the principle of the Wemco machine operation. Air volume fraction contours in horizontal planes that cut the rotor blades are shown in Figures 5.7a-5.7f. In these figures, the blades rotate counter-clockwise. At this instant of time ($t = 14.35$s) the rate of air flow is minimum and the water volume in rotor is also minimum. Figure 5.7a is for a plane just below the rotor, and it shows that negligible air penetrates down to the draft tube. No air recirculates from the tank into the draft tube. Air accumulates on the blade suction side whereas water covers most of the pressure sides. Figure 5.7b shows that as water enters the rotor from the draft tube there is blade-to-blade periodicity, but very quickly asymmetry develops with height as can be seen in planes of higher elevation; Figures 5.7c-5.7e. The air bucket cross-sectional area within the rotor increases with elevation. Each pair of diametrically opposite blades have similar distributions. The asymmetry is due to interference between the wake of one blade with the flowing blade. This interference may be triggered by many sources such as the disperser having 17 holes which breaks circumferential symmetry for the six-blade rotor. Also, there is one air inlet at a particular circumferential angle. Lack of flow periodicity in the Wemco rotor has also been predicted by CFD simulations of single-phase flow in Wemco 250 and 300 conducted by Salem-Said and Ragab (unpublished work).

Water superficial vertical and radial velocity contours on the same horizontal planes are depicted in Figures 5.8a-5.8f and 5.9a-5.9f, respectively. In Figure 5.9c, we see that the two blades at positions twelve-O'clock and six-O'clock have the strongest radial outflow, whereas the two blades in the positions four-O'clock and ten-O'clock have inward radial flow. The radial inward flow is entrained by the rotor from the secondary flow below the disperser. The pumping situation switches at higher elevation as shown in Figure 5.9e. Here, the radial flow at the blades at twelve-O'clock and six-O'clock is blocked whereas that at the blades at four-O'clock and ten-O'clock is strong and outward. Hence, water exits the rotor non-uniformly both circumferentially and vertically.

Air volume fraction and water superficial vertical and radial velocity contours on the same horizontal planes at another instant of time ($t = 15.4$ s) are depicted in Figures 5.10a-5.10f, 5.11a-5.11f and 5.12a-5.12f, respectively. At this instant, the air flow rate is maximum and the water content in the rotor is also maximum. The important qualitative difference in the flow at this instant of time and the earlier one is the change in the direction of the vertical velocity at the rotor top as shown in Figures 5.8f and 5.11f. Water flows from the rotor into the standpipe mainly through the gap between rotor and disperser, and then falls down back from the standpipe mixed with air. The tips of rotor blades then pump this mixture through the upper row of disperser holes to the tank.

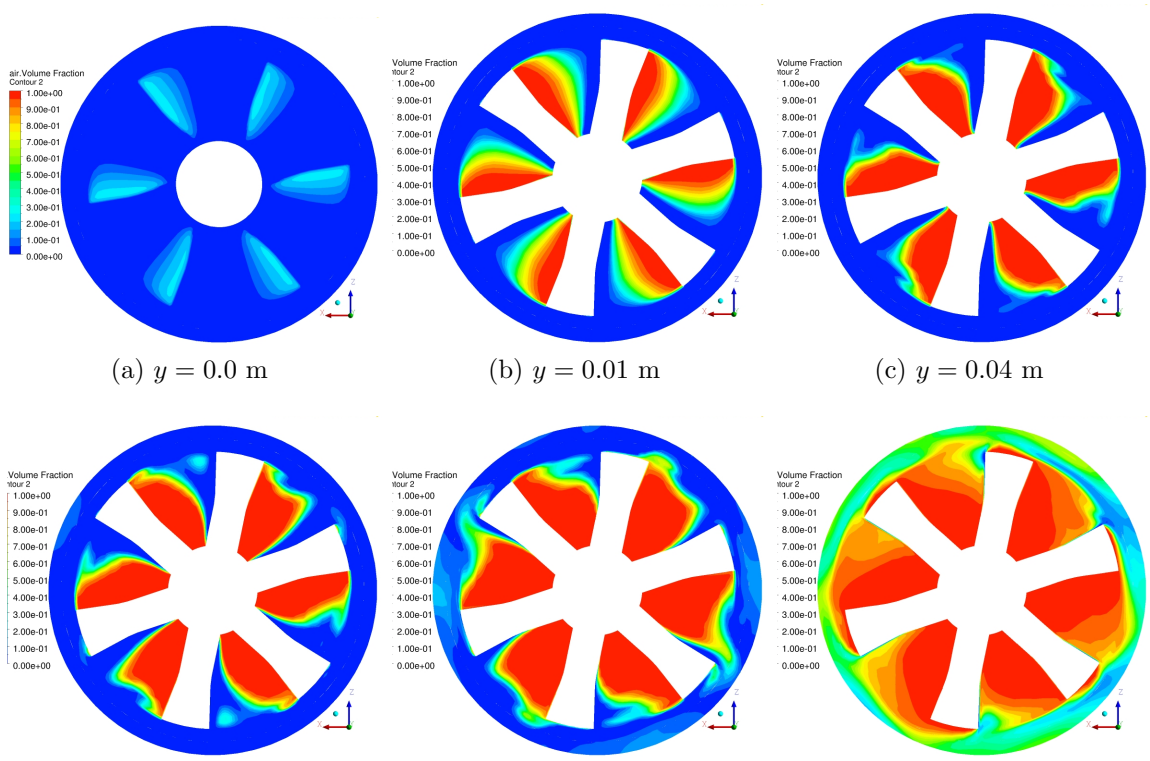

(a) $y = 0.0$ m (b) $y = 0.01$ m (c) $y = 0.04$ m

(d) $y = 0.06$ m (e) $y = 0.10$ m (f) $y = 0.24$ m

Figure 5.7: Air volume fraction contours in horizontal planes cutting rotor blades, $t = 14.35$s. Plane elevation y is measured from the rotor bottom.

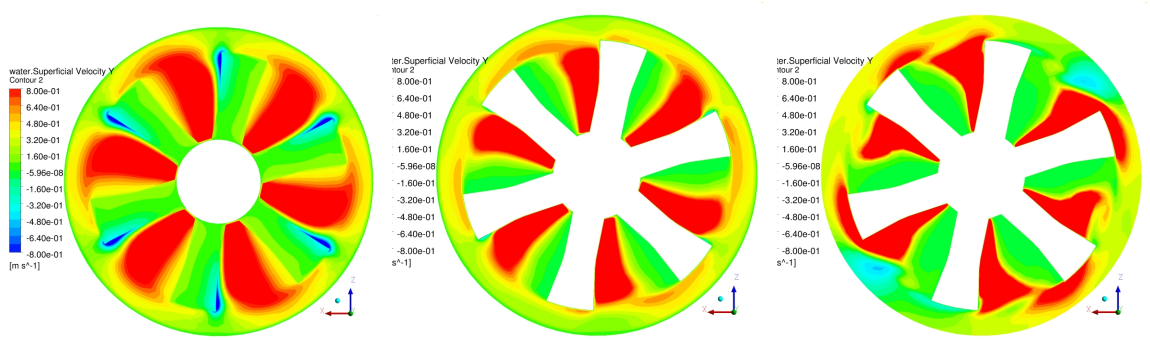

(a) $y = 0.0$ m (b) $y = 0.01$ m (c) $y = 0.04$ m

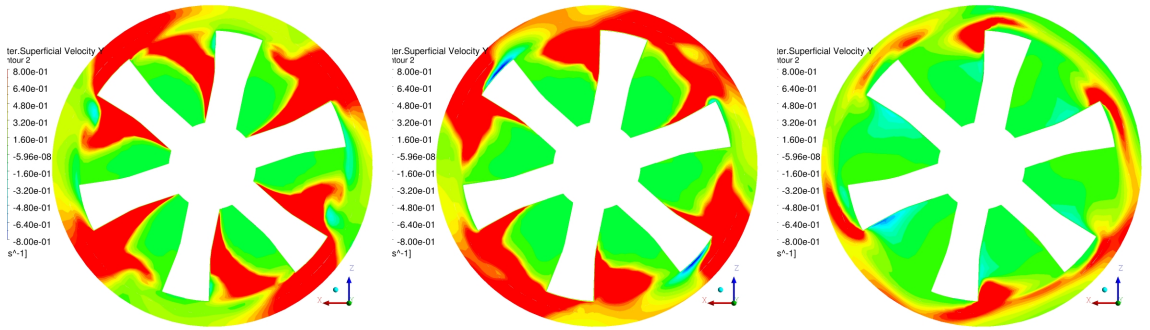

(d) $y = 0.06$ m (e) $y = 0.10$ m (f) $y = 0.24$ m

Figure 5.8: Water superficial vertical velocity contours in horizontal planes cutting rotor blades, $t = 14.35$s. Plane elevation y is measured from the rotor bottom.

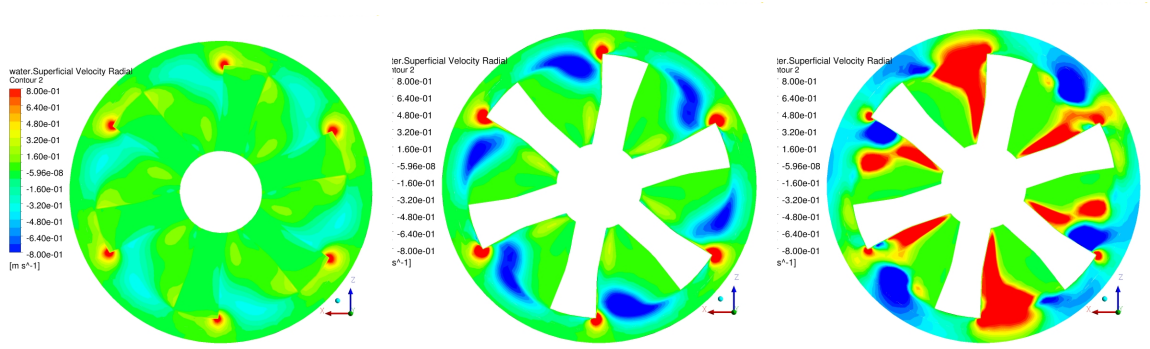

(a) $y = 0.0$ m (b) $y = 0.01$ m (c) $y = 0.04$ m

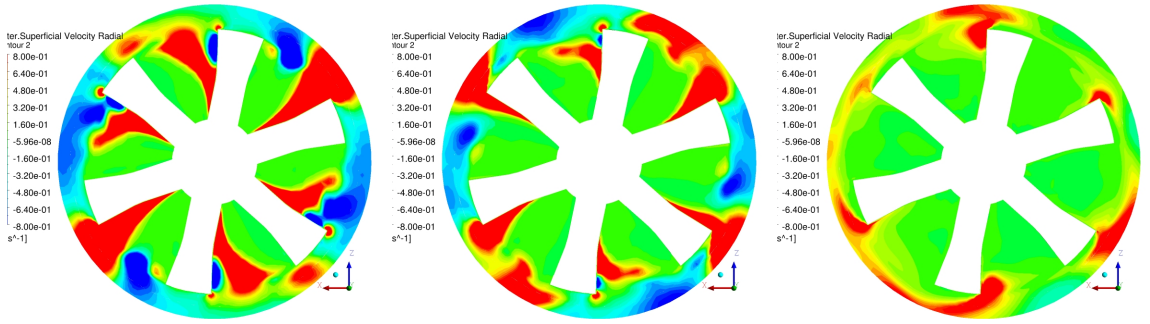

(d) $y = 0.06$ m (e) $y = 0.10$ m (f) $y = 0.24$ m

Figure 5.9: Water superficial radial velocity contours in horizontal planes cutting rotor blades, $t = 14.35$s. Plane elevation y is measured from the rotor bottom.

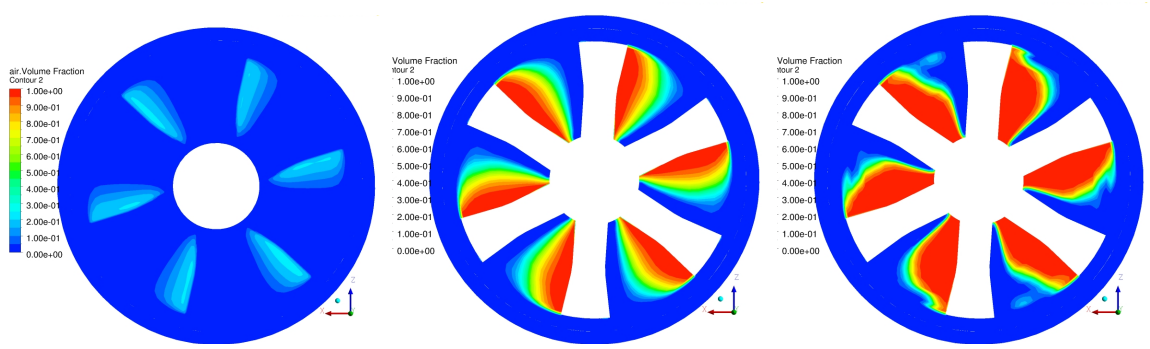

(a) $y = 0.0$ m (b) $y = 0.01$ m (c) $y = 0.04$ m

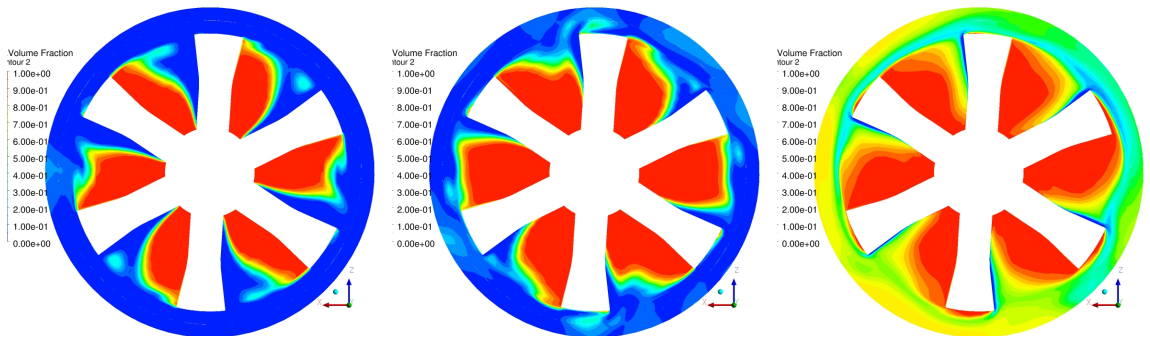

(d) $y = 0.06$ m (e) $y = 0.10$ m (f) $y = 0.24$ m

Figure 5.10: Air volume fraction contours in horizontal planes cutting rotor blades, $t = 15.4$s. Plane elevation y is measured from the rotor bottom.

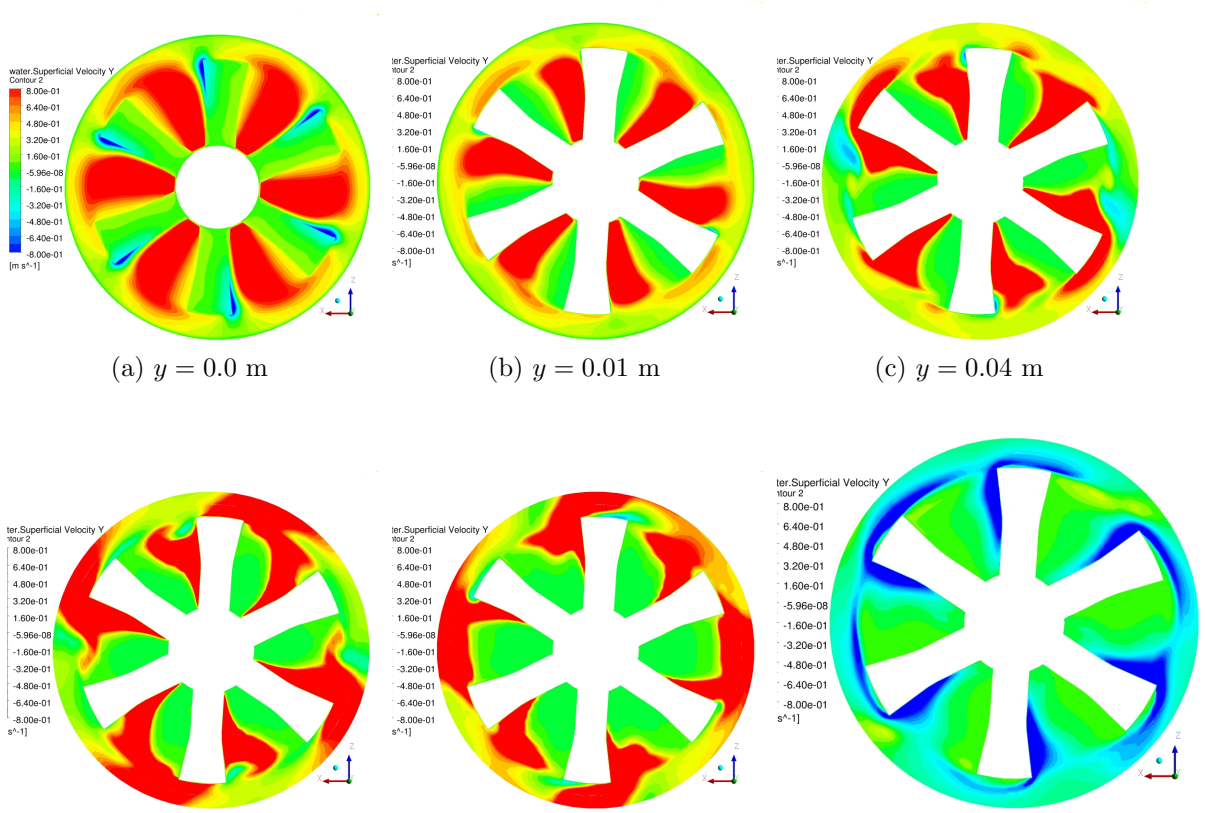

(a) $y = 0.0$ m (b) $y = 0.01$ m (c) $y = 0.04$ m

(d) $y = 0.06$ m (e) $y = 0.10$ m (f) $y = 0.24$ m

Figure 5.11: Water superficial vertical velocity contours in horizontal planes cutting rotor blades, $t = 15.4$s. Plane elevation y is measured from the rotor bottom.

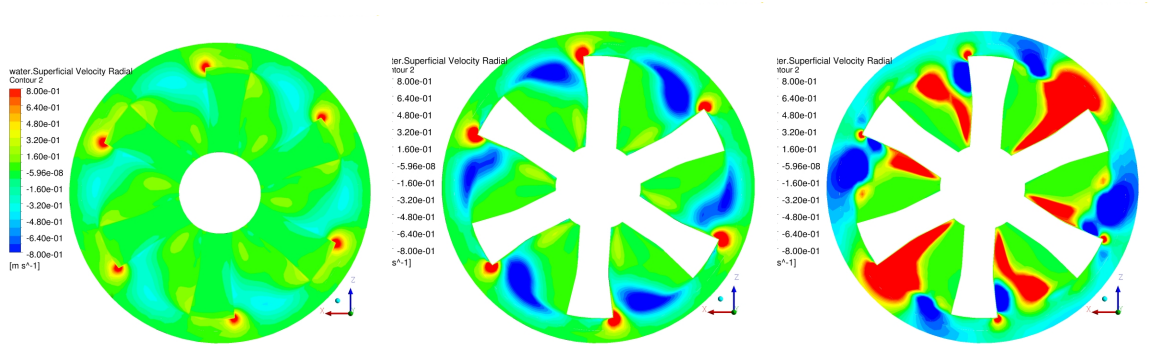

(a) $y = 0.0$ m (b) $y = 0.01$ m (c) $y = 0.04$ m

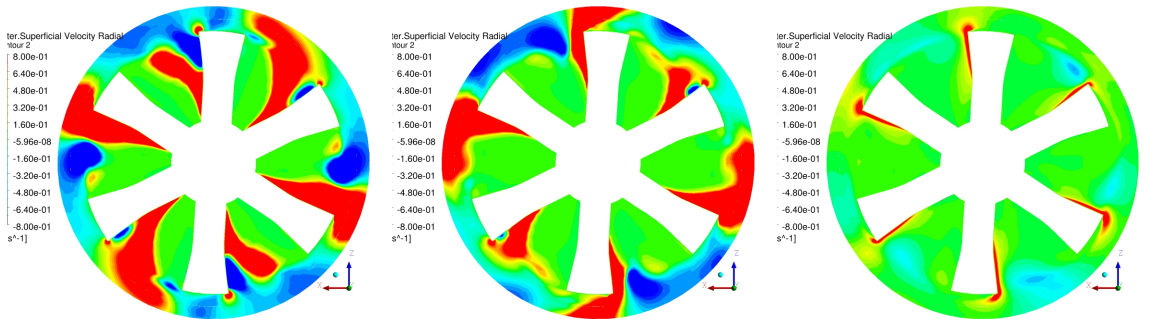

(d) $y = 0.06$ m (e) $y = 0.10$ m (f) $y = 0.24$ m

Figure 5.12: Water superficial radial velocity contours in horizontal planes cutting rotor blades, $t = 15.4$s. Plane elevation y is measured from the rotor bottom

Figures 5.13a-5.13b show the air volume fraction in a vertical mid plane that passes through the axis of the machine at two different times where the air flow rate is minimum and maximum, respectively. A vortex is formed in the standpipe, and water adheres to the standpipe walls under the effects of centrifugal forces (i.e. water flows up into the standpipe with high circumferential velocity component). Consequently, water head in the standpipe increases continuously until it reaches its maximum level. At this instant water breaks away from the standpipe walls and falls under gravity to the rotor tips capturing air with it as a mixture as depicted in figure 5.13d. Water superficial radial velocity component does not change significantly with time as shown in figures 5.13e-5.13f. Secondary flow is observed under the disperser that allows water to circulate from the tank to the rotor region. It makes the flow very weak in the lower half of the tank as the velocity vectors show in figures 5.14a-5.14b. These figures also show that jets issue only from the upper row of the disperser holes, while the lower row of holes are inactive. Jets out of disperser are nearly horizontal.

The secondary flow represents about 50 % of the total pumping capacity coming out from the disperser holes. The effects of the secondary flow on the recovery rate is unknown. However, the results points to possible design modifications of the Wemco machines. The effects of parameters such as the standpipe to rotor diameter ratio, disperser to rotor diameter ratio and disperser to standpipe diameter ratio need to be investigated. Also, the submergence depth of the rotor inside the draft tube may have great effect on the pumping capacity of the rotor. These parameters can be optimized to enhance performance of the Wemco cells.

Figures 5.15a-5.15b depict the water axial and circumferential velocity profiles in the draft tube in a plane $y = 0.16$ m below rotor bottom. The water velocity vectors projected on that plane are shown in Figure 5.15c. Velocity profiles show small variations of the water velocities in draft tube at the two different extremes of the air flow rate. As mentioned earlier maximum air flow rate thought the machine is obtained when the water volume in rotor is maximum. Water velocities in draft tube respond to variations of the water volume between the rotor passages. An axial vortex has been predicted in the draft tube as shown in figure 5.15c due to very small vorticity in the tank. This means that the disperser did not completely suppress the circumferential velocity component of water jets from the rotor. Part of the angular momentum imparted by the rotor to the water is preserved until the water flows back into the draft tube and that angular momentum appears as an axial vortex.

Figure 5.16 shows a snapshot of an iso-surface of air volume fraction equal to 0.25 through the whole machine. This surface in the standpipe is almost conical due to the combined effects of gravity and centrifugal acceleration. The surface deforms as it rotates continuously in time. The lower edge of this conical surface is attached to the rotor tip. Jets of air and water mixture exit the disperser holes and impinge on the tank walls. The jets split into two streams, one rises to the tank top the other moves into the lower tank. All air eventually rises to the overflow tank due to buoyancy.

In the present simulations, dispersion of air through the tank is highly affected by two main

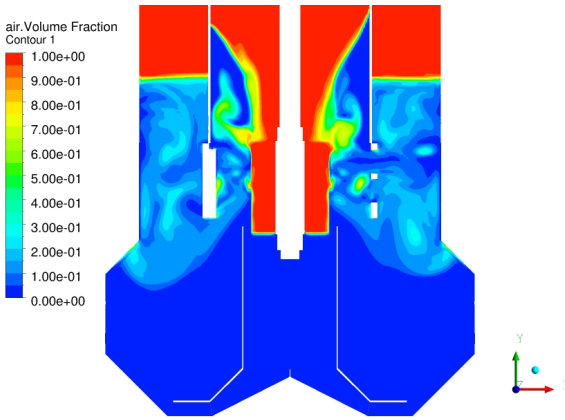

(a) Air volume fraction, $t = 14.35$ s

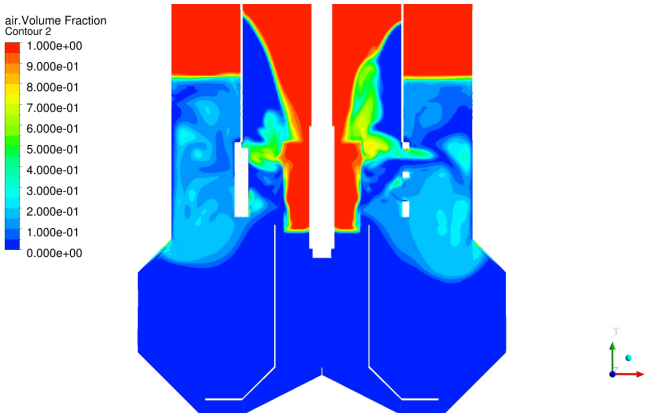

(b) Air volume fraction, $t = 15.4$ s

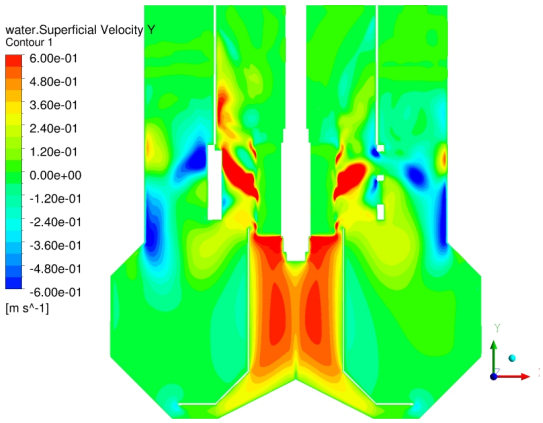

(c) Water superficial vertical velocity, $t = 14.35$ s

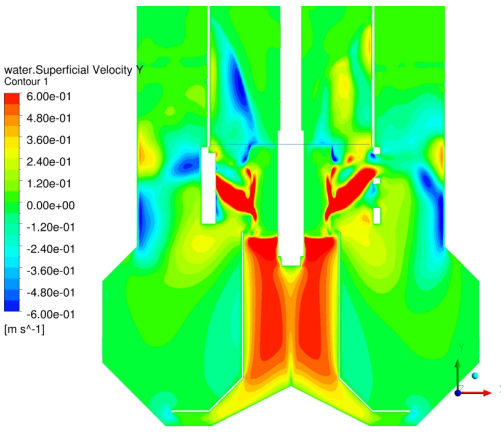

(d) Water superficial vertical velocity, $t = 15.4$ s

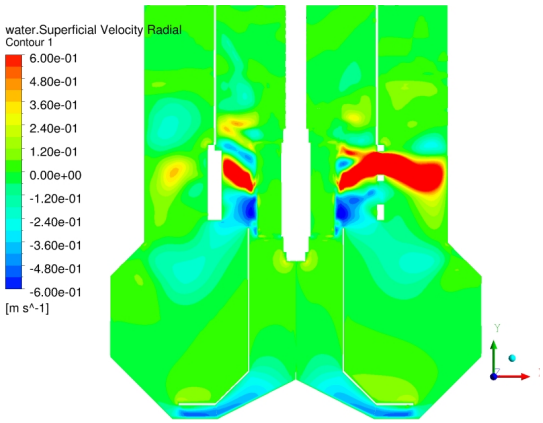

(e) Water superficial radial velocity, $t = 14.35$ s

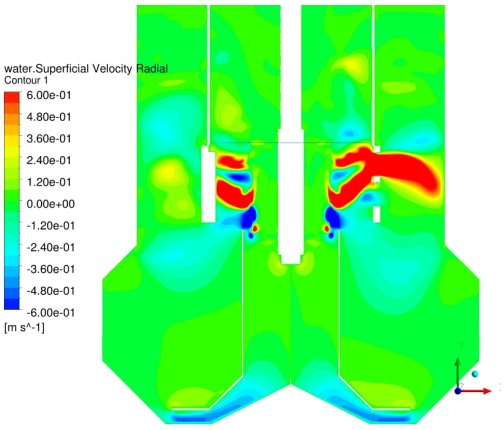

(f) Water superficial radial velocity, $t = 15.4$ s

Figure 5.13: Air volume fraction and water superficial velocity contours at times $t = 14.35$ and 15.5 s

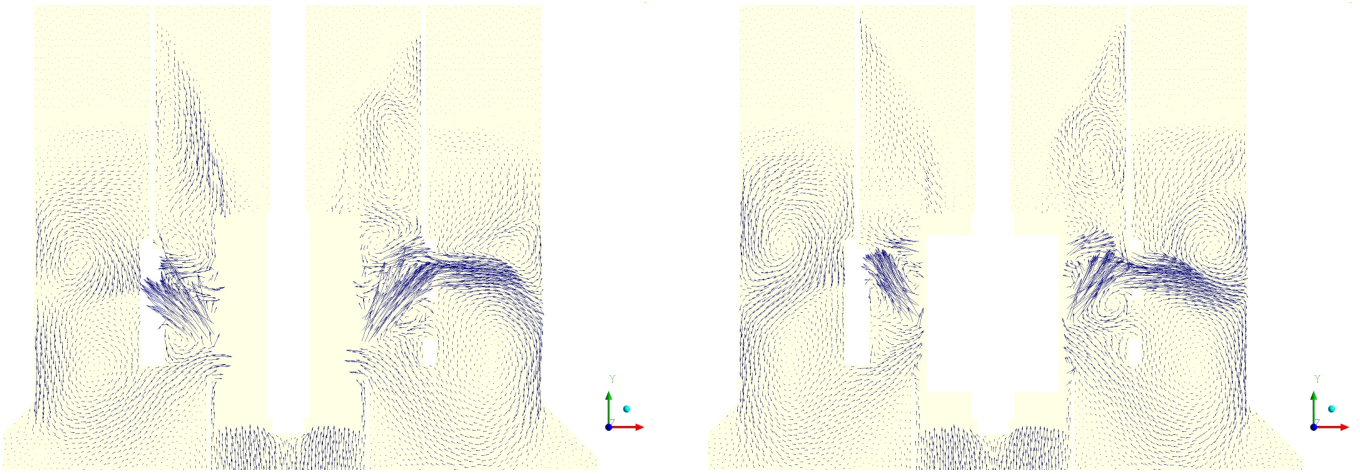

(a) Water superficial velocity vectors at maximum rate of air flow

(b) Water superficial velocity vectors at minimum rate of air flow

Figure 5.14: Water superficial velocity vectors in a vertical plane passing through rotor axis at maximum and minimum air flow rates

forces, drag and buoyancy. Drag on a spherical bubble is proportional to the square of the diameter while buoyancy is proportional to the cube of the diameter. Accordingly, bubble diameter has a significant effect on the spatial distribution of air volume fraction through the Wemco 0.8m^3 as depicted in Figures 5.17a-5.17c. For the small bubble diameter of 0.5 mm, air is well dispersed in the tank region and penetrates deeper into the lower tank in comparison with larger bubble diameters. The air holdup is defined by

$$\epsilon_g = \frac{1}{V_w} \int_{V_w} \alpha dV_w \tag{5.21}$$

where V_w is the total pulp volume below the initial water level.

The air holdup is 9.3%, 7.4%, and 5.7% for the three bubble diameters 0.5, 0.7, and 1. mm, respectively. The increase of air holdup with the decrease in the bubble diameter is anticipated because bubbles of small diameter are more responsive to the drag than buoyancy forces. This means that these small bubbles take longer time (i.e. retention time) to escape out at the free surface of the pulp. As long as the retention time of the bubbles increases, more air will build up in the pulp phase.

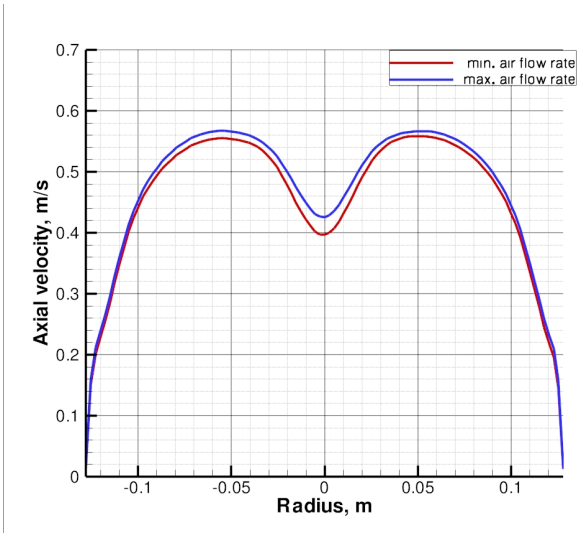

(a) Water axial velocity profiles in draft tube

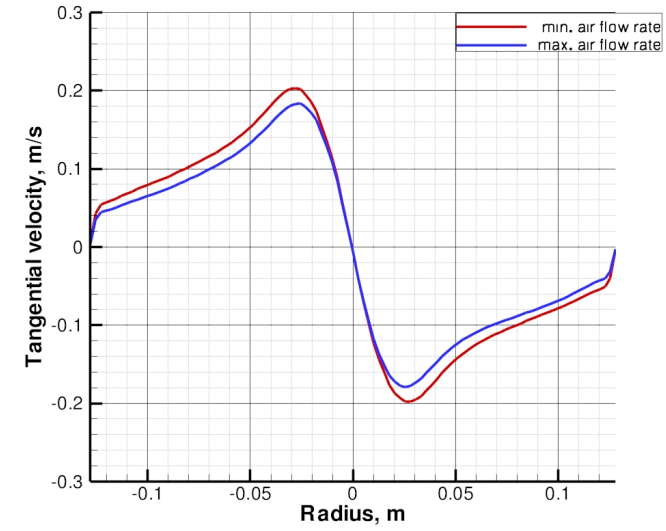

(b) Water circumferential velocity profiles in draft tube

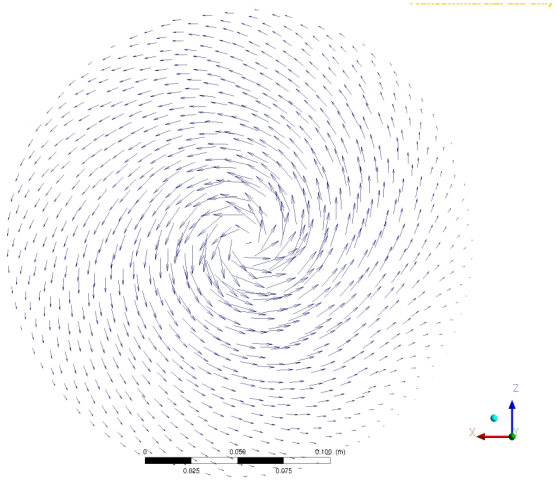

(c) Water circumferential velocity vectors in draft tube

Figure 5.15: Water superficial axial and circumferential velocities in draft tube

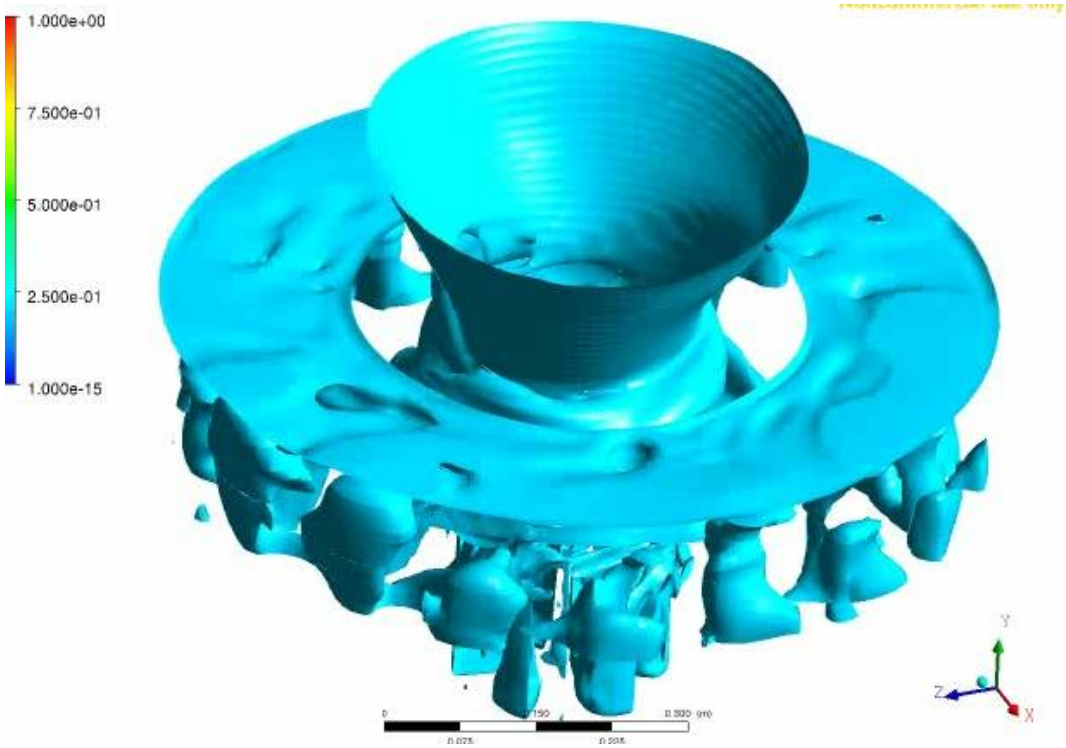

Figure 5.16: Iso-surface of 25% air volume fraction

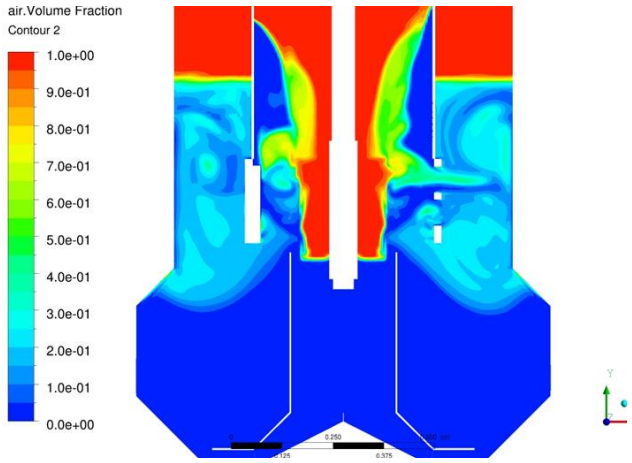

(a) Air volume fraction for bubble diameter 0.5mm

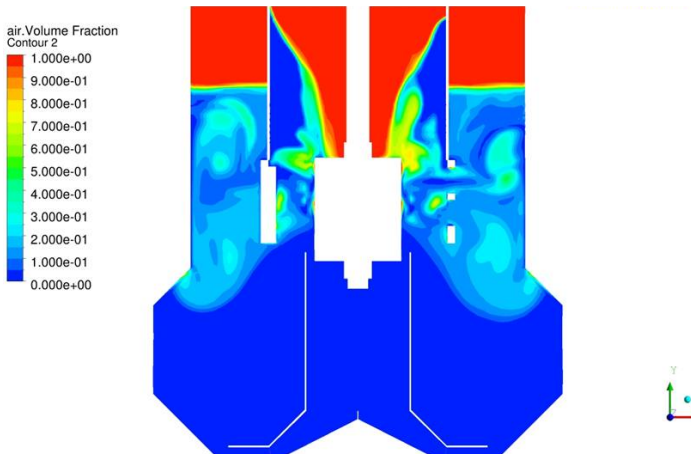

(b) Air volume fraction for bubble diameter 0.7mm

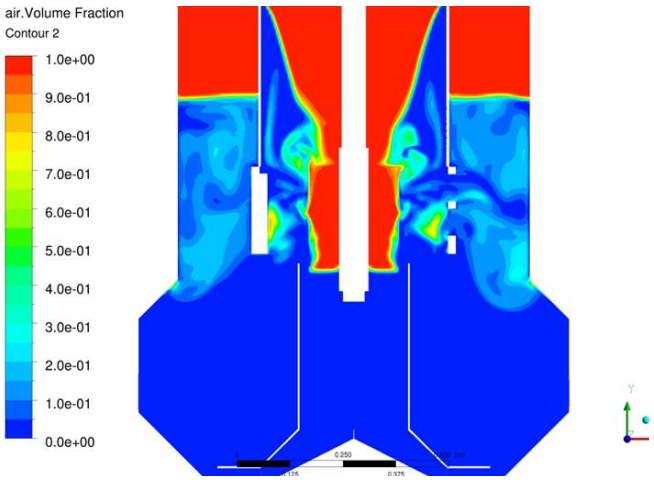

(c) Air volume fraction for bubble diameter 1.0mm

Figure 5.17: Effects of assumed bubble diameter on air volume fraction, $d_b = 0.5,\ , 0.7$ and 1.0 mm

5.6 Application of CFD-Based Flotation Model

In this section, we demonstrate the viability of CFD-based flotation model as a tool to evaluate the performance of flotation machines and provide detailed hydrodynamic and kinetics data that can help improve the design of such machines. Ragab and Fayed [50] have developed a CFD-based flotation model, and used it to determine the effects of particle diameter d_p, particle specific gravity γ_p, contact angle θ, and surface tension σ on the recovery rate constant at any locality within the pulp. Spatial distributions of dissipation rate, ϵ, and air volume fraction, α (also called void fraction), are determined by the two-phase hydrodynamic simulations. The number concentration of bubbles is $n_{bT} = \alpha/v_b$, where v_b is the bubble volume, and spherical bubbles are assumed. The particles-bubbles collisions kernel is given Abrahamson-Schubert [58] model (see Section 2.2.2). In this dissertation, the particles-bubbles collisions kernel by Zaichik et al. [79] (see Section 2.2.4) is implemented into CFD-based flotation model as post processing programs that can be used to compute recovery rate in the pulp of Wemco 0.8m^3. The recovery rates are compared to those using Abrahamson-Schubert model [58]. The two-phase simulations in the Wemco 0.8m^3 cell obtained by Fayed and Ragab [21] have also been used here to provide the spatial distribution of the air volume fraction, α, the dissipation rate, ϵ, and the velocity fluctuation, u', which is estimated from the local eddy viscosity and dissipation rate. The probabilities of collision, adhesion, and stabilization have been presented in [50] and will not be repeated here.

Collisions of bubbles of diameter 0.7 mm with particles of diameter in the range 10μm to 300μm are relevant to flotation machines. Comparisons between the recommended Zaichik et al. [79] model and Abrahamson-Schubert [58] model, a model that is often used in flotation kinetics, for turbulence and particle sizes of interest to mineral flotation are shown in Figures 5.18a and 5.18b for particle specific gravity of 4.1 and 2.0, respectively. Three levels of dissipation (ϵ = 1; 10, and 100W/kg) are considered. Overall, for particle diameter less than 100μm, Abrahamson-Schubert model overestimates the mean radial relative velocity of particles and bubbles at collision and hence the collisions frequency is overpredicted. It is also observed that the radial velocity predicted by Abrahamson-Schubert [58] model increases very rapidly at large particle sizes while that of Zaichik et al. [79] model seems to level off at large particles sizes. Figures 5.19a-5.20d show a comparison between Abrahamson-Schubert and Zaichik-2010 model for the collisions kernel in Wemco 0.8m^3 at 20μm and 100μm particle diameter. High turbulent dissipation has a favorable effects on the collisions kernel. It is observed that high collisions kernel exists in the region between rotor and stator where the highest levels of turbulent dissipation rates exist. Small particles ($d_p < 50\mu$m) collisions with bubbles occur on the rotor tip where the highest dissipation rate exists in these regions. The analysis of this model reveals the fact that high turbulent dissipation rate is needed to float very fine particles $d_p < 50\mu$m. However, high turbulent dissipation rates have an adverse effects on the attachment and stabilization of particles-bubbles aggregates. It is evident from these figures that the collisions kernel, hence frequency, estimated by Abrahamson-Schubert model [58] is much greater than that according to Zaichik et al. [79] model, particularly

in the rotor region. This conclusion is true for the practical range of particle diameters of interest for flotation.

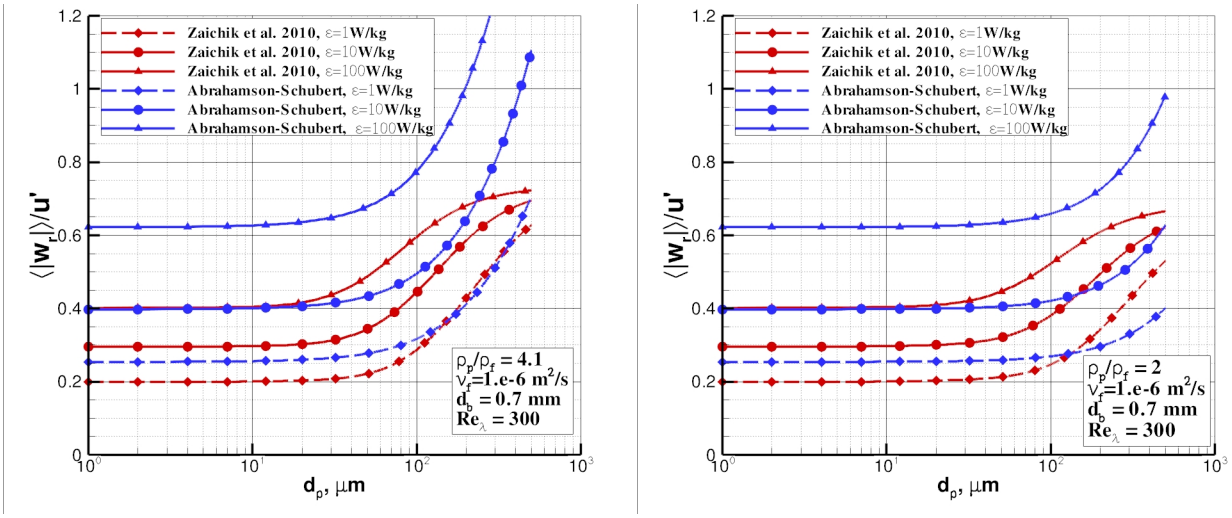

(a) $\rho_p = 4100 kg/m^3$ (b) $\rho_p = 2000 kg/m^3$

Figure 5.18: Comparison between Zaitchik et al. [79] model and Abrahamson-Schubert [58] model for particle-bubble radial relative velocity

We fix the parameters $\gamma_p = 4.1$, $\theta = 50^o$ degrees, $\sigma = 0.06$ N/m, and bubble diameter $d_b = 0.7$ mm. These parameters are required to calculate the local probabilities of attachment, collision and stabilization. We introduce a new definition of rate constant by:

$$k_1^* = k_1 \frac{\alpha}{v_b}(1-\alpha) \tag{5.22}$$

We recognize the factor α/v_b as the local number concentration of bubbles. The local number concentration of particles n_p is unknown, but we expect it to be proportional to the local water void fraction, $(1-\alpha)$. We believe that including the factor $(1-\alpha)$ gives a better figure of merit that be used to evaluate different designs in the absence of n_p distribution. Local distribution of k_1^* based on Abrahamson-Schubert and Zaichik models are depicted in Figures 5.21a- 5.21d. Despite the remarkable differences between the two collisions models, Abrahamson-Schubert and Zaichik-2010, the differences in the local values of k_1^* is not that much. The reason for that is very low probabilities of attachment exist in the regions where large differences between the the two collisions models exist.

We define an average pulp pseudo rate constant by

$$R = \frac{R_f}{V}\int_V k_1^*(1-b)dV \tag{5.23}$$

where R_f is a froth recovery factor. We assumed $R_f = 1$ and $b = 0$. The pseudo rate constants shown in these figures are very high relative to experimental data reported in

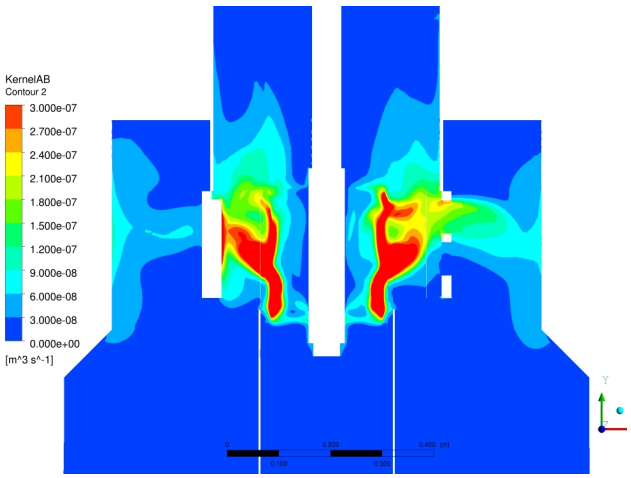

(a) Vertical plane. Abrahamson-Schubert Model

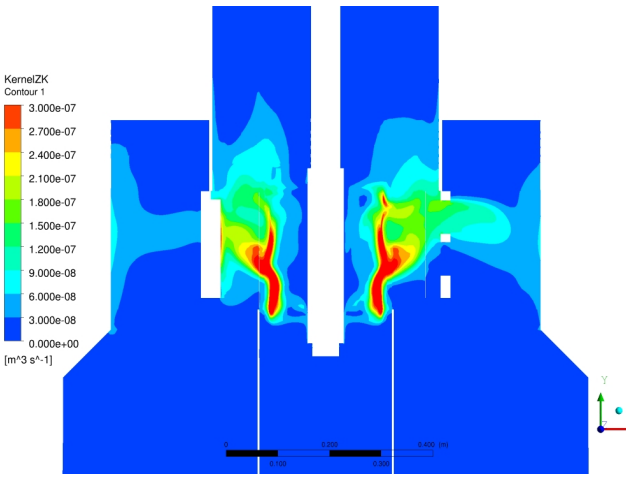

(b) Vertical plane. Zaichik-2010 Model

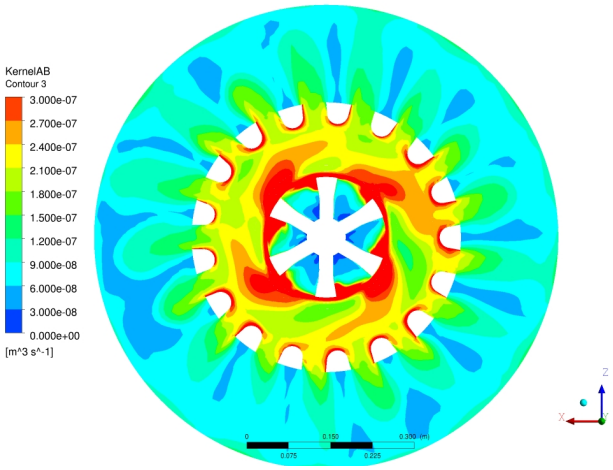

(c) Horizontal plane. Abrahamson-Schubert Model

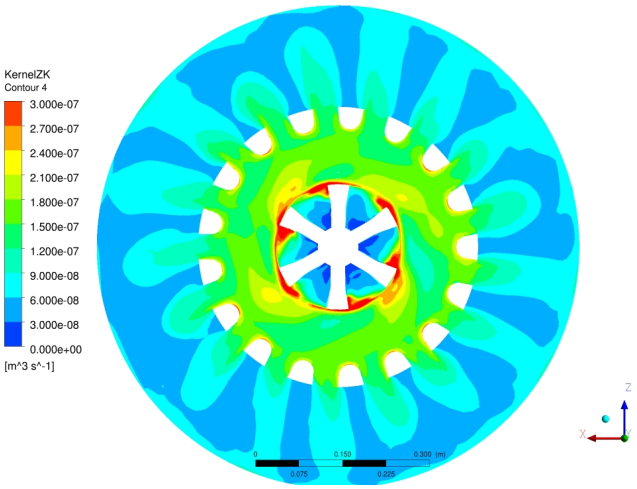

(d) Horizontal plane plane. Zaichik-2010 Model

Figure 5.19: Collision kernel. Comparison of Zaichik et al. [79] and Abrahamson-Schubert [58] models. Bubble diameter $d_b = 0.7$ mm, particle diameter $d_p = 20\mu$m.

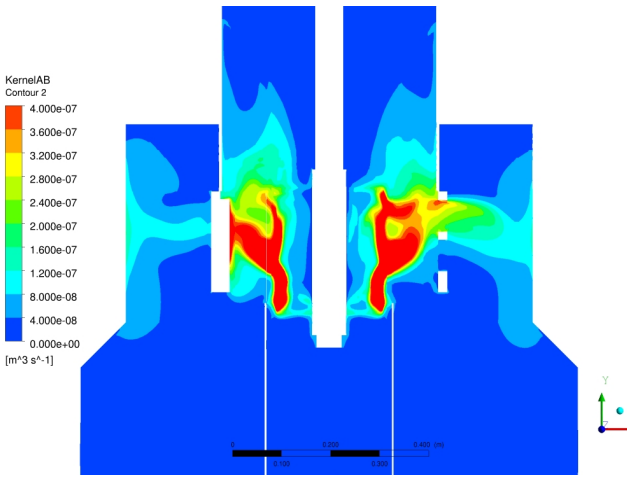

(a) Vertical plane. Abrahamson-Schubert Model

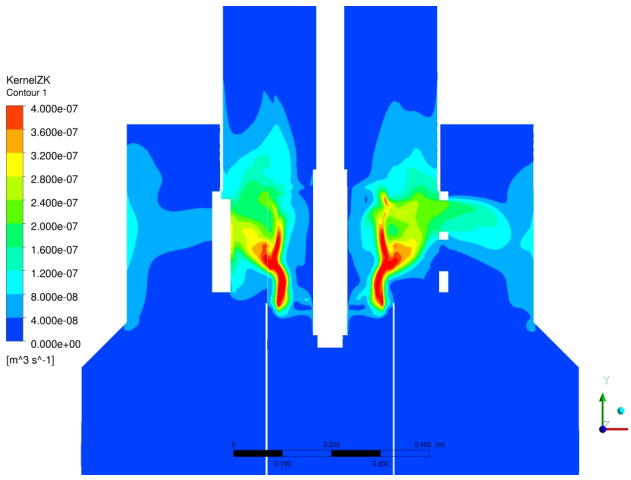

(b) Vertical plane. Zaichik-2010 Model

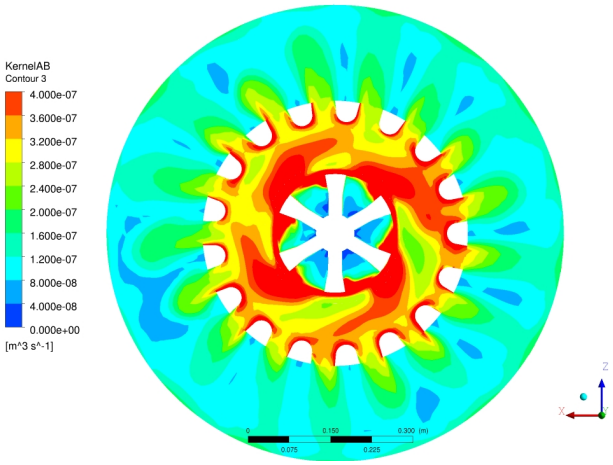

(c) Horizontal plane. Abrahamson-Schubert Model

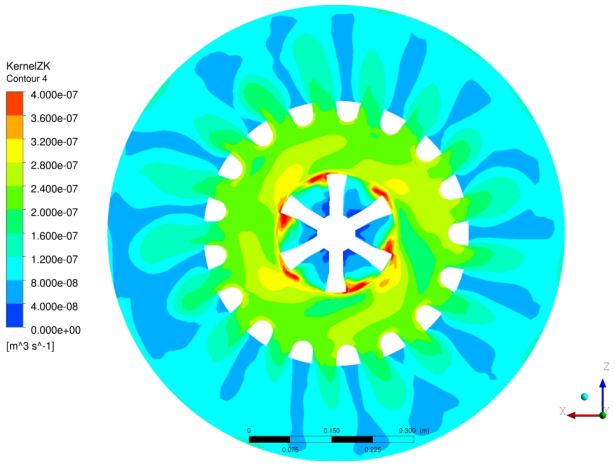

(d) Horizontal plane plane. Zaichik-2010 Model

Figure 5.20: Collisions kernel. Comparison of Zaichik et al. [79] and Abrahmson-Schubert [58] models. Bubble diameter $d_b = 0.7$mm, particle diameter $d_p = 100\mu$m.

literature because of the assumed values of R_f and b and the assumption of uniform bubble size.

In the present work, the pseudo rate constant is computed as a function of particle diameter. The comparison between the two models is shown in Fig(5.22). The pulp rate predicted by using Abrahamson-Schubert [58] model is slightly higher than that of Zaichik et al. [79] model. Although the collision frequency according to Abrahamson-Schubert model is much higher than that of Zaichik-2010 model, the net effect on the pseudo rate constant is a modest increase. This is because regions of higher collision rate are also associated with very low probability of stabilization. Nevertheless, the Zaichik-2010 model assessed in this study is more reliable than Abrahamson-Schubert model.

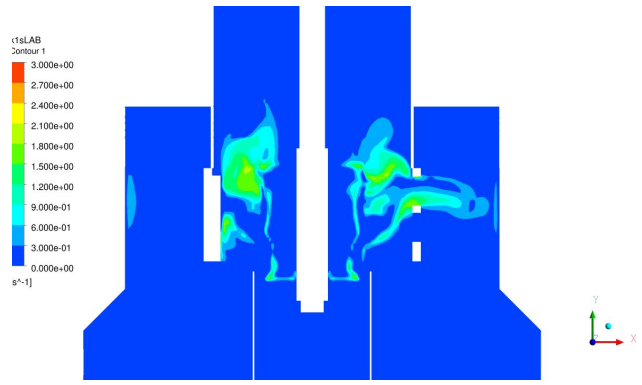

(a) Pseudo rate constant k_1^* for 20 μm particle diameter based on Abrahamson-Schubert Model

(b) Pseudo rate constant k_1^* for 20 μm particle diameter based on Zaichik-2010 model

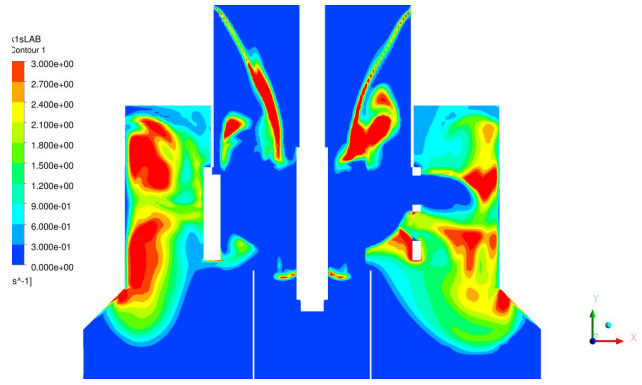

(c) Pseudo rate constant k_1^* for 100 μm particle diameter based on Abrahamson-Schubert Model

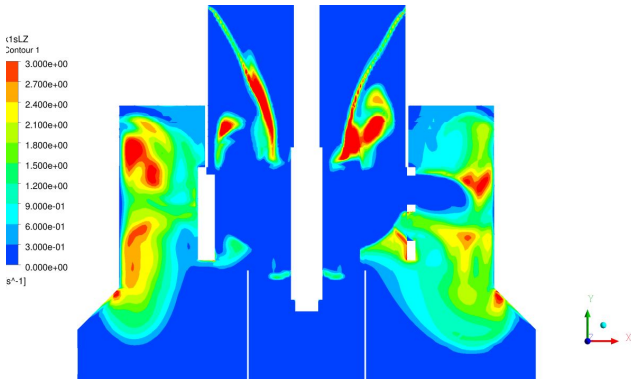

(d) Pseudo rate constant k_1^* for 100 μm particle diameter based on Zaichik-2010 model

Figure 5.21: Pseudo rate constant $k_1^* = k_1\alpha(1-\alpha)/v_b$ for 0.7 mm bubble diameter in WEMCO 0.8

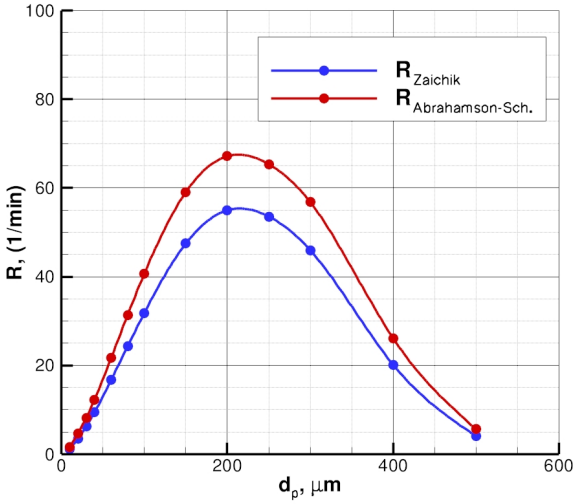

Figure 5.22: Average pseudo rate constant R for 0.7mm bubble diameter in Wemco 0.8m^3. Comparison of Zaichik et al. [79] and Abrahamson-Schubert [58] models.

Chapter 6

Numerical Simulations of Two-Phase Flow in a Dorr-Oliver Flotation Cell Model

[1]

Abstract

Two-phase (water and air) flow in the forced-air mechanically-stirred Dorr-Oliver machine has been investigated using computational fluid dynamics (CFD). A 6 m3 model is considered. The flow is modeled by the Euler-Euler approach, and transport equations are solved using software ANSYS-CFX5. Unsteady simulations are conducted in a 180-degree sector with periodic boundary conditions. Air is injected into the rotor at the rate of 2.63 m3/min, and a uniform bubble diameter is specified. The effects of bubble diameter on velocity field and air volume fraction are determined by conducting simulations for three diameters of 0.5, 1.0, and 2.0 mm. Air volume fraction contours, velocity profiles, and turbulent kinetic energy profiles in different parts of the machine are presented and discussed. Results have been compared to experimental data, and good agreement is obtained for the mean velocity and turbulent kinetic energy profiles in the rotor-stator gap and in the jet region outside

[1]This chapter is based on a paper coauthored by Dr. Abdel Halim Salem-Said and Dr. Saad Ragab [56]. Dr.Abdel Halim generated the grid, obtained results for single phase flow and preliminary results of two-phase flow. The present author obtained final results for the two-phase simulations and compared CFD results with two-phase flow experimental data

stator blades.

6.1 Introduction

The hydrodynamics of froth flotation machines controls the grade and rate of recovery achievable in such machines. The complexity of three phase turbulent flow prevalent in those machines defies intuition, and a more scientific approach is needed to understand and control the multiplicity of physicochemical processes responsible for froth flotation. Computational fluid dynamics (CFD) is a powerful methodology that can provide detailed flow field properties such as mean velocity, turbulence intensity, dissipation rate, spatial distribution of air volume fraction (void fraction), bubble size distribution, and bubble-particle collision rate. All of these properties are needed to build simulation models that can be used to predict the grade and rate of recovery. They also help the designer to understand the flow patterns and their impact on flotation processes and to recommend design changes for performance optimization. Furthermore, CFD can provide unsteady forces and moments for structural components (rotor blades, driving shaft, and stator/disperser) needed for assessing structural integrity (stress analysis and vibration), longevity of the machine, and power consumption. Ultimately, CFD is a viable tool to assess the performance of existing flotation cells and to help design the new generation of machines. In the past three years, the authors have used CFD and simulated single and two-phase flows in four well known flotation cells of scales varying from laboratory models to full scale machines [57], [21] and [50]. Two of the machines are forced-air machines, namely Dorr-Oliver and Xcell. The third machine is WEMCO cell, which is a self-aerated machine.

Numerical simulation of single phase flow has been conducted to study flow field in 'Metso Mineral' and 'Outokumpu' $0.8m^3$ cell [29]. A 3D grid of sizes 1.56×10^6 for 'Metso Mineral' and 1.46×10^6 for 'Outokumpu' were used to run the simulations. It illustrates an expensive computational cost especially when the flow inside these flotation cells is unsteady. Single phase simulations may be useful in the initial design stages by providing overall flow characteristics, but in reality, the two phase flow is more relevant to be simulated to determine regions of high void fractions and turbulent dissipation rate. For two-phase simulation, another computational cost is now added to the simulations of the single phase, where another set of transport equations for the gas phase needs to be solved. Some approaches have been used to reduce computational cost [66], where sector-based simulations were used to reduce the number of grid nodes. These simulations provide spatial distribution of turbulent parameters such as turbulent kinetic energy and its rate of dissipation, which are important to identify regions where particles-bubbles attachment and detachment occur [27], [27], [14] and [28]. One of the most important parameters in these simulations is the bubble size, which affects directly local void fraction and overall gas hold up in the cell. In real situations, there is no single bubble size but there is a size distribution, which is affected by the local shear and turbulence parameters. In CFD simulation another set of equations that describe particle size distribution "population balance model" can be implemented to predict the

bubble size distribution [26]. Of course, it will increase the computational cost because each size group will have its own set of equations. Another approach can be applied to avoid that much computational cost, where a parametric study can be conducted for different bubble size to investigate the effect of the bubble size on the flotation rate.

One of the main functions of mechanical flotation machines is to disperse air bubbles throughout the pulp volume. In order to assess the performance of flotation machines, it is important to know the spatial distribution of dispersed bubbles within the tank volume, which directly affects gas holdup. The current CFD simulations is a parametric study of two-phase flow to provide the hydrodynamic data and air volume fraction spatial distribution for a predetermined bubble size in the pulp phase in a Dorr-Oliver 6 m3 flotation cell. The results are presented first for a bubble size of 0.5 mm simulation then another two bubble sizes 1.0 and 2.0 mm are used to investigate the effects of the bubble size on the mean flow, turbulent kinetic energy and air volume fraction. Comparisons with experimental data for single and two phase flow are also presented to show that the unsteady Reynolds-Averaged Navier Stokes (RANS) model used in these simulations gives reliable results.

6.1.1 Euler-Euler Two-Fluid Model

Computational approaches for two phase flow may be classified largely into direct numerical simulation (DNS), Euler-Lagrange, and Euler-Euler models. In the DNS approach [47], [12], Navier-Stokes equations are solved for the local velocity and pressure for each phase. This approach is not practical for flotation machines simulations because of the large number of bubbles and high turbulent Reynolds number of the continuous phase. The Euler-Lagrange approach aims at modeling the carrier liquid phase by solving the Reynolds averaged Navier-Stokes equations and tracking bubbles by solving the equations of motion of each bubble as a point mass. Again, this approach is not practical essentially because of the large number of bubbles. The more practical approach is the Euler-Euler approach in which both phases are modeled by volume averaged equations [47]. The motion of the two continuous phases is described by its own RANS equations as the following:

Continuity Eq

$$\frac{\partial \alpha_i \rho_i}{\partial t} + \nabla \bullet (\alpha_i \rho_i \vec{V_i}) = 0 \tag{6.1}$$

Momentum Eq

$$\frac{\partial \alpha_i \rho_i \vec{V_i}}{\partial t} + \nabla \bullet (\alpha_i \rho_i \vec{V_i} \vec{V_i}) = -\alpha_i \nabla P + \nabla \bullet (\alpha_i \mu_{i,eff} (\vec{V_i} + (\vec{V_i})^T)) + S_i + M_i \tag{6.2}$$

where $i = 1$ denotes water phase and $i = 2$ denotes gas phase, ∇P is the modified pressure to include the gravity effects, S_i describes any external momentum source $S_i = 0$ and M_i is the

interfacial force on phase i due to the presence of other phases. Momentum exchange between the two phases due to drag and buoyancy on bubbles are the only mechanisms that couple the motion of the two phases. Bubbles are deformable fluid particles when moving in high shear rate regions such as in minerals flotation machines. Schiller-Naumann drag model [10] is used to predict the bubble drag coefficient. Schiller-Naumann drag model [10] neglects the effects of bubble deformation on drag coefficient. Turbulence transport is modeled by the shear stress transport (SST) turbulence model. A universal turbulence model for two-phase flow, particularly at high volume fraction, does not exist [12]. Perhaps the Reynolds stress model is the most adequate model for swirling flows, but it is computationally too demanding, and to the best of our knowledge, has never been applied to two-phase flow in flotation machines.

6.2 Computational Mesh and Boundary Conditions

The Dorr-Oliver machine is a mechanically agitated flotation cell. Two-phase (water and air) simulations are conducted for a $6m^3$ model of the machine. The overall dimensions of the model are shown in Figure 6.1. The machine is equipped with a $6 - blade$ rotor surrounded by a $16 - blade$ stator. Air is injected continuously into the rotor through six slots on the hub of the six passages of the rotor. Simulations are conducted for rotor speed of $250rpm$ ($N = 4.167rev/s$), maximum rotor diameter of $0.49m$, Reynolds number ($ND2/\nu$) of 1.0×10^6, and air volume rate Q $2.633m3/min$. These conditions give rotor tip speed U of $6.414m/s$ and average inlet air speed of $7.0m/s$. To investigate the effects of bubble diameter on gas hold up and other flow properties, separate simulations are performed for bubble diameters d_b of 0.5, 1.0, and $2.0mm$. The flow in a $180-degree$ sector is simulated by applying periodic boundary conditions. This choice of computational domain is dictated by the number of rotor blades of which there are six, and the number of stator blades of which there are 16. Therefore, the smallest circumferential sector that allows periodic boundary conditions must include three rotor blades and eight stator blades; that is half the machine.

A block-structured mesh is generated on half the machine using $1.2million$ nodes. The mesh in a vertical plane through the central axis is shown in Figure 6.2a, and a close-up of the surface mesh on the rotor and stator blades is shown in Figure 6.2b. Geometric details of the rotor and stator are very precisely represented by the geometric model. Fine grids are used near solid walls, particularly the leading edges of rotor blades in order to resolve tip vortices and high suction regions. The rotor is embedded in a rotating volume whose surface is a body of revolution. The impeller rotation is modeled by the Rotating Frame of Reference RFR approach because it correctly represents the unsteady interaction between the rotor and stator blades. The commonly used Multiple Frames of Reference MFR approach is inaccurate because the stator-rotor interaction is treated by the Frozen Rotor frame change model. All equations are advanced in time by using first-order implicit Euler method. The unsteady calculations have been performed on 8 parallel processors. The time step Δt is

equal to $0.002s$, and at $250rpm$, the impeller volume rotates $\Delta\theta$ equal to 3.0 degrees per time step. Five sub-iterations are used per time step, and the residual RMS of each equation was less than 5×10^4 at the end of each time step.

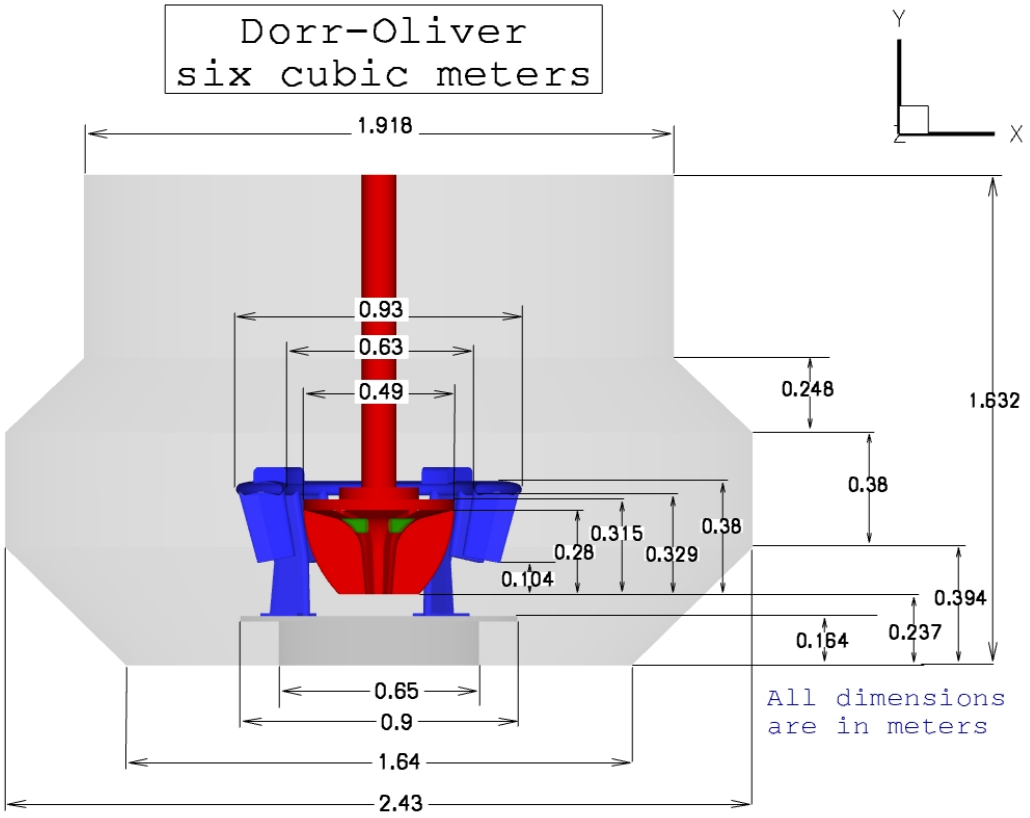

Figure 6.1: Overall dimensions of a $6m^3$ model of Dorr-Oliver flotation cell

No-slip boundary condition is imposed on all solid walls. The flow in a small duct leading to the air injection opening is modeled, and inlet boundary condition with specified air normal-velocity is specified on the inlet to the duct. The top surface of the actual tank is extended into an overflow tank (not shown in figures). Outflow boundary condition with prescribed air velocity that satisfies global conservation of air volume flow rate through the machine is imposed at the top of the overflow tank. This treatment of the tank top boundary condition is more suitable for unsteady flow than the degassing boundary condition. This is because air holdup and pulp interface are not known a priori. The actual tank is initialized with 100% water, and the overflow tank is initialized with 100% air. The overflow tank is used to permit the water level to rise due to the accumulation of air in the pulp, and at the same time, it does not allow water to exit the computational domain. No boundary conditions are needed at the interface between the actual tank and the overflow tank. The governing equations of

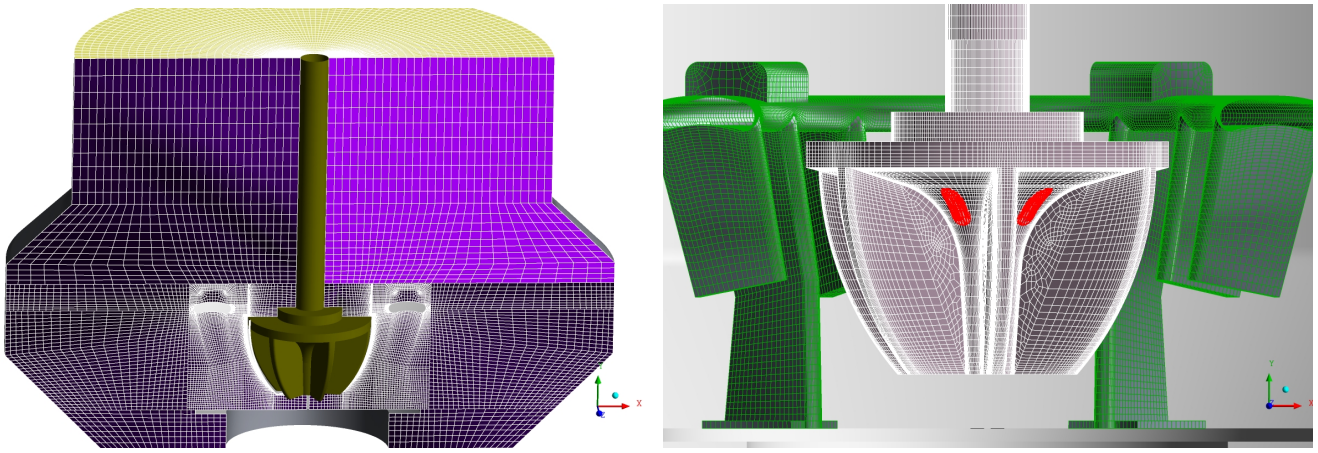

(a) Block structured mesh (b) Surface grids on rotor and stator blades

Figure 6.2: Computational domain and grid in Dorr-Oliver $6m^3$

the two-phase flow are solved in both tanks allowing air and water to flow between the tanks as required by the transport equations.

6.3 Results and Discussion

6.3.1 Flow Details for $d_b = 0.5mm$

The results for the case of bubble diameter of $0.5mm$ will be presented in more details here. The effects of bubble diameter will be briefly discussed. Contours of air volume fraction α on the rotor surface are depicted in Figure 6.3a. Upon exiting the injection slots, air adheres to the rotor top plate and drifts towards the suction sides (these are the receding faces) of the rotor blades. Air exits the rotor mainly from corners at the intersections of the suction sides of the blade with the ceiling of rotor. The major part of pressure sides (advancing surfaces) is wetted with water. Shown in Figure 6.3b are pressure P contours (flooded contours) and friction lines (black lines) that give the direction of water velocity (relative to the rotor) very close to the rotor surface. Friction lines show attachment line in the region of high pressure near the leading edges of the blades.

Water flows inward on the pressure sides and outward on the suction sides, which implies the presence of passage vortices. Relative superficial air velocity vectors at the rotor exit are concentrated near the rotor top and mainly near the suction sides. These vectors are colored by the local air volume fraction. Also shown in the figure is an iso-surface of air volume fraction equal to $\alpha = 0.6$. Iso-surface of water relative velocity magnitude V_{wr} of $5.0m/s$ is shown in Figure 6.3c. The iso-surface is colored by the water radial velocity component. The

negative radial velocity (blue color) indicates that water enters rotor passages through the lower two thirds of rotor and exits through the upper one third with maximum outward radial velocity near the end plate. Also shown in the figure are air relative velocity vectors, which are colored by the air volume fraction. An air jet exits the rotor passage near the upper corner, above and somewhat segregated from the water jet. An iso-surface of air volume fraction of $\alpha = 0.1$ is used to show the passage vortices, which are shown in Figure 6.3d. The iso-surface is colored by air radial velocity. The blue color on bottom (negative radial velocity) and the red color on top (positive radial velocity) clearly indicate the presence of a vortex. The vortex is anchored on the suction side of the blade and exits the rotor near the upper corner of the pressure side. The vortex is made visible by air bubbles trapped in the vortex core. In addition, as air is injected into the rotor it is squeezed by the water flow towards the rotor end wall.

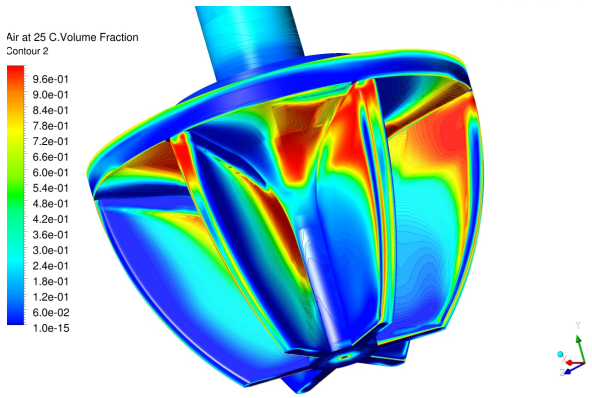

(a) Air volume fraction α on rotor surface

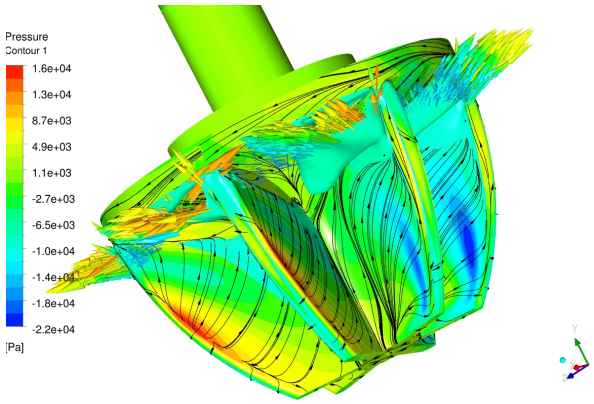

(b) pressure P contours on rotor surface

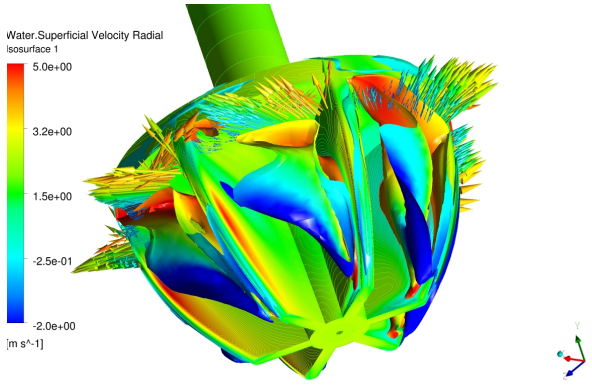

(c) iso-surface of water superficial relative velocity $V_{wr} = 5.0m/s$

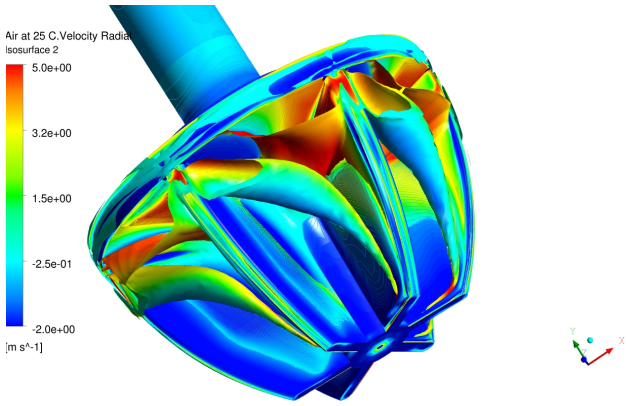

(d) iso-surface of air volume fraction $\alpha = 0.1$ showing rotor passage vortices

Figure 6.3: Flow structure in the rotor of Dorr-Oliver $6m^3$

Next, we discuss the flow characteristics downstream of the stator blades. The flow exits the upper third of the rotor as six pulsating jets with strong radial and circumferential velocity

components. The six jets impinge on the sixteen-blade stator and emerge from the stator as sixteen radial jets. The jet locations relative to stator are shown in Figure 6.4a by water superficial velocity V_w iso-surface of $0.92m/s$, which is colored by air volume fraction. As the flow exits the rotor and impinges on stator blades leading edges, a small fraction of it splashes over the ring carrying some of the high air volume fraction above the ring as indicated by the color of the small eight tongs between rotor and stator. The major part of flow, however, goes below the stator ring.

Figure 6.4b shows an iso-surface of air volume fraction of $\alpha = 0.15$ and the contours of air volume fraction on the rotor surface. Air bubbles are mainly convected by the jets towards the tank walls. Some of the air-rich flow splashes on the stator blades and escapes through the gap between rotor and stator. Air volume fraction, air superficial radial velocity, and water superficial radial velocity profiles on two vertical lines at radial distances $r = 0.52$ and $0.92m$ are shown Figures 6.5a-6.5c, respectively. Air volume fraction profiles very close to the stator at $r = 0.52m$ shows a double peak, but only the lower peak is convected as can be deduced from the air superficial radial velocity profile shown in Figure 6.5b. The air volume fraction profile at $r = 0.92m$ shows a maximum in the jet region but also an increase in air concentration above and below the jets. As the jets impinge nearly normally on the tank walls, they recirculate part of the air into the lower and upper portions of the tank. The velocity profiles diffuse due to turbulent momentum transport and also because of the increase of flow area in the radial direction. Negative radial velocity indicates the return flow into the rotor region. The jets are directed slightly upward, and the two profiles for air and water are somewhat similar in the jet regions.

6.3.2 Effects of Bubble Diameter on Void Fraction

In the present two-phase flow simulations, a uniform bubble diameter is used. To study the effects of bubble diameter on the flow characteristics, three separate simulations for bubble diameters of 2.0, 1.0, and $0.5mm$ are conducted. Air volume fraction contours in a vertical plane passing through jet region are shown in Figures 6.6a-6.6c for the three mentioned bubble diameters, respectively.

As shown in Figure 6.6a for a large bubble diameter of $2mm$, higher buoyancy force relative to drag causes air bubbles to escape through the gap between rotor and stator. The portion of air that escapes through the gap drifts towards the shaft (low pressure region due to centrifugal forces) and rises upward to the water surface. The portion of air bubbles that passes through stator is convected with water jets and rises upward near tank walls towards water free surface. Most of the air for this bubble diameter escapes through the gap between rotor and stator. Negligible amount of air bubbles are convected downward with water stream to re-enter the rotor.

Similarly, it is concluded from Figure 6.6b that for bubble diameter of $1mm$, buoyancy force on air bubbles is still high enough to cause some air to escape through the gap between rotor

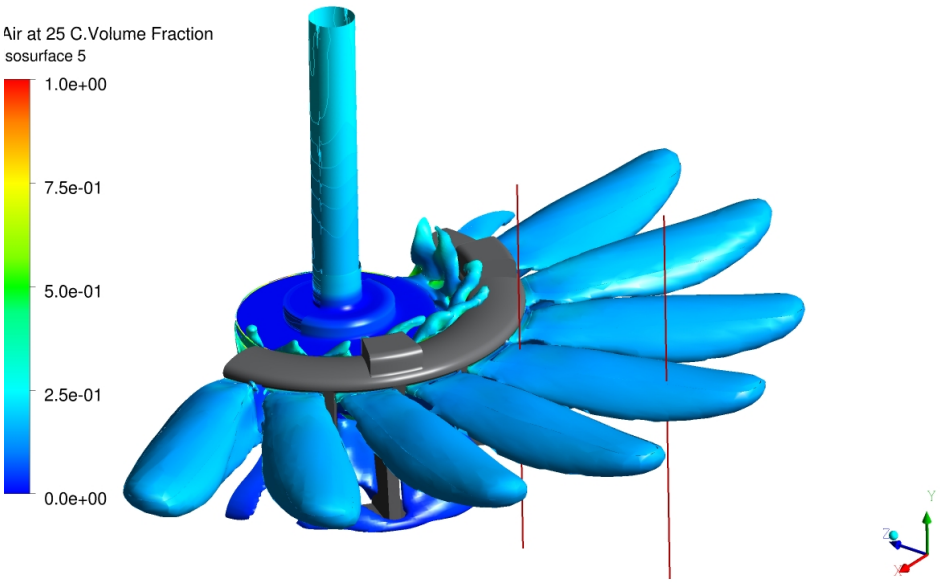

(a) Iso-surface of water superficial velocity $V_w = 0.92m/s$ showing jets downstream of stator

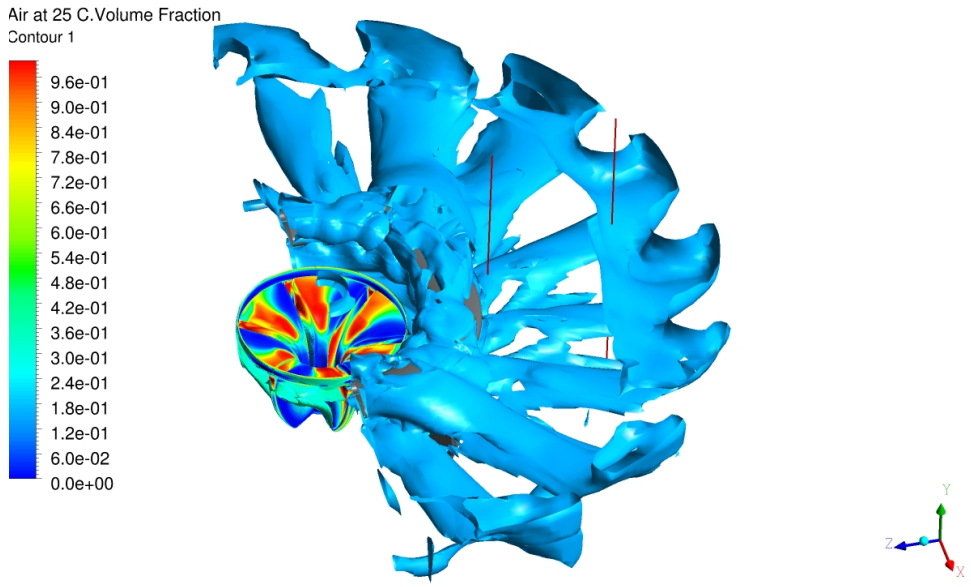

(b) Iso-surface of air volume fraction of $\alpha = 0.15$, lines at radii $r = 0.52$ and $0.92m$

Figure 6.4: Flow structure in the tank of Dorr-Oliver $6m^3$

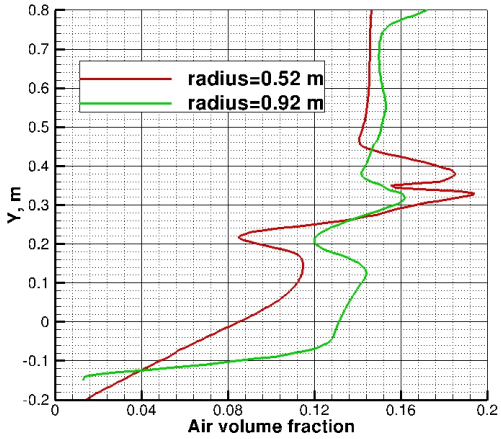

(a) Air volume fraction α at $r = 0.52$ (red) and $0.92m$ (green)

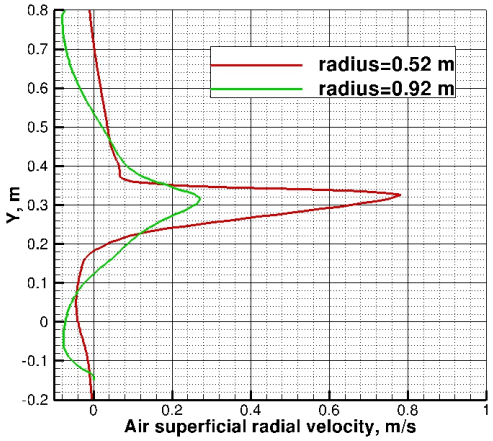

(b) Air superficial radial velocity $V_{a,radial}$ at $r = 0.52$ (red) and $0.92m$ (green)

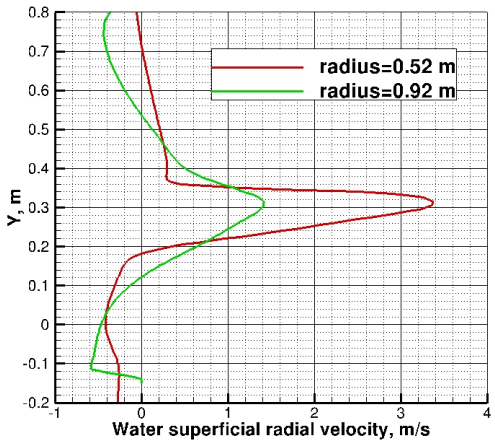

(c) Water superficial radial velocity $V_{a,radial}$ at $r = 0.52$ (red) and $0.92m$ (green)

Figure 6.5: Air volume profiles downstream of the stator in Dorr-Oliver $6m^3$

and stator. The portion of air bubbles that passes through stator is convected with water jets and drifts upward near tank walls towards water surface. Some of the air is convected downward into lower portion of the tank. The air is well dispersed throughout the tank.

Unlike the previous two cases, as shown in Figure 6.6c for a small bubble diameter of $0.5mm$, higher drag relative to buoyancy causes air bubbles to travel longer with water jets. Most of the air bubbles pass through stator and are convected with water stream. Air bubbles are dispersed throughout the tank volume, and some air re-enters the rotor.

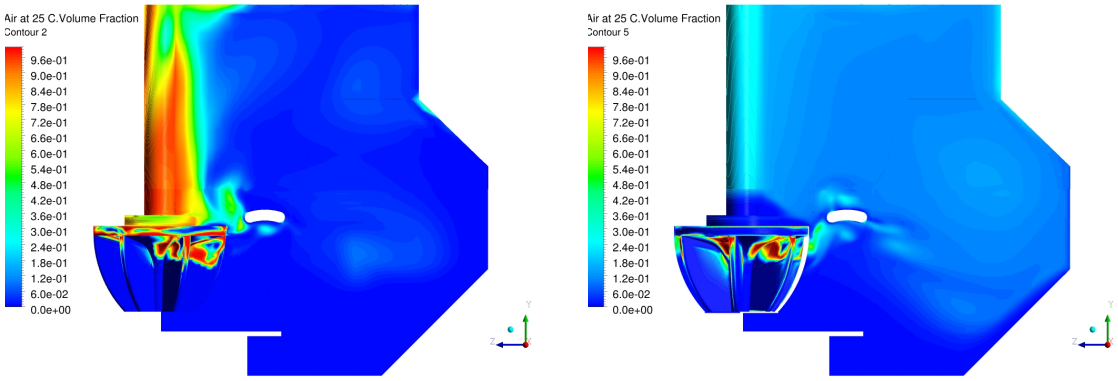

(a) Air volume fraction α contours for bubble diameter $2mm$

(b) Air volume fraction α contours for bubble diameter $1mm$

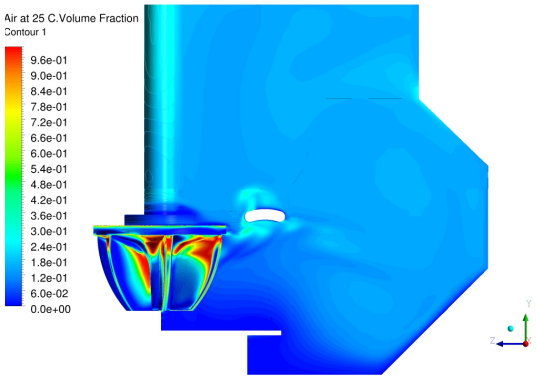

(c) Air volume fraction α contours for bubble diameter $0.5mm$

Figure 6.6: Effect of bubble size on air volume fraction in the tank of Dorr-Oliver $6m^3$

6.3.3 Comparison of CFD Results with Experiments

Validation of the computational model is very important to build confidence in CFD as a viable tool for the analysis of such a complex two-phase flows. The flow in a flotation cell poses many challenges to both CFD modeling and experimental measuring techniques.

Such challenges including three-dimensional unsteady shear flow, turbulence production and dissipation, rotating components, and multiphase phenomena. Mean velocity and turbulence statistics have been measured in a $6m^3$ Dorr-Oliver pilot cell for both single and two phase flow [75] and [74].

Comparisons between CFD and experimental data [75]- [74] for void fraction on two vertical lines outside stator are shown in Figures 7a,b. An iso-kinetic probe had been developed and used to measure air void fraction [74]. The comparison in Figures 6.7a and 6.7b shows that the CFD agrees with the experimental data in the jet region for bubble diameter d_b of $1.0mm$. Away from the stator, the overall level air volume fraction of CFD is comparable to the level of the experimental data however the trend below the jet is different. This may be attributed to the production of smaller bubbles (smaller than the diameter specified in the simulations) in the jet shear layers thereby increasing the local void fraction as supported by the increase of the void fraction below the jets as the bubble size decreases from 2.0 to $0.5mm$. In the simulation, gas holdup is 13%, 8% and 3% for bubble diameters of 0.5, 1.0 and $2.0mm$, respectively. Experimental gas holdup reports 6.8% where a bubble size distribution exists in the physical experiment.

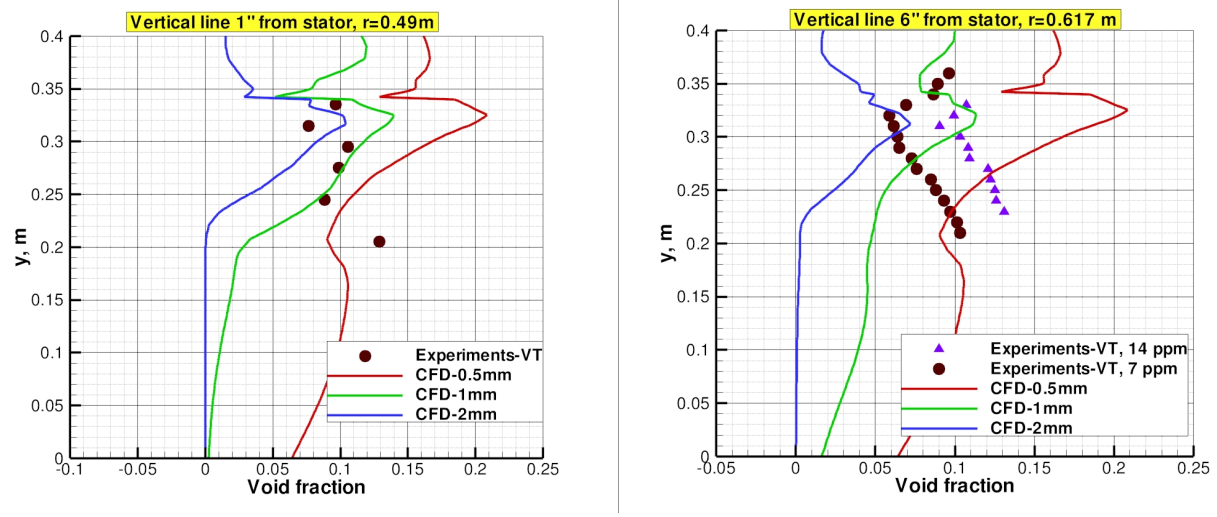

(a) Air volume fraction α profile at $25.4mm$ downstream of stator

(b) Air volume fraction α profile at $152.4mm$ downstream of stator

Figure 6.7: Comparison between CFD and experiments for air volume fraction profiles in Dorr-Oliver $6m^3$

Water superficial velocity profiles on vertical lines in the gap between rotor and stator and outside that region are shown in Figures 6.8a-6.9b. All velocities are normalized by the rotor tip speed (U = 6.414 m/s.). Each profile is an average over 16 vertical lines that have the same circumferential location relative to the stator; which has 16 blades; however, they are not averaged over time.

It is evident from Figures 6.8a-6.8c that the bubble diameter has some effects on the water superficial radial velocity within and outside the rotor-stator regions. CFD profiles for 1.0 mm bubble diameter show good agreement with the experimental data. Of course, in the experiments, a bubble size distribution exists, and the present simulations suggest that the most probable bubble diameter is $1.0mm$. Comparison between CFD profiles and experimental data for tangential and vertical velocity components in the gap between rotor and stator are depicted in Figures 6.9a-6.9b respectively. Very good agreement is obtained in that region for bubble diameters of 1 and $0.5mm$. The strong buoyancy effects on the larger bubble diameter of $2mm$ gives significantly higher vertical water velocity in the gap. Outside the stator, the tangential component is small in comparison to the radial component; not presented here.

The comparison shows some deviations between experimental and CFD results due to the existence of multi-size bubbles in the experimental work, while in CFD work a mono-size of the bubbles has been applied. Other sources of uncertainty in the CFD model is the model used to evaluate drag on bubbles which is valid only at low volume fraction, whereas in this machines regions of volume fraction as high as $100\% exist$. Notwithstanding the deviations between CFD and experimental data, and considering the complexity of such a flow, the agreement between CFD results and experimental data is deemed good; which lends strong support for the validity of the CFD model.

Figures 6.10a-6.10c show a comparison between CFD and experiments [75]- [74] for turbulent kinetic energy TKE normalized by the square of the rotor tip speed $U2$ in different regions in Dorr-Oliver $6m^3$ pilot cell. High levels of turbulent kinetic energy are predicted in the gap between rotor and stator. The high levels are localized in the high speed jets out of the rotor. As the jets impinge on stator blades, they break up into smaller jets downstream of the stator resulting in a more uniform distribution of turbulent kinetic energy but over a larger volume. Very good agreement is obtained for bubble diameter d_b of $1.0mm$ in the gap between rotor and stator. In addition, good agreement is obtained immediately downstream of the stator, but there is significant differences in the region far from the stator. As mentioned earlier the bubble size distribution in the experiments could cause these deviations, and also the turbulence model utilized with the RANS equations in the CFD model does not account for bubble induced turbulence, its importance is noted by Van den Akker [12]. Generally, turbulence in the continuous phase may be generated by shear due to large-scale velocity gradient as well as by the presence and relative motion of the dispersed phase. In addition, the dispersed phase may exhibit a turbulent flow behavior in response to the turbulent motions of the continuous phase. Another source of uncertainties in the CFD results is the fact that in unsteady RANS simulations there is no clear-cut distinction between time scales, some scales are treated by the turbulence models, and others are resolved by the averaged equations. There are also uncertainties in the experimental data. The CFD results are encouraging; however, further improvements in turbulence modeling for multiphase flow are needed. Further validation for single phase flow is presented in the appendix. Figure 6.11 shows contours of the turbulent kinetic energy dissipation rate ϵ in a horizontal plane passing

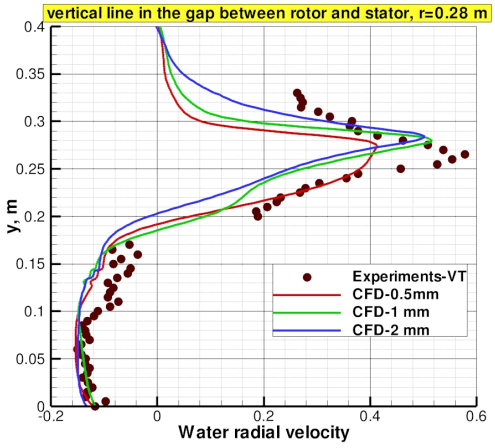

(a) Normalized water superficial radial velocity on a vertical line $r = 0.28m$ in the gap between the rotor and stator

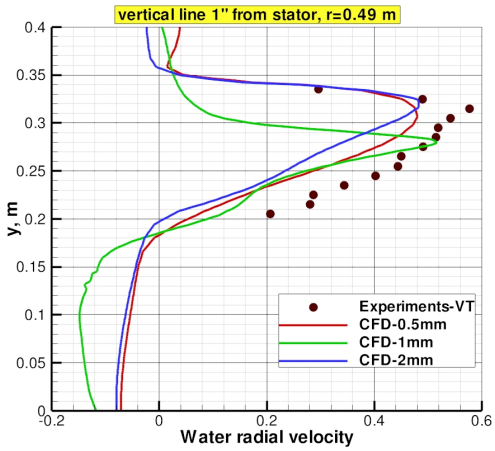

(b) normalized water superficial radial velocity on a vertical line at radial distance $25.4mm$ from the stator ring

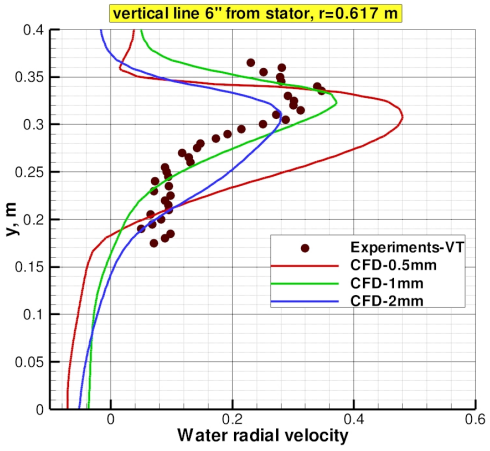

(c) normalized water superficial radial velocity on a vertical line at radial distance $152.4mm$ from the stator ring

Figure 6.8: Comparison between CFD and experiments for water superficial radial velocity profiles in Dorr-Oliver $6m^3$

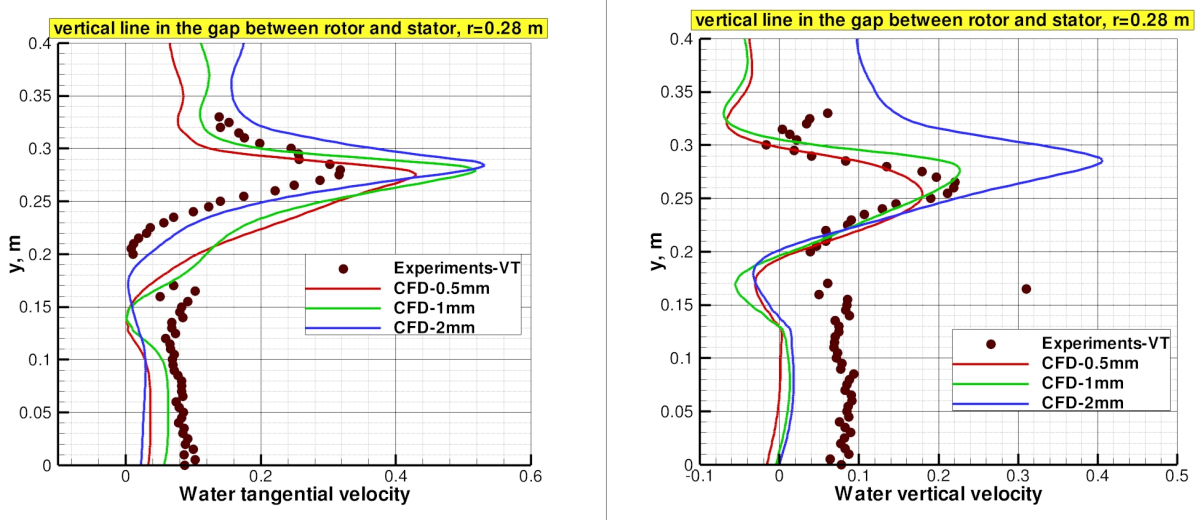

(a) Normalized water superficial tangential velocity on a vertical line $r = 0.28m$ in the gap between the rotor and the stator

(b) Normalized water superficial vertical velocity on a vertical line $r = 0.28m$ in the gap between the rotor and the stator

Figure 6.9: Comparison between CFD and experiments for water superficial tangential and vertical velocity profiles in Dorr-Oliver $6m^3$

through the rotor, stator and the tank at the jets maximum velocity. TKE dissipation rate are maximum in the regions between rotor and stator and between stator blades. Ragab and Fayed [50] showed that high dissipation rate has favorable effects on collisions frequency of particles and bubbles in the regions between rotor and stator blades. Nevertheless, high dissipation rate has also adverse effects on the attachment probability in these regions.

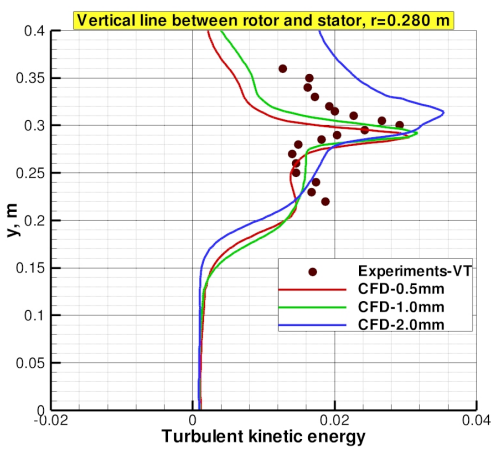

(a) Normalized TKE on a vertical line $r = 0.28m$ in the gap between the rotor and the stator

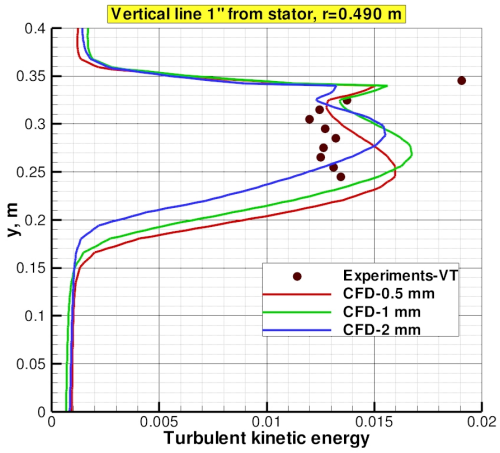

(b) Normalized TKE along vertical line at $25.5mm$ from the stator ring in the radial direction

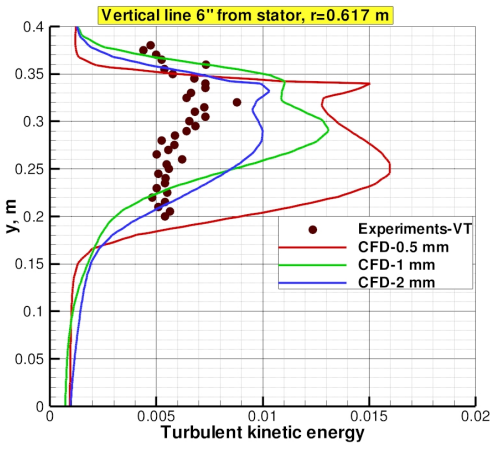

(c) Normalized TKE on a vertical line 152.4 mm from the stator ring in the radial direction

Figure 6.10: Comparison between CFD and experiments for water turbulent kinetic energy profiles in Dorr-Oliver $6m^3$

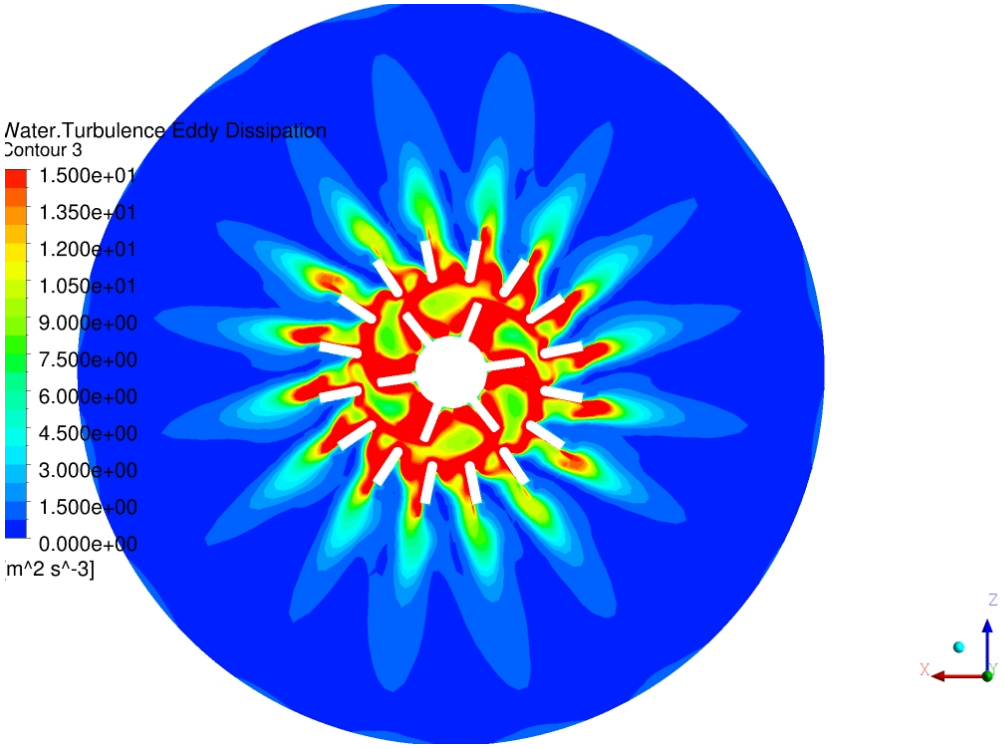

Figure 6.11: Turbulent kinetic energy dissipation rate in a horizontal plane passing through the jets

6.4 Conclusions

In this paper, two-phase (water and air) flow in a $6m^3$ model of Dorr-Oliver flotation cell, which is an air-forced mechanically-stirred machine, is simulated. Euler-Euler two-fluid approach is used, and the transport equations are solved in time (unsteady simulation). A block structured grid is used to model a $180 - degree$ sector (half the machine) and rotationally periodic boundary conditions are enforced. Air flow rate is specified, and uniform bubble diameter is assumed. A novel treatment of the free surface boundary condition is introduced. The results indicate:

- Air injected into the rotor is squeezed between the rotor solid surface and the water pumped by the rotor. The air-water flow exits the upper one-third of the rotor passage with air-rich above water-rich flow. The air-rich flow drifts towards the suction (or receding) sides of the rotor blades, while the water-rich flow drifts towards the pressure (or advancing) sides of the rotor blades. Thus, air is not fully dispersed at the rotor exit, but is somewhat segregated from water.
- For large bubble diameter $d_{=}2mm$, higher buoyancy relative to drag causes most of the injected air to escape through the gap between rotor and stator.
- For small bubble diameter $d_{=}0.5mm$, higher drag relative to buoyancy causes air bubbles to travel longer distances with water jets. Most of the air bubbles pass through stator and is convected with the water stream. Some air re-circulates in the bottom tank, re-enters the rotor and accumulates in the core of rotor passage vortices, which are low pressure regions.
- Bubble diameter has significant effects on the gas hold up. Higher gas hold up ratio is observed for smaller bubble diameters.
- High levels of turbulent kinetic energy are predicted in six (number of rotor blades) regions between rotor and stator. These regions, however, are localized in the high speed jets out of the rotor. As these jets impinge on stator blades, they breakup into 16 (number of stator blades) smaller jets downstream of stator resulting in a more uniform distribution of turbulent kinetic energy over a larger volume.
- Flow exits stator as spinning radial jets (16 jets) that impinge on tank wall forming strong recirculation region in the lower part of the tank, and a weaker circulation in the upper part.

CFD results have been validated by comparison with experimental data [75] and [74]. The comparisons show:

1. Good to fair agreement between CFD and experimental data for the mean velocity profiles at different radial locations. The results indicate that the most probable bubble diameter is around $1.0mm$.

2. CFD predicts correct trend and profiles of TKE.

3. In addition, for single phase (water) simulations, good agreement for pressure distribution on stator windward sides is obtained. CFD predicts the right trend for pressure distribution on leeward side of stator blades but fair agreement for pressure magnitude (Results are shown in [56]).

This work demonstrates the viability and validity of CFD as a technique that can provide detailed description of the two-phase flow in a flotation cell. Further developments of the computational model, however, are still needed. In view of the important effects of bubble diameter on two-phase simulations, future simulations should account for a distribution over a range of bubble diameter. The effects of bubble breakup and coalescence using a population balance model should also be considered. More simulations are needed to determine sensitivity of CFD results to drag coefficient and turbulence models. Existing bubble drag models assume very low void fraction; drag models that account for high volume fraction need to be developed. The complex three-dimensional unsteady shear flow calls for a more detailed description of the important large scales of turbulence. It is feasible to apply large-eddy simulations to predict multiphase flow in flotation machines.

Chapter 7

Conclusions and Future Work

7.1 Conclusions

In this dissertation, we made contributions to the advancement of computational modeling of multiphase turbulent flows and its application to mineral flotation machines.

1. We presented new results obtained by direct computation of collisions frequency of mono- and bi-dispersed phases in a turbulent flow, and validated theoretical models. The salient feature of the method used here for frequency computation is the use of a high fidelity direct numerical simulations for the carrier phase and integration of the equations of motion of the dispersed phases simultaneously with the carrier phase equations using the same time advancement technique. We found that particles at Stokes number of one, in addition of being preferentially concentrated, they are also segregated from bubbles. As a result the radial distribution function in the case of bi-dispersed flow can be less than one, whereas existing theoretical models do not predict this result. This finding is significant because it means that the collisions frequency is reduced by this segregation and should be taken into consideration in computational modeling of such flows.

2. Collisions frequency computation at very high turbulence Reynolds number demands the use of large-eddy simulations (LES). This dissertation proposed a numerical method for the construction of subgrid velocity fluctuations for the purpose of tracking particles and bubbles of sizes on the order of Kolmogorov length scale. The method is based on multifractal representation of the cascade of large scale turbulent structures to small scales subgrid fluctuations.

3. We developed a new treatment of inflow/outflow boundary condition for forced-air and self-aspirated flotation machines. The developed treatment is more reliable than

the standard treatment known as the degassing boundary condition that we found to produce nonphysical flow behavior.

4. We developed a CFD-based flotation model for the prediction of pulp rate constant for flotation machines. The model makes use of the detailed hydrodynamic two-phase flow CFD data (dissipation rate and void fraction) and provides detailed picture of spatial distribution of particle-bubble attachment and detachment rates throughout the machine. The developed model is a very useful design tool.

Next, we discuss in more details the above contributions.

Particles and bubbles suspended in homogeneous isotropic turbulence are tracked and their collisions frequency is determined as function of particle Stokes number. The carrier phase velocity fluctuations are determined by Direct Numerical Simulations using a pseudo-spectral method. The equations of motion of dispersed phases account for Stokes drag, added-mass force, and pressure gradient in the carrier phase. The equations of motion are integrated simultaneously with the forced Navier-Stokes equations of the carrier phase using a third-order Runge-Kutta time stepping scheme. Simulations for turbulence Reynolds numbers $Re_\lambda = 57$, 77 and 96 have been performed, and the computed collisions kernels are used to evaluate theoretical models developed by Zaichik et al. [78] and Zaichik et al. [79].

The present DNS results revealed the importance of accumulation effects on the collisions kernel of particles and bubbles. In DNS we observed that bubbles, as they migrate to low pressure vortex cores, tend to be segregated from heavy particles. *This segregation leads to reduced collisions frequency between particles and bubbles. We found that the radial distribution function at collision is less than one for the case of particle-bubble collisions.* Most theoretical models assume such a function to be one, and hence they stand to overpredict the collision frequency especially for particle Stokes number near one for which particles accumulate in the high strain regions.

Excellent agreements between DNS and Zaichik et al. model [78] for mono-disperse (particle-particle) and bi-disperse (particle-bubble) radial relative velocity are obtained. Even though the radial relative velocity is well predicted by the model, the radial distribution function show only qualitative agreement with DNS. The model is applicable only to heavy small particles, and if applied to the case of bi-disperse (particle-bubble) collisions, the predicted radial distribution function is nearly one whereas DNS predicts lower than one values due to particle-bubble segregation. A more accurate theoretical model for the radial distribution function for bi-disperse particle-bubble collisions is needed. The model should consider the particle-bubble segregation.

Zaichik et al. [79] accounts for both pressure gradient in the carrier phase and added-mass force, and it provides only expressions for the radial relative velocity. Excellent agreement

between DNS and the model predictions are obtained for the bi-disperse particle-bubble collisions, but only qualitative agreement is obtained for the mono-disperse particle-particle collisions.

Large-Eddy simulation of particles and bubbles collisions are studied. The carrier phase velocity fluctuations are determined by LES using a pseudo-spectral method and spectral eddy viscosity model is used to close the momentum equation. Comparison between the turbulent kinetic energy spectra from DNS (grid 256 points) and LES (grid 32 points) shows good agreement. The equations of motion of dispersed phases account for Stokes drag, added-mass, and pressure gradient in the large resolved scales of the carrier phase. The equations are integrated simultaneously with the equations of the carrier phase using a third-order Runge-Kutta time stepping scheme. Simulations for turbulence Reynolds numbers $Re_\lambda = 96$ have been performed, and the computed collision kernel is compared with that of DNS and theoretical model developed by Zaichik et al. [78].

The present LES results revealed the importance of SGS velocity fluctuations as well as the SGS carrier phase acceleration on the collision rate of particles and bubbles. In LES we also observed that bubbles, as they migrate to low pressure vortex cores, tend to be segregated from heavy particles as observed in DNS. However, the radial distribution function in LES is not as low as the DNS because the contribution of the subgrid scales to the pressure gradient was neglected in the present LES.

we proposed to extend Burton and Dahm [7] multifractal model to synthesize the instantaneous subgrid velocity fluctuations. We also tested the use of a frozen subgrid velocity field obtained from a filtered DNS field. Adding the synthesized multifractal or frozen subgrid velocity fields to the resolved field has no potential improvements of the LES when compared with DNS. We conclude from this study that for accurate particle tracking in LES the subgrid velocity fluctuations must be dynamically realizable field (temporally and spatially correlated with the large scale motion). Adding random SGS velocity fluctuations is not enough to capture the correct radial distribution functions of dispersed phases especially for bubbles-particles collisions where the pressure gradient term (or acceleration $D\vec{u_f'}/Dt$) is responsible for particle-bubble segregation for particle Stokes number near one.

A CFD-based flotation model is presented that can be used to determine the pulp rate constant in flotation machines. It uses a first-order rate equation, where processes of collision, attachment and detachment are described by well known theoretical and empirical formulae. The model uses local values of turbulent energy dissipation rate and air volume fraction. The spatial distributions of these two parameters are determined by simulations of two-phase flow (air and water) in the machine. Not only the average pulp rate constant can be estimated but also the regions of high/low rate can be identified. The CFD-based flotation model presented here is also used to determine the dependence of rate constant at any locality within the pulp on particle diameter, particle specific gravity, contact angle, and surface tension. The model is a very useful design tool because it can be used to establish the effectiveness of different components (rotor, stator, or disperser jets) on the pulp recovery.

7.2 Future Work

In this dissertation only small particles on the order of Kolmogorov scale have considered. Turbulent modulations due to these particles are negligible because their sizes are in the dissipative length scale. And the comparison between DNS/LES calculations are based on this assumption. However, particles size can vary from the dissipative length scale to the inertial range length scale. Direct numerical simulations of turbulent dispersion of particles of sizes in the inertial range are recommended to account for the generated wakes of these large particles and their effects on the modulation of the turbulent flow field. Validation of existing theoretical models such as that given by Zaichik et al. [79] model for large particles are needed as well. This is because Zaichik et al. [79] is valid for arbitrary particle size and Stokes number.

For flotations machines applications, the effects of shear flow on the breakup of large bubbles is another challenging computational multiphase flow problem of great importance.

Bibliography

[1] J. Abrahamson. Collision rate of small particles in a vigorously turbulent fluid. *Chem. Eng. Sci.*, 30:1371–1379, 1975.

[2] G. Ahmadi and V.W. Goldschmidt. Motion of particles in a turbulent fluid-The Basset history term. *Journal of Applied Mechanics, Trans. ASME*, E38:561–563, 1971.

[3] Gorain B.K., Franzidis J.P., and Manlapig E.V. Studies in impeller type, impeller speed and air flow rate in an industerial scale flotation cell-part1: Effects on bubble size distribution. *Minerals Engineering*, 8 No. 6:615–635, 1995.

[4] F. Bloom and T. J. Heindel. On the structure of collision and detachment frequencies in flotation models. *Chem. Eng. Sci.*, 57:2467–2473, 2002.

[5] F. Bloom and T. J. Heindel. Modeling flotation separation in semi-batch process. *Chem. Eng. Sci.*, 58:403–422, 2003.

[6] G. C. Burton. *A Multifractal subgrid-scale modeling for the Large-Eddy Simulation of Turbulent flows*. PhD thesis, University of Michigan, Ann Arbor, NC, 2003.

[7] G. C. Burton and W. J. Dahm. A multifractal subgrid-scale modeling for large-eddy simulation. i. model development and a priori testing. *phys. Fluids*, 17:075111, 2005.

[8] C. Canuto, M.Y. Hussaini, A. Quarteroni, and T.A. Zang. *Spectral Methods. Evolution to Complex Geometries and Applications to Fluid Dynamics*. Springer, New York, 2007.

[9] J.P. Chollet and M. Lesieur. Parametrization of small scales of three-dimensional isotropic turbulence utilizing spectral closures. *J. Atmos. Sci.*, 38:2747–2757, 1981.

[10] R. Clift, J.R. Grace, and M.E. Weber. *Bubbles, Drops and Particles;*. Dover Publications, Mineola NY USA, 2005.

[11] Z. Dai, D. Fornasier, and J. Ralston. Particle-bubble attachment in mineral flotation. *Journal of Colloid and Interface Science*, 217:70–76, 1999.

[12] H. E. A. Van den Akker. Toward a truly multiscale computational strategy for simulating turbulent two-phase flow processes. *Ind. Eng. Chem. Res.*, 49:10780–10797, 2010.

[13] V. Eswaran and S.B. Pope. An examination of forcing in direct numerical simulations of turbulence. *J. Computers and Fluids*, 16 No. 3:257–278, 1988.

[14] G. Evans, E. Doroodchi, G. Lane, P. Koh, and P. Schwarz. Mixing and gas dispersion in mineral flotation cells. In *6th International Symposium on Mixing Industrial Process Industries (ISMIP VI)*, Niagara on the Lake Canada, August 2008.

[15] H. Fayed and S. Ragab. Direct numerical simulation of particles-bubbles collisions kernel in homogeneous isotropic turbulence. *J. Computational Multiphase Flows*, 5 No. 3:167–188, 2013.

[16] P. Fede and O. Simonin. Numerical study of the subgrid fluid turbulence effects on the statistics of heavy colliding particles. *Phys. Fluids*, 18:045103, 2006.

[17] P. Fede, O. Simonin, P. Villedieu, and K. D. Squires. Stochastic modeling of the turbulent subgrid fluid velocity along inertial particle trajectories. In *Proceedings of the 2006 Summer Program*, Center for Turbulence Research Stanford University, Stanford, CA, December 2006.

[18] J. Bardina J. H. Ferziger and R. S. Rogallo. Improved subgrid models for large eddy simulation. In *AIAA 13th Fluid and Plasma Dynamics Conference*, Snowmass, Colo., July 1980.

[19] D.T. Gillespie. Exact numerical solution of the ornstien-uhlenbeck process and its integral. *J. Physical REVIEW E*, 54 No. 2:2084–2091, 1996.

[20] D. Govender, D. Lelinski, and F. Traczyk. Hybrid energy flotation^{TM} - on the optimization of fine and coarse partile kinetics in a single row. *The Journal of The South African Institute of Mining and Metallurgy*, 113:285–296, 2013.

[21] H.Fayed and S. Ragab. CFD analysis of two-phase flow in a self aerated flotation machine. In *SME Annual Meeting and Exhibit*, Seattle WA, February 2012.

[22] H.Fayed and S. Ragab. Collisions frequency of particles and bubbles suspended in homogeneous isotropic turbulence. In *AIAA 50th Aerospace Sciences Meeting*, Nashville, TN, December 2012.

[23] A.T. Hjelmfelt and L.F. Mockros. Motion of discrete particles in a turbulent fluid. *Appl. Sci. Res. A*, 16:149–161, 1966.

[24] Z. Huang and Tim Olson. Froth and kinetic flotation, CFD simulation, new rotor and stator designs. In *SME Annual Meeting and Exhibit*, Denver Colorado, February 2013.

[25] G. Jin, G.W. He, and L.P. Wang. Large-eddy simulation of turbulent collision of heavy particles in isotropic turbulence. *Phys. Fluids*, 22:055106, 2010.

[26] F. Kerdouss, A. Bannari, and P. Proulx. CFD cfd modeling of gas dispersion and bubble size in a double turbine stirred tank. *Chem. Eng. Sci.*, 61:3313–3322, 2006.

[27] P. Koh and P. Schwarz. CFD model of a self-aerating flotation cell. *Int. J. Miner. Processing*, 85:16–24, 2007.

[28] P. Koh and P. Schwarz. Cfd models of microcell and jameson flotation cells. In *7th International Conference on CFD in the Minerals and Process Industries*, Melbourne Australia, December 2009.

[29] P. Koh, P. Schwarz, and Y. Bourke. Development of CFD models of mineral flotation cells. In *3rd International Conference on CFD in the Minerals and Process Industries*, Melborne Australia, December 2003.

[30] P.T.L Koh and M.P. Schwarz. CFD modeling of bubble-particle attachments in flotation cells. *Minerals Engineering*, 19:619–626, 2006.

[31] R. Kraichnan. Eddy viscosity in two and three dimensions. *J. Atoms. Sci.*, 65:1521–1536, 1976.

[32] F.E. Kruis and K.A. Kusters. The collision rate of particles in turbulent flow. *Chem. Eng. Communications*, 158:201–230, 1997.

[33] F. Lehr and D. Mewes. A transport equation for the interfacial area density applied to bubble columns. *Chem. Eng. Sci*, 56:1159–1166, 2001.

[34] F. Lehr, M. Millies, and D. Mewes. Bubble-size distribution and flow fields in bubble columns. *AIChE*, 48 No. 11:2426–2443, 2002.

[35] F. Leipe and O.H. Mockel. Untersuchungen zum stoffvereinigen in flussiger phase. *Chemical Technology*, 30:205–209, 1976.

[36] D. L'Espérance, J.D. Trolinger, C.F.M. Coimbra, and R.H. Rangel. Particle response to low-Reynolds-number oscillation of a fluid in microgravity. *AIAA J.*, 44, No. 5:1060–1064, 2006.

[37] H. Luo and H. Svendsen. Theoretical model for drop and bubble breakup in turbulent dispersions. *AIChE*, 42 No. 5:1225–1233, 1996.

[38] C. Martinez-Bazan, J.L. Montanes, and J.C. Lasheras. On the breakup of an air bubble injected into a fully developed turbulent flow. paert 2. size pdf of the resulting daughter bubbles. *J. Fluid Mech.*, 401:183–207, 1999.

[39] M. R. Maxey. The gravitational settling of aerosol-particles in homogeneous turbulence and random flow-fields. *J. Fluid. Mech.*, 174:441–465, 1987.

[40] A. Scotti C. Meneveau. A fractal model for large eddy simulation of turbulent flow. *Physica D.*, 127:198–232, 1999.

[41] O. Metais and M. Lesieur. Spectral large-eddy simulation isotropic and stably stratified turbulence. *J. Fluid Mech.*, 239:157–194, 1992.

[42] M. Germano U. Piomelli P. Moin and W. H. Cabot. A dynamic subgrid-scale eddy viscosity model. *Phys. Fluid A*, 3:1760–1765, 1991.

[43] M.G. Nelson, F.P. Traczyk, and D. lelinski. Design of mechanical flotation machines. In *reprint SME Annual Meeting*, Denver COL., February 2011.

[44] K. Podila, A.M. Al Taweel, M. Koksal, A. Troshkoc, and Y.P. Gupta. CFD simulation of gas liquid contacting in tubular reactors. *Chem. Eng. Sci*, 62:7151–7162, 2007.

[45] W.H. Press, S.A. Teukolsky, W.T. Vetterling, and B.P. Flannery. *Numerical Recipes in Fortran, 2nd Edition*. Cambridge University Press, 1992.

[46] M. Prince and H. Blanch. Bubble coalescence and break-up in air-sparged bubble columns. *AIChE*, 36 No. 10:1485–1499, 1990.

[47] A. Prosperetti and G. Tryggvason. *Computational Methods for Multiphase Flow*. Cambridge University Press, Cambridge UK, 2007.

[48] B. Pyke, D. Fornasiero, and J. Ralston. Bubble particle heterocoagulation under turbulent conditions. *J. Colloid and Interface Science*, 265:141–151, 2003.

[49] S. Ragab, H. Fayed, and A. S. Said. Two-phase flow simulations and kinetics models of flotation machines. Technical Report October 9th, Virginia Tech, 2011.

[50] S. Ragab and H.Fayed. New model for particles-bubbles collisions frequency and applications to flotation machines. In *SME Annual Meeting and Exhibit*, Seattle WA, February 2012.

[51] R.S. Rogallo. An ILLIAC program for the numerical simulation of homogeneous, incompressible turbulence. Technical Report TM-73203, NASA, 1977.

[52] R.S. Rogallo and P. Moin. Numerical simulations of turbulent flows. *Annu. Rev. Fluid Mech.*, 16:99–137, 1984.

[53] P.G. Saffman and T.S. Turner. On the collision of drops in turbulent clouds. *J. Fluid Mech.*, 1:16–30, 1956.

[54] P. Sagaut. *Large Eddy Simulation for Incompressible Flows*. Springer, New York, third edition, 2006.

[55] J. A. Domaradzki E. M. Saiki. A subgrid-scale model based on the estimation of unresolved scales of turbulence. *Phys. Fluids*, 9:2148–2164, 1997.

[56] A. Salem-Said, H. Fayed, and S. Ragab. Numerical simulations of two-phase flow in a dorr-oliver flotation cell model. *Minerals J.*, 3:284–303, 2013.

[57] A. Salem-Said, H.Fayed, and S. Ragab. CFD simulation of a dorr-oliver flotation cell. In *SME Annual Meeting and Exhibit*, Denver Colorado, February 2011.

[58] H. Schubert. On the turbulence-controlled microprocesses in flotation machines. *Int. J. Mineral Processing*, 56:257–276, 1999.

[59] H.J. Schulze. *Physico-chemical Elementary Processes in Flotation*. Elsevier, New York, 1984.

[60] H.J. Schulze. Flotation as a hetrocoagulation process: possibilities of calculation the probability of flotation. In *Coagulation and Flocculation (B. Dobias, 1993)*, pages 321–363. Marcel Dekker, New York, 1993.

[61] J. Smagorinsky. General circulation experiments with the primitive equation. part i. the basic experiment. *Mon. Wea. Rev.*, 91:99–164, 1963.

[62] S. Stolz and N. A. Adams. An approximate deconvolution procedure for large-eddy simulation. *Phys. Fluids*, 11:1699–1701, 1999.

[63] S. Sundaram and L.R. Collins. Numerical considerations in simulating a turbulent suspension of finite-volume particles. *J. Comput. Phys.*, 124:337–350, 1996.

[64] S. Sundaram and L.R. Collins. Collision statistics in an isotropic particle-laden turbulent suspension. part. 1. direct numerical simulation. *J. Fluid Mech.*, 335:75–109, 1997.

[65] M. Thiel, J. Kurths, M.C. Romano, G. Karolyi, and A. Moura. *Nonlinear Dynamics and Chaos: Advances and Perspectives*. Springer-Verlag Berlin Heidelberg, 2010.

[66] J. Tiitinen, K. Koskinen, and S. Ronkainen. Numerical modeling of an Outokumpu flotation cell. In *Centenary of Flotation Symposium*, Brisbane Australia, June 2005.

[67] M. A. T. van Hinsberg, J. H. M. ten Thije Boonkkamp, and H. J. H. Clercx. An efficient, second order method for the approximation of the basset history force. *J. Comput. Physics*, 158:1465–1478, 2011.

[68] L. Wang, A.S. Wexler, and Y. Zhou. On the collision rate of small particles in isotropic turbulence. i. zero-inertia case. *Phys. Fluids*, 10:266–276, 1998.

[69] L. Wang, A.S. Wexler, and Y. Zhou. Statistical mechanical descriptions of turbulent coagulation. *Phys. Fluids*, 10:2647–2651, 1998.

[70] L. Wang, A.S. Wexler, and Y. Zhou. Statistical mechanical descriptions and modeling of turbulent collision of inertial particles. *J. Fluid Mech.*, 415:117–153, 2000.

[71] T. Wang, J. Wang, and Y. Jin. A novel theoretical breakup kernel function for bubbles/droplets in a turbulent flow. *Chem. Eng. Sci.*, 58:4629–4637, 2003.

[72] J.J.E. Williams and R.I. Crane. Particle collision rate in turbulent flow. *Int. J. Multiphase Flow*, 9:421–435, 1983.

[73] J.J.E. Williams and R.I. Crane. Collision rate of small particles in a homogeneous and isotropic turbulence. *AIChe*, 30:4802–807, 1984.

[74] Y. Yang. *Experimental study of multi-phase flow hydrodynamics in stirring tanks*. PhD thesis, Virginia Tech, Blacksburg, VA, 2011.

[75] Y. Yang and D. Telionis. Turbulence measurements in a flotation cell using fast-response probe. *Preprint SME Annual Meeting, Denver, Colorado, 27 February - 2 March*, 2011.

[76] R.H. Yoon and G.H. Luttrell. The effect of bubble size on fine particle flotation. *Mineral Processing and Extractive Metallurgy Review*, 5:101–122, 1989.

[77] L. I. Zaichik, V. M. Alipchenkov, and E. G. Sinaiski. *Particles in Turbulent Flows*. Wiley-VCH, Germany, 2008.

[78] L. I. Zaichik, O. Simonin, and V. M. Alipchenkov. Collision rates of bidisperse inertial particles in isotropic turbulence. *Phys. Fluids*, 18 No. 3:035110, 2006.

[79] L. I. Zaichik, O. Simonin, and V. M. Alipchenkov. Turbulent collision rates of arbitrary-density particles. *Int. J. Heat and Mass Transfer*, 53:1613–1620, 2010.

[80] L.I. Zaichik and V.M. Alipchenkov. Statistical models of clustering particles in wall and isotropic turbulent flows. *High Temperature*, 43 No. 3:426–442, 2004.

[81] L.I. Zaichik and V. Pershukov. Modeling of particle motion in a turbulent flow with allowance for collisions. *Fluid Dynamics*, 30 No. 1:49–63, 1995.

[82] Y. Zhou, A.S. Wexler, and L. Wang. On the collision rate of small particles in isotropic turbulence. ii. finite inertia case. *Phys. Fluids*, 10 No. 5:1206–1216, 1998.

[83] Y. Zhou, A.S. Wexler, and L. Wang. Modelling turbulent collision of bidisperse inertial particles. *J. Fluid Mech.*, 433:77–104, 2001.

Appendices

Appendix A

Numerical Interpolation

A.1 Hermite Interpolation

Fluid velocity at the particles instantaneous position is needed to track particles in turbulent flows. High order interpolation schemes are required to track particles and bubbles of sizes on the order of Kolmogorov′s length scale. $3D$ Lagrange interpolation with different orders (3^{rd}, 5^{th} and 7^{th}) have been tested and we found that high-order Lagrange interpolation produces large errors at regions where high velocity gradient exist. Incomplete Hermite interpolation, equivalent to Lagrange 7^{th} order, does not produces such large errors as in Lagrange interpolation.

Search algorithm described in Chapter 3 is applied to find the indices of the computation cell that contains the particle center. Velocities and their spatial gradients at the 8 corners of the that computational cell (32 degrees of freedom for each velocity component) are stored to be used in the Hermite interpolation. Each computational cell is mapped to a cube of side equal one as shown in Figure A.1 and velocity spatial derivatives are also mapped to the local coordinate system.

The interpolated velocity at any local point within the computational cell is written as follows,

$$u_f = c_o + c_1 x + ... + c_{30} x^3 y z^3 + c_{31} x y^3 z^3 \tag{A.1}$$

The 32 coefficients in Eq A.1 are found by solving a system of 32 equations as follows,

$$\begin{pmatrix} \{U\}_1 \\ \{U\}_2 \\ \vdots \\ \{U\}_8 \end{pmatrix} = [T] \begin{pmatrix} c_o \\ c_1 \\ \vdots \\ c_{31} \end{pmatrix}$$

and

$$\{U\}_n = \begin{pmatrix} u \\ \frac{\partial u}{\partial x} \\ \frac{\partial u}{\partial y} \\ \frac{\partial u}{\partial z} \end{pmatrix} \tag{A.2}$$

are the velocity and its three spatial derivatives at each corner of the computational cell ($n = 1, ..., 8$). Matrix $[T]$ depends only on the coordinates of the 8 corners of the mapped computational cell, and its inverse is obtained and stored one time before the simulation. The coefficients vector (c) is calculated as follows,

$$\begin{pmatrix} c_o \\ c_1 \\ \vdots \\ c_{31} \end{pmatrix} = [T]^{-1} \begin{pmatrix} \{U\}_1 \\ \{U\}_2 \\ \vdots \\ \{U\}_8 \end{pmatrix}$$

Eq A.1 is rewritten as follows

$$u_f = (B)\,(c) \tag{A.3}$$

and vector (B) depend on the local particle coordinates as follows

$$(B) = \begin{pmatrix} 1, x, x^2, x^3, y, y^2, y^3, z, ... \\ z^2, z^3, xy, x^2y, x^3y, xy^2, xy^3, yz, ... \\ y^2z, y^3z, yz^2, yz^3, xz, xz^2, xz^3, x^2z, ... \\ x^3z, xyz, x^2yz, xy^2z, xyz^2, x^3y^3z, x^3yz^3, xy^3z^3 \end{pmatrix} \tag{A.4}$$

Therefore, the interpolated velocity at the center of each particle is written as

$$u_f = (B)\,[T]^{-1} \begin{pmatrix} \{U\}_1 \\ \{U\}_2 \\ \vdots \\ \{U\}_8 \end{pmatrix}$$

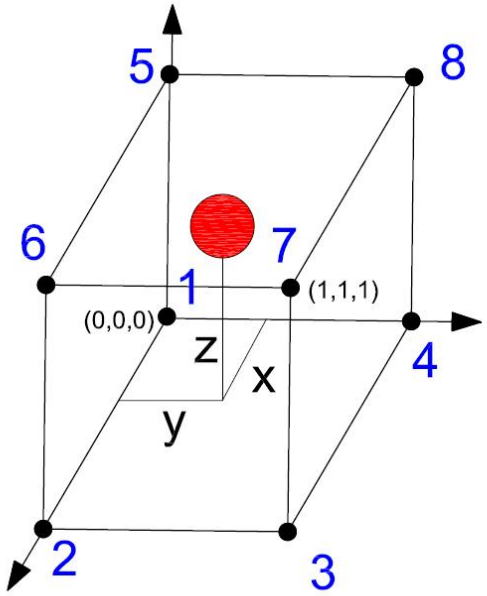

Figure A.1: Schematic diagram of a particle inside computational cell; x,y,z are local coordinate system

A.2 Tri-Linear Interpolation

Fluid accelerations are also needed at the particle position to calculate the pressure gradient and added mass terms in the particle equation of motion. Fluid accelerations at the center each particle are found by Tri-linear interpolation as follows

$$\frac{Du_f}{Dt} = (\Psi)(DU_f) \tag{A.5}$$

where

$$(DU_f) = \begin{pmatrix} \frac{Du_{f1}}{Dt} \\ \frac{Du_{f2}}{Dt} \\ \vdots \\ \frac{Du_{f8}}{Dt} \end{pmatrix} \tag{A.6}$$

which are the fluid acceleration at the 8 corners of the computational cell and

$$(\Psi) = \begin{pmatrix} 1 - x - y - z + xy + xz + yz - xyz, ... \\ x - xy - xz + xyz, ... \\ xy - xyz, ... \\ y - xy - yz + xyz, ... \\ z - xz - yz + xyz, ... \\ xz - xyz, ... \\ xyz, ... \\ yz - xyz \end{pmatrix} \tag{A.7}$$

Appendix B

CFD Simulation of Bubble Size Distribution

B.1 introduction

In minerals flotation machines air is dispersed in the pulp as bubbles with size distribution that may vary in space and time. The effect of the bubble size distribution on flotation rate has been observed since flotation early decades [3]. Bubble size distribution depends mainly on spatial distribution of turbulent dissipation rate and transport (advection) by the pulp motion; parameters that are functions of the machine rotor-stator (or disperser) design. Computational simulations can provide spatial distribution for bubble size distribution, and can be used to determine the response of such distributions to design modifications. The basic element of a computational fluid dynamics (CFD) model for predicting local bubble size distribution is a population balance model. It is usually implemented in the framework of a multiple size group (MUSIG) model. Population balance equations are passive transport equations for the number density of the bubbles of each size. The right hand side of the population balance equations includes source and sink terms that determine the birth and disappearance rates due to bubble breakup into smaller bubbles and the coalescence of two smaller bubbles to produce a specific size. In this study different breakup and coalescence models are reviewed and summarized. We introduced some modifications on the breakup model by Luo and Svendsen [37] and the coalescence model by Prince and Blanch [46]. The modified model developed in this appendix has been applied for Wemco $0.8m^3$ and Wemco $300m^3$ flotation machines and the model and results have been transferred to FLSmidth Minerals Inc. Salt Lake City, Utah, USA.

B.2 Theory: Population Balance and Multiple Group Size Models

In flotation machines, a range of bubble sizes exists in any region of the machine, and the distribution over that range varies in space and time. In theory, we may assume the existence of a continuous bubble size distribution given by bubble volume probability density function. A feasible approach is to discretize this continuous representation of the bubbles sizes into a finite number of groups. Bubbles within each group are assumed to have the same volume. Let $n(v;x;t)$ denote the number density, where v is bubble volume, and x and t are space and time. ndv is the number of bubbles having volumes between v and $v+dv$ per unit of spatial volume. The Multiple Size Group Model (MUSIG) aims at determining an approximation to the continuous number density. The continuous bubble size distribution $n(v)$ (dependence on x and t will be suppressed) is divided into a finite number of groups (or bins) M_g. Each group is represented by one number density N_i defined by

$$N_i = \int_{v_{i-1/2}}^{v_{i+1/2}} n(v)dv \tag{B.1}$$

We note that the integral is over bubble volume distribution (not space). Now, N_i is the number of bubbles (per unit of spatial volume) in the ith group (or bin). It is assumed that the bubbles in that group are of equal volume, v_i. The objective of the MUSIG model is to determine bubble volume pdf and hence $N_i(x;t)$ (units: m^{-3}). To that end we introduce the group size fraction f_i which is the ratio of volume fraction of gas in the ith group to the total gas volume fraction of all groups. Let α_g denote the local air volume fraction, hence $\alpha_i = N_i v_i$ is the local volume fraction of the ith group of bubbles, and hence $f_i = \alpha_i/\alpha_g$, and $\sum f_i = 1$. Conservation of mass for the ith group gives the Population Balance equation

$$\frac{\partial \rho_g \alpha_g f_i}{\partial t} + \nabla \cdot (\rho_g \alpha_g f_i \vec{V_g}) = B_{bi} - D_{bi} + B_{ci} - D_{ci} \tag{B.2}$$

where B_{bi}, D_{bi} are called birth and disappearance rates due to breakup of a bubble into smaller bubbles, and B_{ci} and D_{ci} are birth and disappearance rates due to coalescence of two bubbles. In this work, we used a homogeneous model in which the convection velocity $\vec{V_g}$ is the same for all groups. Thus, in addition to the set of momentum and turbulence model equations for two-phase flow, mass conservation equations must also be solved simultaneously for each of the groups. The computation time increases dramatically as the number of groups increases.

B.3 Breakup Models

B.3.1 Luo and Svendsen Breakup Model

Luo and Svendsen [37]model accounts for bubbles breakup due to collisions of bubbles with turbulent eddies of length scales on the order of the bubble size. Turbulent transport is due to eddies of length scales larger than bubbles sizes. The breakup process depends on the kinetic energy level of the colliding eddies. This constraint implies that the kinetic energy of the eddies has to be greater than or equal to the increase in the surface energy due to binary breakup. A bubble of volume v breaks up into two bubbles of volume $v_1 = vf_{BV}$ and $v - v_1$ and $0 \leq f_{BV} \leq 1$ (binary process). Breakup probability in Luo and Svendsen [37]model is equal to the probability of the colliding eddies with bubbles of sizes in the inertial subrange and isotropic turbulence. Those eddies are having kinetic energy equal to or greater than the increase in bubbles surface energy due to breakup. Luo and Svendsen [37] breakup kernel is written,

$$g(v_i, f_{BV}v_i) = 0.923(1-\alpha_g)\left(\frac{\epsilon}{d_i^2}\right)^{1/3}\int_{\xi_{min}}^{1}\frac{(1+\xi)^2}{\xi^{\frac{11}{3}}}exp(-\frac{12c_f\sigma}{\beta\rho_w\epsilon^{2/3}d_i^{5/3}\xi^{11/3}})d\xi \tag{B.3}$$

and

$$f_{BV} = \left(\frac{d_j}{d_i}\right)^3 \tag{B.4}$$

$$c_f = f_{BV}^{2/3} + (1-f_{BV})^{2/3} \tag{B.5}$$

where index i denotes mother bubbles and index j denotes daughter ones and $11.4\eta \leq \xi_{min} \leq 31.4\eta$ and $\beta = 2.0$.

B.3.2 Martinez-Bazan Breakup Model

Another breakup model developed by Martinez-Bazan [38] based on the differences between inertial and capillary stresses of the two bubbles results from the breakup of one mother. The minimum size of breakup is limited by $D_{min} = (12\sigma/(\beta\rho D_0))^{3/2}\epsilon^{-1}$. The probability of splitting one bubble of diameter D_0 into two bubbles D_1 and its complement is weighted by the product of the two stresses differences. Martinez-Bazan [38] daughter bubble size distribution is written as,

$$P(D_i^*) = \frac{\left[D_i^{*2/3} - \Lambda^{5/3}\right]\left[(1-D_i^{*3})^{2/9} - \Lambda^{5/3}\right]}{\int_{D_{min}^*}^{D_{max}^*}\left[D_i^{*2/3} - \Lambda^{5/3}\right]\left[(1-D_i^{*3})^{2/9} - \Lambda^{5/3}\right]dD^*} \tag{B.6}$$

where D_i is the daughter bubble diameter and $D_i^* = D_i/D_0$, $D_c = (12\sigma/(\beta\rho))^{3/5}\epsilon^{-2/5}$ and $\Lambda = D_c/D_0$.

B.3.3 Lehr and Mewes Breakup Models

Lehr and Mewes [33] derived a binary breakup kernel for bubbles sizes on the order of the inertial subrange similar to Luo and Svendsen [37] breakup model. However, Lehr and Mewes [33] considered both inertial forces that result in breakup with minimum increase of the bubbles surface energy and interfacial forces that result in the minimum stable daughter bubble size. These two constraints gives large probability to very small bubbles to breakup into two equal sizes and large bubbles to breakup into one stable small bubbles and their complements. This models gives a M-shaped daughter bubble size distribution with two maximals close to the very small breakage volume ratio f_{BV} and $f_{BV} = 1$. Lehr and Mewes [33] breakup kernel Eq B.3.3 is only applied for mother bubbles larger than the maximum stable bubble volume v_{stable} and $0 \leq f_{BV} \leq 0.5$. Daughter bubbles of breakage volume ratio $0.5 < f_{BV} \leq 1.0$ have the same rate as their complements.

$$g(v_i, f_{BV}v_i) = \begin{cases} A_i v_{stable} f_{BV}^{2/3} \left((f_{BV}\widehat{v_i})^{7/6} - \frac{1}{\widehat{v_i}^{7/9}} \right) & f_{BV}v_i < v_{stable} \\ A_i v_{stable} f_{BV}^{2/3} \left(\frac{1}{(f_{BV}\widehat{v_i})^{7/9}} - \frac{1}{\widehat{v_i}^{7/9}} \right) & f_{BV}v_i > v_{stable} \end{cases}$$

where,

$$v_{stable} = \frac{\pi}{6} 2^{\frac{3}{5}} \left(\frac{\sigma}{\rho_f} \right)^{\frac{9}{5}} \epsilon^{\frac{-6}{5}} \tag{B.7}$$

$$A_i = 1.5(1 - \alpha_g) v_i \left(\frac{\rho_f}{\sigma} \right)^{\frac{11}{5}} \epsilon^{\frac{9}{5}} \tag{B.8}$$

and

$$\widehat{v_i} = \frac{v_i}{v_{stable}} \tag{B.9}$$

Lehr et al. [34] developed another breakup kernel model based on capillary pressure constraint and interfacial forces balance inertial forces of the eddies. Their model has a M-shaped daughter bubbles size distribution and written as follows

$$g(v_i, f_{BV}v_i) = 1.189 \frac{v_i \sigma}{\rho_w d_i^{16/3} \epsilon^{1/3} f_{BV}^{1/3}} \int_{\xi_{min}}^{1} \frac{(1+\xi)^2}{\xi^{\frac{13}{3}}} exp(-\frac{2\sigma}{\rho_w \epsilon^{2/3} d^{5/3} \xi^{2/3} f_{BV}^{1/3}}) d\xi \tag{B.10}$$

where $\xi_{min} = f_{BV}^{1/3}$ and $0 \leq f_{BV} \leq 0.5$. Podila et al. [44] conducted CFD simulation of bubble size distribution in a bubble column using breakup kernel by Luo and Svendsen [37] and Lehr et al. [34] and obtained qualitative agreement between CFD simulations and experiments. However more extensive experimental work is needed to validate theoretical breakup kernels.

B.3.4 Wang Breakup Model

Wang et al. [71] have derived a breakup model along the same line as Luo and Svendsen [37] breakup model. However, Wang et al. [71] considered both minimum surface energy constraint and maximum capillary pressure constraint of the daughter bubbles. Wang et al. [71] assumed that the breakup probability of a bubble of size v_i to $f_{BV}v_i$ and its complementary volume to be the same when hit by an eddy of size λ having an energy $e(\lambda)$. The pdf of breakup is equal to product of energy distribution of the eddies and the breakup probability.

$$f_{BVmin} = \left(\frac{\pi\lambda^3\sigma}{6e(\lambda)d_i}\right)^3 \tag{B.11}$$

$$\left(f_{BVmax}^{2/3} + (1 - f_{BVmax})^{2/3}\right)\pi d^2\sigma = c_{fmax} \tag{B.12}$$

$$c_{fmax} = min\left((2^{1/3} - 1), \frac{e(\lambda)}{\pi d^2\sigma}\right) \tag{B.13}$$

$$P(f_{BV}|d_i, e(\lambda), \lambda) = \begin{cases} \frac{1}{f_{BVmax} - f_{BVmin}} & f_{BVmax} - f_{BVmin} \geq \delta \; and \; f_{BVmin} \leq f_{BV} \leq f_{BVmax} \\ 0 & elsewhere \end{cases}$$

$$P_e(e(\lambda)) = \frac{1}{\overline{e}(\lambda)} exp\left(-e(\lambda)/\overline{e}(\lambda)\right) \tag{B.14}$$

$$\overline{e}(\lambda) = \frac{\pi}{6}\lambda^3\rho_f\frac{\overline{u}_\lambda^2}{2} \tag{B.15}$$

$$P(f_{BV}|d_i, \lambda) = \int_0^\infty P(f_{BV}|d, e(\lambda), \lambda)P_e(e(\lambda))de(\lambda) \tag{B.16}$$

$$g(v_i, f_{BV}v_i) = 0.923(1 - \alpha_g)\epsilon^{1/3}\int_{\xi_{min}}^1 P(f_{BV}|d_i, \lambda)\frac{(d_i + \lambda)^2}{\lambda^{\frac{11}{3}}}d\lambda \tag{B.17}$$

B.3.5 Modified Luo and Svendsen Breakup Model

Luo and Svendsen [37] model has a U-shaped daughter bubble size distribution that gives a minimum probability for a bubble to break into two equal sizes and gives larger probabilities to the bubble to break into a very large daughter bubble and its complement one. As discussed by Lehr and Mewes [33] and Wang et al. [71], this may not be physical because capillary pressure is another constraint on the minimum daughter bubble size. To avoid the formation of very large bubbles and very small bubbles, daughter bubble size has been multiplied by an *ad hoc* quadratic function that changes the daughter bubble size as shown in Figures B.1a- B.1b and $\xi_{min} = 31.4\eta$. This gives very small chance for the mother bubble to break into very small daughter bubble and its complement. In this model eddies of size λ are assumed to have spherical shapes and based on that assumption the shape factor is $C_b = 1$. In real turbulence eddies are not spherical, and more plausible size distributions were found by using a shape factor $C_b = 1/12$.

The modified Luo and Svendsen is written as follows

$$g(v_i, f_{BV} v_i) = 3.692 f_{BV}(1 - f_{BV})(1 - \alpha_g)\left(\frac{\epsilon}{d_i^2}\right)^{1/3} \int_{\xi_{min}}^{1} \frac{(1+\xi)^2}{\xi^{\frac{11}{3}}} exp(-\frac{12 C_b c_f \sigma}{\beta \rho_c \epsilon_c^{2/3} d_i^{5/3} \xi^{11/3}}) d\xi \tag{B.18}$$

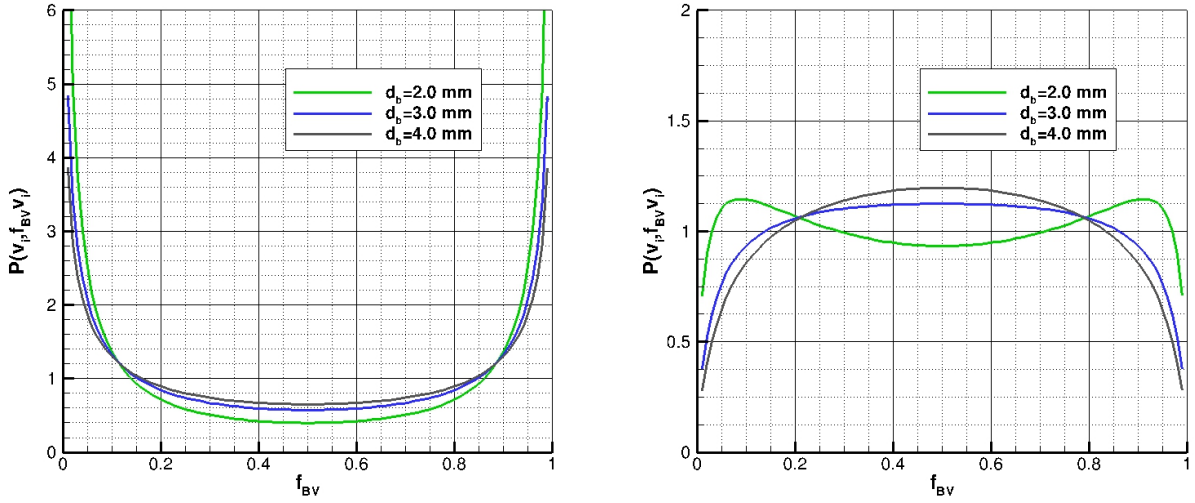

(a) Luo and Svendsen

(b) Modified Luo and Svendsen

Figure B.1: Daughter bubble size distribution, $\epsilon = 3.5 m^2/s^3$

B.4 Coalescence Model

Prince and Blanch [46] developed a phenomenological coalescence model that depends on the collisions rate of the bubbles. As shown in Fig B.2 coalescence of two bubbles in turbulent flows takes place in three stages. The two bubbles colloid first and some deformation occur due the trapped liquid between the two bubbles. In the second stage the liquid film is squeezed out and leading to film thinning between the two bubbles. The third stage is the rupture of the interface between the two bubbles when the liquid film reaches critical thickness.

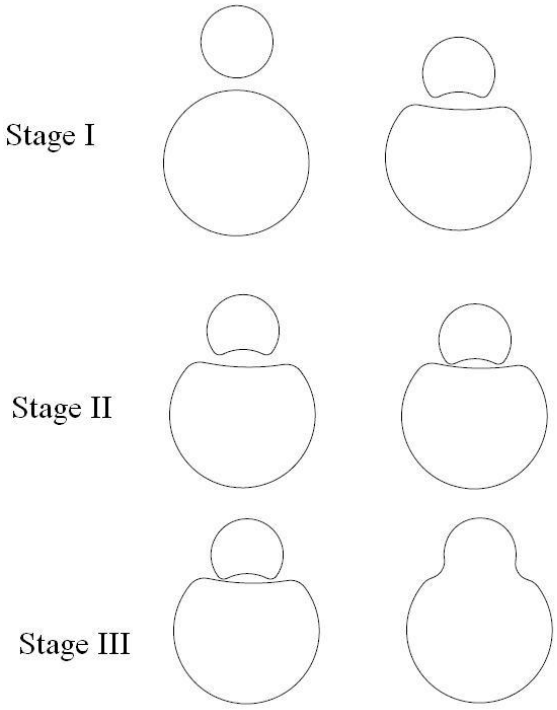

Figure B.2: Schematic diagram of coalescence stages

Bubbles collisions could happen due to turbulent motion, buoyancy effects where bubbles with different sizes will have different rise velocity leading to some collisions and collisions due to mean vorticity in the mean shear layers.

In turbulent flows collisions kernel is written as follows,

$$\beta_{ij} = \frac{\pi}{4} d_{ij}^2 \sqrt{u_i^2 + u_j^2} \tag{B.19}$$

where $d_{ij} = d_i^2 + d_j^2$ and u_i is the bubble turbulent $r.m.s$ fluctuations. Isotropic turbulence and bubbles sizes lie in the inertial subrange of turbulence are the main assumptions to estimate u_i as follows,

$$u_i = \sqrt{2}\,(\epsilon d_i)^{1/3} \tag{B.20}$$

The second stage is the liquid film drainage between the two colliding bubble. The contact time τ_{ij} between the colliding pairs of bubbles has to be on the order of the time required for liquid film to drain out (coalescence time) t_{ij}. The coalescence time t_{ij} used by Prince and Blanch [46] is expressed as

$$t_{ij} = \left[\frac{\rho_f r_{ij}^3}{16\sigma}\right]^{1/2} \ln\frac{h_o}{h_f} \tag{B.21}$$

where $h_o = 10^{-4}$m and $h_o = 10^{-8}$m and

$$r_{ij} = \frac{1}{2}\left(\frac{1}{r_i} + \frac{1}{r_j}\right)^{-1} \tag{B.22}$$

The contact time τ_{ij} depends on the turbulence dissipation rate and bubble size. An estimate for contact time τ_{ij} based on dimensional analysis [46] is expressed as follows

$$\tau_{ij} = \frac{r_{ij}^{2/3}}{\epsilon^{1/3}} \tag{B.23}$$

and coalescence efficiency [46] is written as

$$\eta_{ij} = exp\left(-\frac{t_{ij}}{\tau_{ij}}\right) \tag{B.24}$$

In our work, another *ad hoc* efficiency F_{CT} is used and multiplied by the coalescence efficiency η_{ij}.

$$F_{CT} = exp\left(-\frac{\epsilon_o}{\epsilon} - \left(\frac{r_{ij}}{c_n\eta}\right)^2\right) \tag{B.25}$$

where ϵ_o is a reference dissipation, η is Kolmogorov's length scale and c_n is a constant. ϵ_o and c_n are machine dependent constants. The modifications we have proposed in Luo and Svendsen [37] breakup model are studied in a $2D$ bubbly tank as presented in the next section.

B.5 Results

A simple $2D$ tank is used to study different breakup models as shown in Figure B.3. A block structured grid of 4800 quadratic elements has been generated in this domain. Red line represent a velocity inlet and blue lines represent pressure outlet boundary conditions. Two-phase flow of water and air has been simulated using Eulerian-Eulerian model. Drag and buoyancy are the only interfacial forces that couple the motion of the two phases. Schiller-Naumann drag model [10] is used to predict the bubble drag coefficient. The model neglects the effects of bubble deformation on drag coefficient. Unsteady RANS simulations are conducted. Turbulence transport is modeled by the shear stress transport (SST) turbulence model to close the momentum equations.

Bubbles size distribution depend on the breakup and coalescence rates as given by Eq B.2, in which RHS depend only on breakup and coalescence models. The main idea here is to neglect effects of the convective term in Eq B.2 to study the performance of the MUSIG model under equilibrium. In this case Eq B.2 can be written as

$$\frac{\partial \rho_g \alpha_g f_i}{\partial t} = B_{bi} - D_{bi} + B_{ci} - D_{ci} \tag{B.26}$$

To make the effects of convective term negligible, velocity at the inlet boundary conditions have been chosen to equal a very small value $V_{inlet} = 1.0mm/s$. The breakup and coalescence rates models are written as a User Defined Function within ANSYS CFX so that we can control all input parameters such as turbulent dissipation rate, air volume fraction and integrals lower limit ξ_{min}. Local turbulent dissipation rate and air volume fraction are the only input parameters to breakup rate models. Air volume fraction is forced to be constant at $\alpha = 0.2$ by fixing minimum air volume fraction in the domain and setting the same value at the inlet boundary conditions. Air volume fraction, the same at the inlet BC, and turbulent dissipation rate are a user input parameters for the breakup and coalescence models in this work. This allow us to study the breakup and coalescence models at equilibrium for a specified values of air volume fraction and turbulent dissipation rate. The shown distribution in Figure B.4b is an assumed initial bubble size distribution at the inlet boundary and in the flow domain. Same initial distribution of bubbles size has been applied at the inlet boundary condition.

Number of bubbles groups and bubbles diameters d_b range are an important factors that affect the bubbles size distribution. Large number of bubbles size distribution account for a wide range of bubbles diameters for a given system. However, in large domains and stirred mixing tanks this may not be feasible because of the increasing computational requirements. In this study we choose 30 bubbles groups that covers a range of bubbles diameters $0.112mm \leq d_b \leq 32.8mm$ as given in Table(B.1)

Daughter bubbles size distribution of Luo and Svendsen [37] model has been modified as given by Eq B.18. Effect of daughter bubble size distribution on the bubbles size distribution is

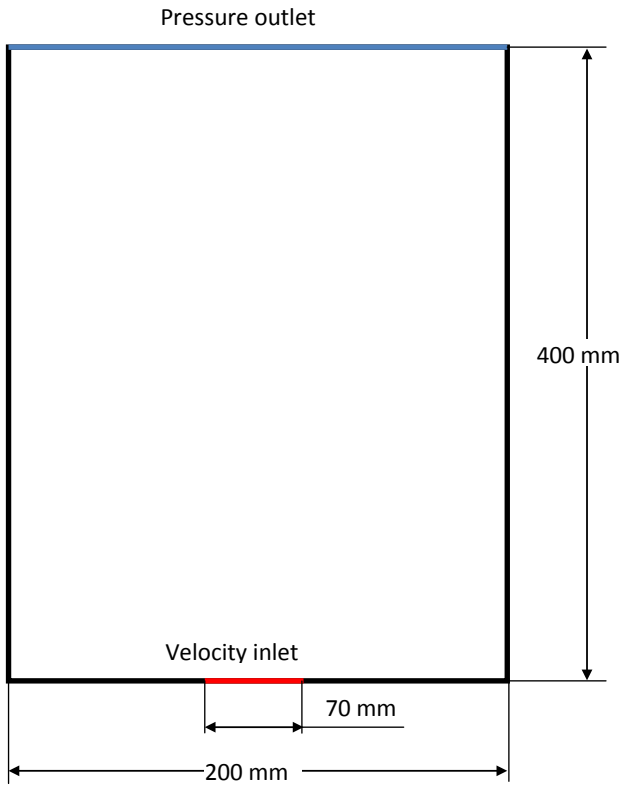

Figure B.3: Schematic diagram of the 2D bubbly tank and boundary conditions

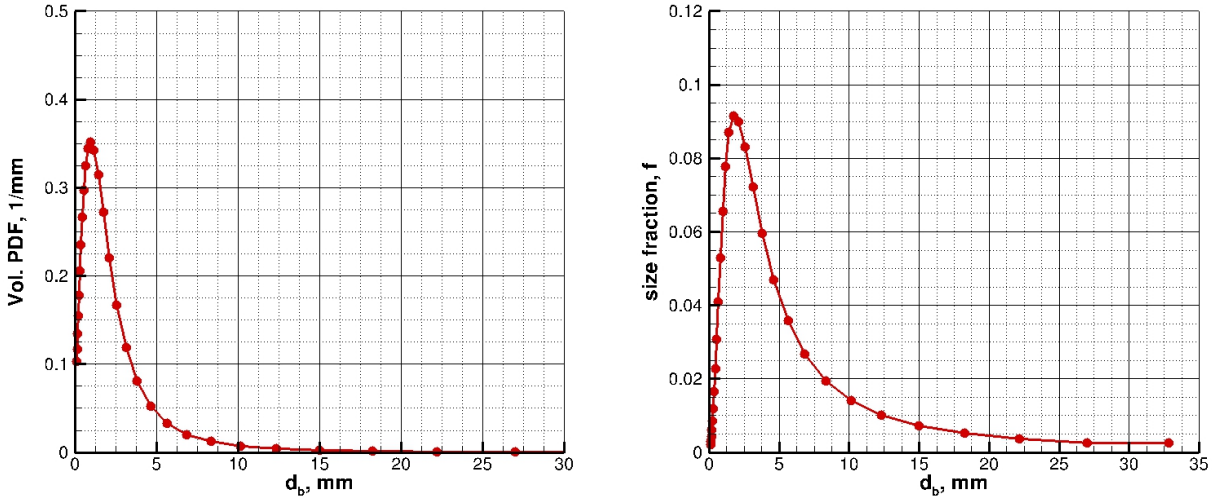

(a) Initial bubble volume PDF

(b) Initial bubbles size distribution f_i

Figure B.4: Initial bubbles size distribution f_i and bubble volume PDF

Table B.1: group Bubble diameter

group number	diameter, mm	group number	diameter, mm
1	1.12E-01	16	2.11E+00
2	1.36E-01	17	2.57E+00
3	1.66E-01	18	3.13E+00
4	2.01E-01	19	3.80E+00
5	2.45E-01	20	4.63E+00
6	2.98E-01	21	5.63E+00
7	3.62E-01	22	6.85E+00
8	4.41E-01	23	8.33E+00
9	5.36E-01	24	1.01E+01
10	6.52E-01	25	1.23E+01
11	7.94E-01	26	1.50E+01
12	9.65E-01	27	1.82E+01
13	1.17E+00	28	2.22E+01
14	1.43E+00	29	2.70E+01
15	1.74E+00	30	3.28E+01

depicted in Figures B.5a and B.5b. The original model has a small peak at the very small bubble diameter and another main peak at $d_b = 0.536mm$. This behavior is attributed to the U-shaped daughter bubbles size distribution which gives higher breakup rates to the very small bubbles and their complements. The modified daughter bubbles size distribution, M or $\bigcap$-shaped, shows a more plausible bubble size distribution as shown in Figure B.5b. Bubbles volume PDF for the modification $mod1$ which has $C_b = 1$ has a maximum value around bubble diameter $d_b = 0.536mm$ and no bi-modal distribution is observed. Modifications $mod2$ which has $C_b = 1/6$ and $mod3$ which has $C_b = 1/12$. As shown in Figure B.5b, the maximum value of bubbles volume PDF for $mod2$ is around bubble diameter $d_b = 0.245mm$ and for $mod3$ is around bubble diameter $d_b = 0.166mm$. There is no available experimental results that can be used to validate these models. However, we present a method that can be used to show the sensitivity of model prediction to various parameters in the model.

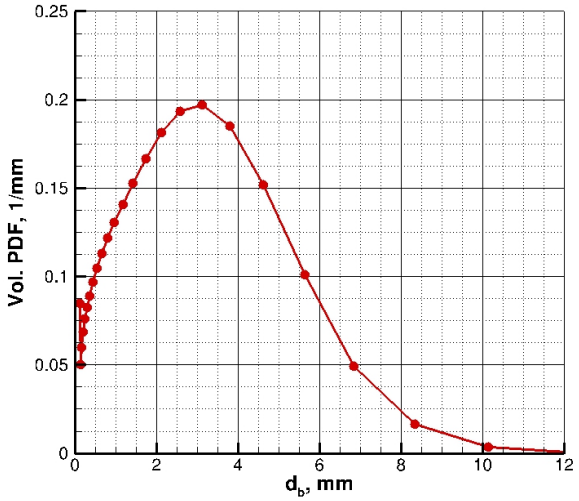

(a) Original model by Luo and Svendsen [37]

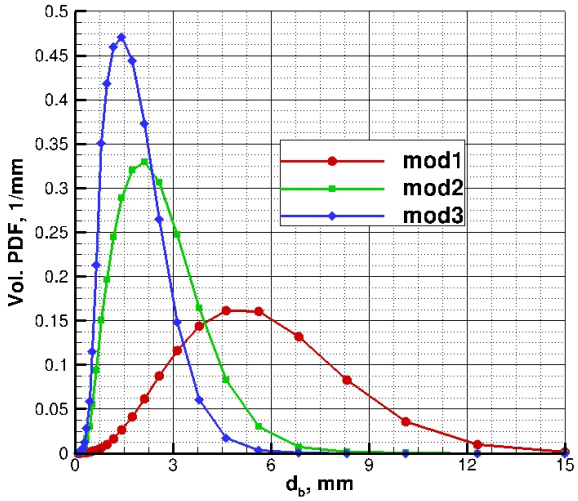

(b) Luo and Svendsen [37] modified model mod1→ Eq B.18 and $C_b = 1$, mod2→ Eq B.18 and $C_b = 1/6$, mod3→ Eq B.18 and $C_b = 1/12$

Figure B.5: Bubbles volume PDF at $\epsilon = 2.0m^2/s$

Appendix C

CFD-Based Flotation Model for Bubbles and Particles Size Distributions

Attachment rate constant k_1 in Eq 5.9 and detachment rate constant k_2 in Eq 5.17 depend on the bubbles size as well as particles size. In Chapters 5 and 6 a uniform bubble size is specified, we conducted a parametric two-phase flow simulations in Wemco and Dorr-Oliver flotation machines. This assumption is useful to study the effect of bubble size on the hydrodynamics and the recovery rate in flotation machines. However, this assumption is not realistic. Slurry feed to the flotation machines, which may have particles loading of 10%-30% by weight, has a particle size distribution around some Sauter mean diameter. Both forced air and self-aerated flotation machines produce a range of bubbles diameters with a certain distribution that vary in space and time. The analysis that have been presented in Chapter 5 reveals the importance of modeling flotation kinetics based on first principles for a particle size distribution and bubble size distribution.

C.1 Rate Constant for Bubble Size Distribution

Flotation is modeled as a first-order rate process for a bubble size distribution and uniform particles size as given by the fundamental equation

$$\frac{dn_{p1}}{dt} = -n_{p1} \sum_{j=1}^{M_g} k_{1j} n_{bj} + \sum_{j=1}^{M_g} k_{2j} n_a \tag{C.1}$$

where n_{p1} is the particles number density (number of particles per unit volume) of free parti-

cles (not attached to bubbles), n_{bj} is the number density of bubbles available for attachment of each bubbles group. Each group contains a number of bubbles having the same diameter d_{bj} The number density of each bubbles group $n_{bj} = \alpha_j / v_{bj}$ where α_j is the air volume fraction of the jth group and v_{bj} is the volume of one bubble of that group and $1 \leq j \leq M_g$. M_g is the number of bubbles group specified a priori in the CFD two-phase Population Balance Model (PBM) simulation.

The attachment rate constant of each bubbles group is written as

$$k_{1j} = \beta_j P_{cj} P_{aj} P_{sj} \tag{C.2}$$

where P_{cj}, P_{aj}, and P_{sj} are probabilities of particle-bubble collision, adhesion, and stabilization of each group. The expressions for the probabilities and collisions kernel for bubbles of size d_{bj} are obtained from the corresponding expressions in Chapters 2 and 5 by replacing d_b by d_{bj}. All expressions have to be executed for each group size ($j = 1, ..., M_g$).

C.2 Particle Size Distribution

Particles in the feed slurry to a flotation machine have a particle size distribution. The attachment rate constant $k_1^*(d_p)$ for a particle of diameter d_p and bubble size distribution is computed as given in Section C.1 for a range of particles diameters.

$$k_1^*(d_p) = \sum_{j=1}^{M_g} k_{1j} \alpha_j (1 - \alpha_g) / v_j \tag{C.3}$$

where α_j is the air volume fraction of bubbles of volume v_j and α_g is the local air volume fraction.

Let $P(d_p)$ denote the pdf of particle size distribution. The pseudo rate constant for particle size distribution is computed

$$\tilde{k}_1^* = \int_{d_{p,min}}^{d_{p,max}} P(\lambda) k_1^*(\lambda) d\lambda \tag{C.4}$$

The machine average rate constant is obtained by integration over the machine volume,

$$R = \frac{R_f}{V} \int_V \tilde{k}_1^* (1 - b) dV \tag{C.5}$$

where R_f is a froth recovery factor.

Appendix D

Matlab Code for Zaichik at al. [78] model

Three nonlinear coupled ODEs for Zaichik-2006 model presented in Physics of Fluids paper [78] or in Zaichik et al. book 'Particles in Turbulent flows' [77] are solved using the Matlab code presented in this appendix.

```
function main
%%
clc
close all
clear all
dxo=0.001;
dx=0.001;
rr=1.0135;
xx(1)=dxo;
NN=600;
%   dd is the collision radius normalized by eta
db=2.48808; dp=0.82938;
dd=(db+dp)/2;
Ca=0.5;
ns=700;
for i=2:NN
    xx(i)=xx(i-1)+dx;
    dx=dx*rr;
end
for i=1:NN
    if xx(i) < dd
        I1=i;
    end
end
I1
xx(I1)
```

```
xx(NN)
%vvvv=bbbb
global Re Stp Stb St TL tauT A1 A2;
  % Input parameters
 % bubble Stokes number based on the added mass
JJ=0;
 if JJ==1

  Stb=Ca*db^2/18;
  Stp=0.1;  Re=96.3249;
  % Constants of the model
    a0inf=7; a01=11;a02=205; C0inf=7; C1=32;
    A1=sqrt(5); A2=0.3;
    a0=(a01+a0inf*Re)/(a02+Re);
    tauT=sqrt(2*Re/a0/sqrt(15));
    TL=2*(Re+C1)/(sqrt(15)*C0inf);
    St=2*Stp*Stb/(Stp+Stb);
    fact1=2*sqrt(15)/(pi*Re);

%vvv=uuu
%xx=linspace(0.01,200,2000);

sol = bvpinit(xx,@initial);


for kk=1:ns
    kk
    Stp=0.0975+0.025*kk;
    St=2*Stp*Stb/(Stp+Stb);

    %solinit = bvpinit(xx,@initial);
sol = bvp4c(@VK,@BC,sol);
YINT=deval(sol,xx);
     g12(kk)=exp(YINT(5,I1));
     St2(kk)=Stp;
     wr12(kk)=sqrt(YINT(1,I1)*fact1);
end
g12
St2_t(:,1)=St2';
St2_t(:,2)=g12';
St2_t(:,3)=wr12';

save('wr_g12pb_Run256.dat', 'St2_t', '-ascii')

for i=1:ns
beta_Z06(i)=2*pi*wr12(i)*g12(i);
end
St2_beta(:,1)=St2';
St2_beta(:,2)=beta_Z06';

save('beta_06_256_pb.dat', 'St2_beta', '-ascii')
```

```
 end
%plot(St2,wr12,'-d')

%hold on
ns=500;
NN=1600;
xx=zeros(1,NN);
dxo=0.001;
dx=0.001;
rr=1.005;
xx(1)=dxo;
%   dd is the collision radius normalized by eta

dd=dp;

for i=2:NN
    xx(i)=xx(i-1)+dx;
    dx=dx*rr;
end
for i=1:NN
    if xx(i) < dd
        I1=i;
    end
end
I1
xx(I1)
xx(NN)

Stp=20; Stb=20; Re=96.3249;
  % Constants of the model
    a0inf=7; a01=11;a02=205; C0inf=7; C1=32;
    A1=sqrt(5); A2=0.3;
    a0=(a01+a0inf*Re)/(a02+Re);
    tauT=sqrt(2*Re/a0/sqrt(15));
    TL=2*(Re+C1)/(sqrt(15)*C0inf);
    St=2*Stp*Stb/(Stp+Stb);
    fact1=2*sqrt(15)/(pi*Re);
St2=zeros(1,ns);
g12=zeros(1,ns);


sol = bvpinit(xx,@initial);
for kk=1:ns
    kk
    Stp=20.04-0.04*kk;
    Stb=Stp;
    St=2*Stp*Stb/(Stp+Stb);

    %solinit = bvpinit(xx,@initial);
```

```
sol = bvp4c(@VK,@BC,sol);
YINT=deval(sol,xx);
     g12(kk)=exp(YINT(5,I1));
     St2(kk)=Stp;
     wr11(kk)=sqrt(YINT(1,I1)*fact1);
end
g12
St2_t=zeros(ns,3);
St2_beta=zeros(ns,2);
St2_t(:,1)=St2';
St2_t(:,2)=g12';
St2_t(:,3)=wr11';
save('wr_g11pp_Run256.dat', 'St2_t', '-ascii')

beta_ST=sqrt(8*pi/sqrt(15))*dd/sqrt(Re);
for i=1:ns
beta_Z06(i)=2*pi*wr11(i)*g12(i)/beta_ST;

St2_beta(i,1)=St2(i);
St2_beta(i,2)=beta_Z06(i);
end
save('beta_06_256_pp.dat', 'St2_beta', '-ascii')


plot(St2,wr11,'-r')

%fprintf('For Von karman rotating fluid problem %4.2f.\n',sol.parameters);
  figure;
  plot(sol.x,sol.y(1,:),'-r','lineWidth' ,2)
  hold on
  plot(sol.x,sol.y(3,:),'-b','lineWidth' ,2)
  %axis([0 15 0 150])
  title('red-Spll,blue-dSpll/dr ');
  xlabel('radius')
  ylabel('Spll,dSpll/dr');
  %legend('radial comp.','tangential comp.' )
  grid
  % sol.x'
  drawnow
  hold on
  figure;
  plot(sol.x,sol.y(2,:),'-r','lineWidth' ,2)
  hold on
  plot(sol.x,sol.y(4,:),'-b','lineWidth' ,2)
  title('red-Spnn,blue-dSpnn/dr ');
   xlabel('radius')
   ylabel('Spnn,dSpnn/dr');
%   legend('vertical comp.' )
  grid
  drawnow
  figure;
```

```
  plot(sol.x,sol.y(5,:),'-b' ,'lineWidth'  ,2)
   title('gama12 ');
   xlabel('radius')
   ylabel('gama12');
%   legend('p(zi)' )
  grid

 function G = VK(x,F)
  %%
global Re Stp Stb St TL tauT A1 A2;
    %%%%%%%%%%%%%%%%%%%%%%%%%%%%%%%%%%%%%%%%%%%%%%%%%%%%%%%%%%%%
    term1=(1-exp(-x*(A2/A1)^(3/2)))^(-2/3);
    term2=(x^4/(x^4+(TL/A2)^6))^(1/6);
    TLr=TL*term1*term2;
    dTLr=(TL*((4*x^3)/(TL^6/A2^6 + x^4) - (4*x^7)/(TL^6/A2^6 + x^4)^2))/(6* ...
    (1 - 1/exp(x*(A2/A1)^(3/2)))^(2/3)*(x^4/(TL^6/A2^6 + x^4))^(5/6)) - (2* ...
    TL*(A2/A1)^(3/2)*(x^4/(TL^6/A2^6 + x^4))^(1/6))/(3*exp(x*(A2/A1)^(3/2))*(1
...
     - 1/exp(x*(A2/A1)^(3/2)))^(5/3));
     %-%%%%%%%%%%%%%%%%%%%%%%%%%%%%%%%%%%%%%%%%%%%%%%%%%%%%%%%%%%%%
      C=2;
      A=2*Re;
     %-%%%%%%%%%%%%%%%%%%%%%%%%%%%%%%%%%%%%%%%%%%%%%%%%%%%%%%%%%%%%
    fact1=exp(-x/(15*C)^(3/4));
    fact2=(15^3*x^4/(15^3*x^4+(2*Re/C)^6))^(1/6);
    Sll=(2*Re/sqrt(15))*(1-fact1)^(4/3)*fact2;
    Sll_dev=(15^(1/2)*A*(1 - 1/exp(x/(15*C)^(3/4)))^(4/3)*((13500*x^3)/(A^6 ...
    /C^6 + 3375*x^4) - (45562500*x^7)/(A^6/C^6 + 3375*x^4)^2))/(90*((3375* ...
    x^4)/(A^6/C^6 + 3375*x^4))^(5/6)) + (4*15^(1/2)*A*(1 - 1/exp(x/(15*C) ...
   ^(3/4)))^(1/3)*((3375*x^4)/(A^6/C^6 + 3375*x^4))^(1/6))/(45*exp(x/ ...
   (15*C)^(3/4))*(15*C)^(3/4));
    Snn=Sll+0.5*x*Sll_dev;
    Sll_diff2=-(168750*15^(1/2)*A*C^12*x^6*(A^12*(15*C)^(3/2) ...
        - 8*A^12*x^2 - 91125000*C^12*x^10 + 6*A^12*x^2*exp(x/(15*C)^(3/4)) ...
        + 68343750*C^12*x^10*exp(x/(15*C)^(3/4)) ...
        - 2*A^12*exp(x/(15*C)^(3/4))*(15*C)^(3/2) ...
        + A^12*exp((2*x)/(15*C)^(3/4))*(15*C)^(3/2) ...
        + 8*A^12*x*(15*C)^(3/4) - 54000*A^6*C^6*x^6 ...
        + 50625*A^6*C^6*x^4*(15*C)^(3/2) + 27000*A^6*C^6*x^5*(15*C)^(3/4) ...
        - 8*A^12*x*exp(x/(15*C)^(3/4))*(15*C)^(3/4) ...
        + 40500*A^6*C^6*x^6*exp(x/(15*C)^(3/4)) ...
        - 101250*A^6*C^6*x^4*exp(x/(15*C)^(3/4))*(15*C)^(3/2) ...
        + 50625*A^6*C^6*x^4*exp((2*x)/(15*C)^(3/4))*(15*C)^(3/2) ...
        - 27000*A^6*C^6*x^5*exp(x/(15*C)^(3/4))*(15*C)^(3/4)))/ ...
        (exp((2*x)/(15*C)^(3/4))*(1 - 1/exp(x/(15*C)^(3/4)))^(2/3)*(15*C)^(3/2) ...
        *(A^6 + ...
        3375*C^6*x^4)^4*((3375*x^4)/(A^6/C^6 + 3375*x^4))^(11/6));
    Snn_dev=1.5*Sll_dev+0.5*x*Sll_diff2;
   %-%%%%%%%%%%%%%%%%%%%%%%%%%%%%%%%%%%%%%%%%%%%%%%%%%%%%%%%%%%%%
    z=tauT/TL;
    omega_p=Stp/TL; omega_b=Stb/TL;
```

```
fup=(2*omega_p+z^2)/(2*omega_p+2*omega_p^2+z^2);
fub=(2*omega_b+z^2)/(2*omega_b+2*omega_b^2+z^2);
%-------------------------------------------------------------------
zr=z;
omega_rp=Stp/TLr; omega_rb=Stb/TLr;
frp=(2*omega_rp+zr^2)/(2*omega_rp+2*omega_rp^2+zr^2);
frb=(2*omega_rb+zr^2)/(2*omega_rb+2*omega_rb^2+zr^2);
%-------------------------------------------------------------------
gup=TL/Stp-fup;
gub=TL/Stb-fub;
grp=TLr/Stp-frp;
grb=TLr/Stb-frb;
%-------------------------------------------------------------------
domega_p=-dTLr*Stp/(TLr)^2; domega_b=-dTLr*Stb/(TLr)^2;
dtauTr=tauT*dTLr/TL;
dzr=0;
dz2r=0;
dfrp=((2*omega_rp+2*omega_rp^2+zr^2)*(2+dz2r)-(2*omega_rp+zr^2) ...
       *(2+4*omega_rp+dz2r))/(2*omega_rp+2*omega_rp^2+zr^2)^2;
dfrb=((2*omega_rb+2*omega_rb^2+zr^2)*(2+dz2r)-(2*omega_rb+zr^2) ...
       *(2+4*omega_rb+dz2r))/(2*omega_rb+2*omega_rb^2+zr^2)^2;
   dfrp=dfrp*domega_p;
   dfrb=dfrb*domega_b;
dgrp=dTLr/Stp-dfrp; dgrb=dTLr/Stb-dfrb;
%-------------------------------------------------------------------
aA=2*(Stp*gup-Stb*gub)*(Stb-Stp)*Re/(sqrt(15)*(Stp+Stb));
Br=(Stp^2*grp+Stb^2*grb)/(Stp+Stb);
dH1=(Stp^2*dgrp+Stb^2*dgrb)*Sll/(Stp+Stb)+Br*Sll_dev;
dH2=(Stp^2*dgrp+Stb^2*dgrb)*Snn/(Stp+Stb)+Br*Snn_dev;
Dpll=St*F(1)+aA+Br*Sll;
Dpnn=St*F(3)+aA+Br*Snn;
Cc=(Stb-Stp)*(fup-fub)*Re/(sqrt(15)*(Stp+Stb));
Ar=(Stp*frp+Stb*frb)/(Stp+Stb);
Cll=Cc+Ar*Sll-F(1);
Cnn=Cc+Ar*Snn-F(3);
dDpll=St*F(2)+dH1;
dDpnn=St*F(4)+dH2;
%-------------------------------------------------------------------
GG=-(2*(F(1)-F(3))/x+F(2))*(St/Dpll);
G(1,1)=F(2);
T2    =(4/(3*x))*(Dpll*F(4)+2*Dpnn*(F(1)-F(3))/x)-(2/St)*Cll;
G(2,1)=T2/(Dpll)-2*F(2)/x-GG*F(2)-(F(2)/Dpll)*dDpll;
G(3,1)=F(4);
T3    =-(6/St)*Cnn;
T4    =-F(4)*(4/x+GG+dDpll/Dpll);
T5    =3*Dpnn/x+GG*Dpnn+dDpnn;
T6    =T5*(F(1)-F(3))+Dpnn*(F(2)-F(4));
G(4,1)=T3/(Dpll)+T4-(2/(x*Dpll))*T6;
G(5,1)=GG;
%-------------------------------------------------------------------
```

```
 function res = BC(Fa,Fb)
  %%
  global Re Stp Stb TL tauT;

  %%%%%%%%%%%%%%%%%%%%%%%%%%%%%%%%%%%%%%%%%%%%%%%%%%%%%%%%%%%%
  z=tauT/TL;
  omega_p=Stp/TL; omega_b=Stb/TL;
  fup=(2*omega_p+z^2)/(2*omega_p+2*omega_p^2+z^2);
  fub=(2*omega_b+z^2)/(2*omega_b+2*omega_b^2+z^2);

  CC=(fup+fub)*Re/sqrt(15);
  res = [Fa(2)
         Fa(4)
         Fb(1)-CC
         Fb(3)-CC
         Fb(5) ];

     function Finit=initial(x)
%%
  %%
  % Input parameters
  global Re Stp Stb TL tauT;

  %%%%%%%%%%%%%%%%%%%%%%%%%%%%%%%%%%%%%%%%%%%%%%%%%%%%%%%%%%%%
  z=tauT/TL;
  omega_p=Stp/TL; omega_b=Stb/TL;
  fup=(2*omega_p+z^2)/(2*omega_p+2*omega_p^2+z^2);
  fub=(2*omega_b+z^2)/(2*omega_b+2*omega_b^2+z^2);

  CC=(fup+fub)*Re/sqrt(15);
         Finit=[ CC
                 0
                 CC
                 0
                 0];
```